FRM II
Forschungs-Neutronenquelle
Heinz Maier-Leibnitz

MLZ
Heinz Maier-Leibnitz Zentrum

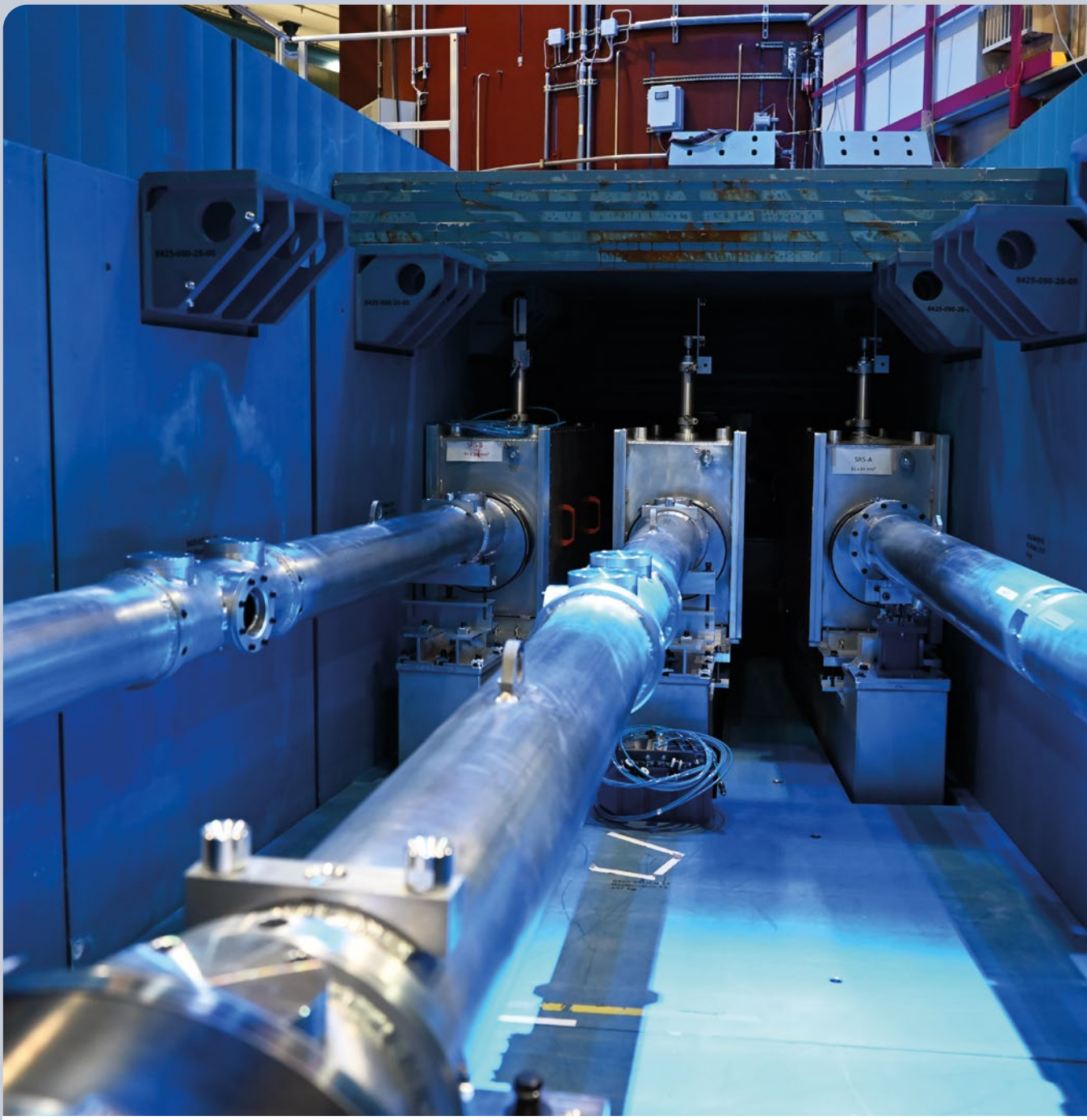

Annual Report 2025

MLZ is a cooperation between:

JÜLICH
Forschungszentrum

Helmholtz-Zentrum
hereon

Technical
University
of Munich

With funding from the:

Bavarian State Ministry of Science and the Arts

Federal Ministry of Research, Technology and Space

The Heinz Maier-Leibnitz Zentrum (MLZ):
The Heinz Maier-Leibnitz Zentrum is a leading centre for cutting-edge research with neutrons and positrons. Operating as a user facility, the MLZ offers a unique suite of high-performance neutron scattering instruments. This cooperation involves the Technical University of Munich, the Forschungszentrum Jülich GmbH and the Helmholtz-Zentrum hereon GmbH. The MLZ is funded by the German Federal Ministry of Research, Technology and Space, together with the Bavarian State Ministry of Science and the Arts and the partners of the cooperation.

The Forschungs-Neutronenquelle Heinz-Maier-Leibnitz (FRM II):
The Forschungs-Neutronenquelle Heinz-Maier-Leibnitz provides neutron beams for the scientific experiments at the MLZ. The FRM II is operated by the Technical University of Munich and is funded by the Bavarian State Ministry of Science and the Arts.

Joint Annual Report 2025

of the MLZ and FRM II

2025 IN NUMBERS

PUBLICATIONS AND COMMUNICATION

615 media articles

206 scientific journal articles

44 news articles on the web pages

3,086 followers on social media

THIRD-PARTY FUNDING

54 Third-Party Funding Projects at MLZ with a total volume of € 8.8 million

€ 4.69 million — Federal Ministry of Research, Technology and Space

€ 1.13 million — DFG

€ 1.59 million

€ 1.36 million from other institutions

SCIENTIFIC EVENTS

More than **70** participants at the "Munich Quantum Matter Days"

MUNICH QUANTUM MATTER DAYS

232 participants at the MLZ User Meeting

62 participants at the MLZ Conference "Neutrons for Fusion and Nuclear Applications"

51 participants at the MLZ-LLB-workshop 2025

EVENTS FOR THE PUBLIC

88 children and **270** adults participating in FRM II tours at the "Open Day with the Mouse"

4,313 visitors

Around **300** viewers at the "Science for Everyone" lecture (by Deutsches Museum)


JÜLICH
JÜLICH

Joining forces for a new beginning

In 2025, the Research Neutron Source Heinz Maier-Leibnitz (FRM II) and the Heinz Maier-Leibnitz Zentrum (MLZ) set the course for the restart of our user operation. All our colleagues in Garching are working with great dedication to provide the scientific and medical communities, as well as industry, with urgently needed neutrons.

The recent evaluation of the MLZ in 2024 once again demonstrated the high relevance of neutron research in Garching for Germany and the international community. The excellent rating awarded by the review panel served as the foundation for the extension of the MLZ cooperation. We are grateful for the continued support by our funding bodies at both federal and state levels. It was decided that the extension would undergo a transition period of 1.5 years, during which time the FRM II is expected to come into operation again, organisational issues will be developed further, and a continuation of the associated cooperation is anticipated.

A major milestone last year was the completion of the Neutron Guide Hall East (see photo on the left). The final installation and hot commissioning of the instruments will be possible, the first neutrons being produced after the restart. We are delighted that this will provide our users with a significantly expanded instrument suite covering a broad range of scientific fields, especially soft and hard condensed matter, geoscience and particle physics.

The conversion of the FRM II has also made great strides: two fuel plates made of a monolithic uranium-molybdenum alloy were successfully irradiated. This marks the first time a production process for new fuels using low-enriched uranium has been tested under realistic irradiation conditions. Based on these results, we submitted the official conversion application for the FRM II in 2025.

Furthermore, the Federal Office for the Safety of Nuclear Waste Management (BASE) has granted approval for the transport of spent fuel elements and for the storage of CASTOR casks at the Ahaus interim storage facility. Further steps are required before the first transports to Ahaus can take place. A definitive date has not yet been set as of December 2025. However, the transport of the spent fuel elements represents a vital facet for the long-term operation of the FRM II.

Our scientists also utilised the past year to plan the resumption of user operations. At their biennial retreat in Grainau, relevant aspects of the instruments and infrastructure were discussed in detail, and specific directives for action were stipulated.

In addition, our researchers are increasingly active in the field of fusion research. For instance, the MLZ Conference 2025 *Neutrons for Fusion and Nuclear Applications* in Fürstenried addressed the question of how neutron research can assist in the development of materials for fusion reactors. Moreover, the FRM II plays a key role in maintaining nuclear technology expertise, a goal pursued with determination by the Technical University of Munich (TUM). New ErUM-Pro projects to advance FRM II's instrumentation have been approved. Strong support was received for the MORIS upgrade programme during the scientific evaluation in 2024, even though a funding decision has not yet been made. This upgrade will ensure that, in the long run, the MLZ will be able to provide world class instrumentation.

Last but not least, we were also involved in the *International Year of Quantum Science and Technology*, as proclaimed by the United Nations (UN) for 2025. At the MLZ, 30 top-tier speakers presented the latest findings in areas such as quantum magnetism, spin liquids, and topological materials during the week-long *Munich Quantum Matter Days* at the end of October. The Jülich Centre for Neutron Science (JCNS) workshop 2025 was dedicated to *Quantum Materials: Theory and Experiments* as well. Other important events in the past year included a joint workshop with our French colleagues from the Laboratoire Léon Brillouin (LLB) and our annual User Meeting, which once again highlighted the international and national support for the future of the FRM II and the MLZ.

All of this underscores the high societal relevance of neutron research for Germany and the international community in Garching. We are now pooling all our resources to get FRM II back into operation.

Christian Pfleiderer Stephan Förster Martin Müller Axel Pichlmaier Jürgen Neuhaus

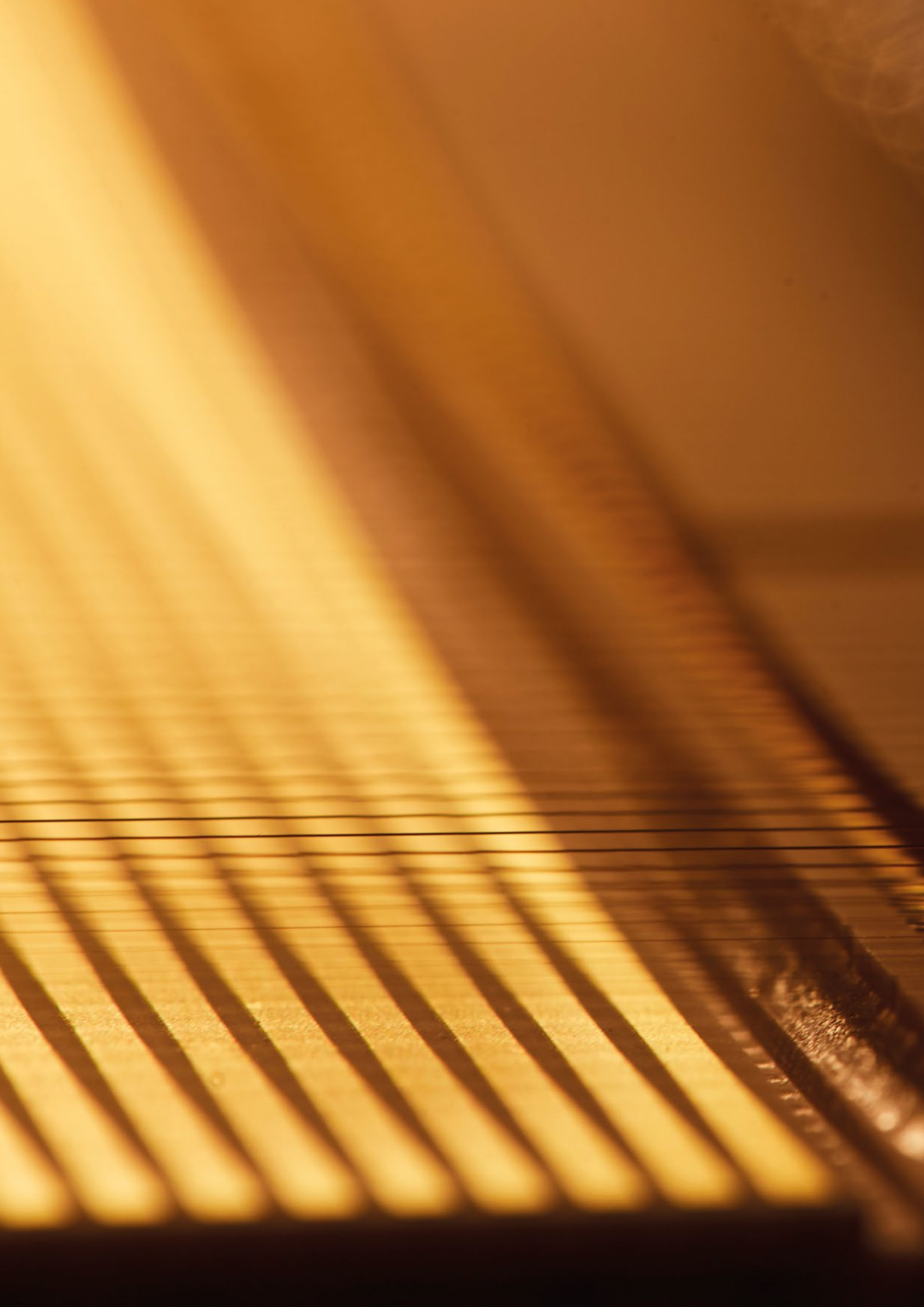

Scientific Highlights

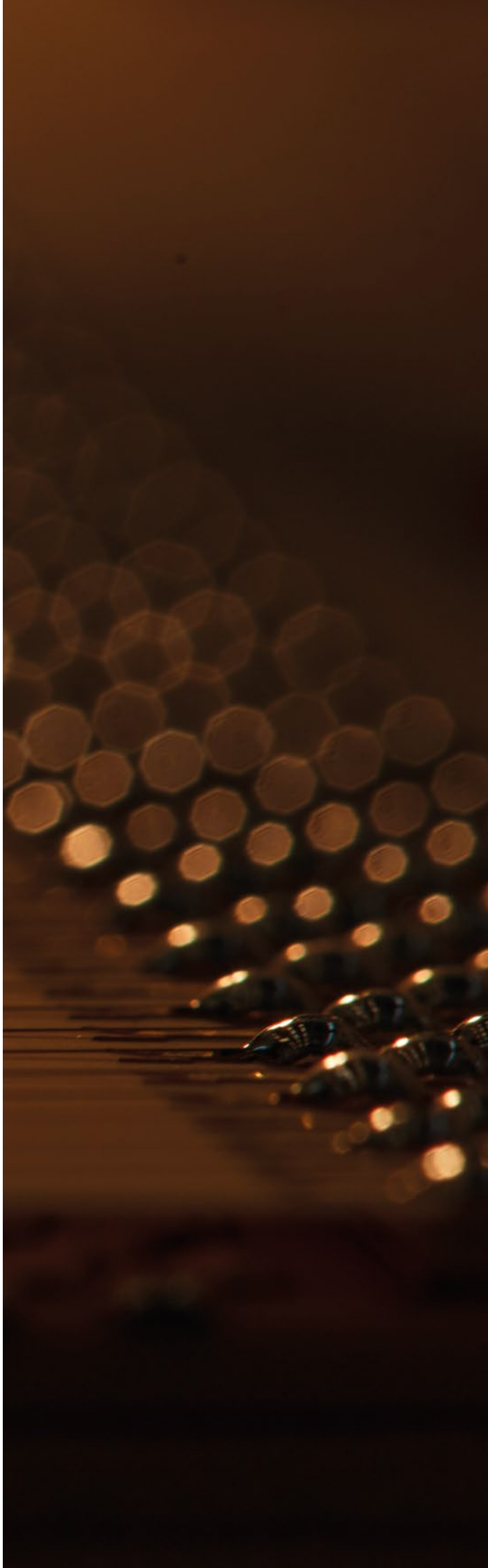

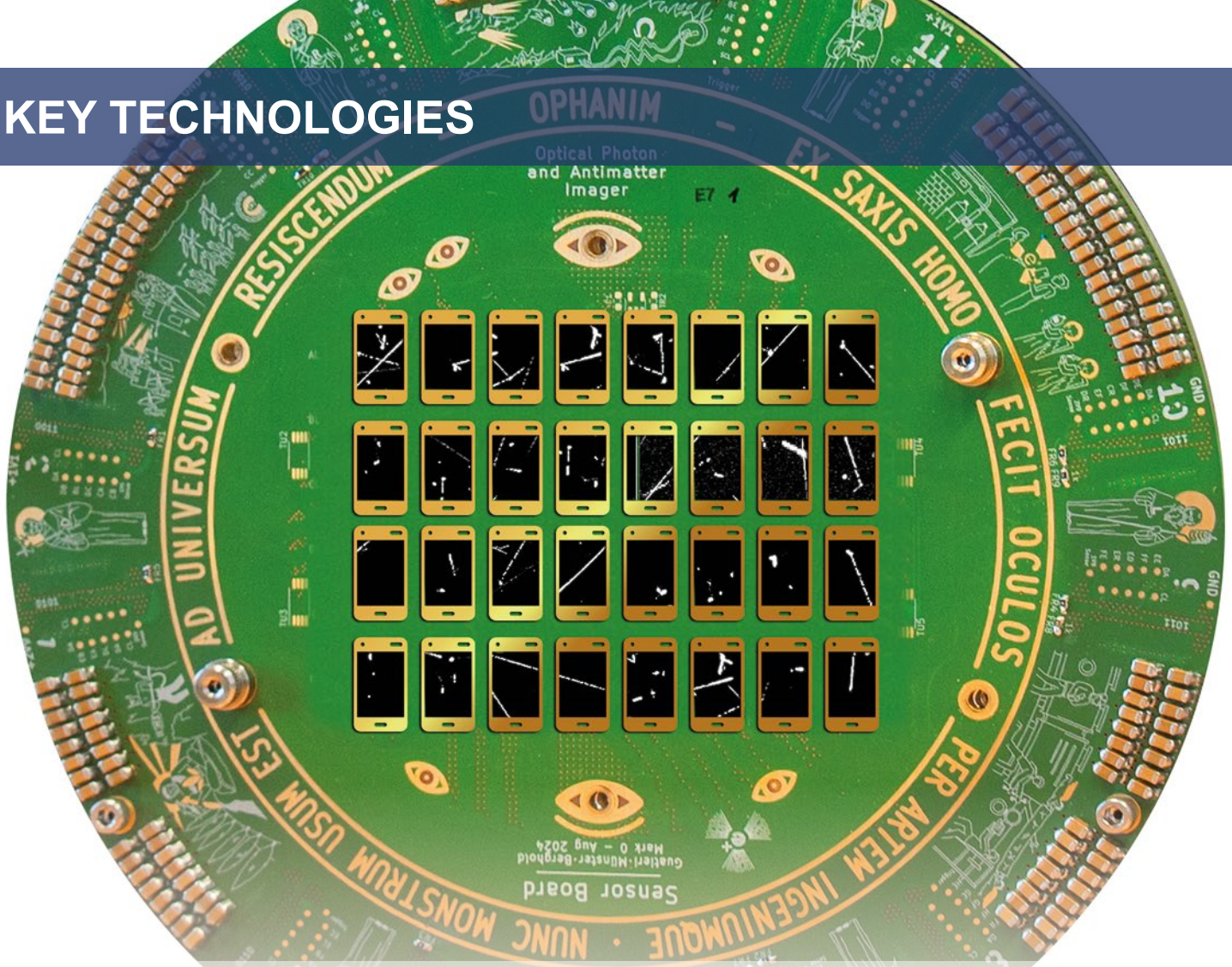

SMARTPHONES UNVEIL ANTIMATTER SECRETS

Using smartphone camera sensors, CERN researchers observed antimatter in real time with sub-micron resolution. The high-pixel detector enables precise antihydrogen and antiproton studies, revolutionising gravitational measurements and opening new opportunities in physics, medicine, and space research.

Antimatter is one of the most exotic substances we can produce. As it reacts instantly upon contact with ordinary matter, precise measurements involving antimatter have long been a technical challenge. Using smartphone sensors, CERN researchers can now make processes such as antiproton decay or the free fall of antihydrogen visible in real time. Individual annihilation fragments can be analysed in detail, providing unprecedented insights into the fundamental interactions between matter and antimatter.

World record

The Optical Photon and Antimatter Imager (OPHANIM) combines 60 modified smartphone sensors into a detector system with a resolution of 3,840 megapixels – a world record for imaging devices. The AEgIS collaboration (Antihydrogen Experiment: Gravity, Interferometry, Spectroscopy) uses this system to study how antihydrogen falls in the Earth's gravitational field. A Moiré deflectometer measures even the smallest vertical deflection. The new detector greatly increases precision while simultaneously providing insight into the interactions of low-energy antiparticles with materials.

Detectors for the future

Beyond fundamental research, the technology offers new perspectives: in medicine, for high-precision particle imaging; in industry, for analysing semiconductor microstructures; and in astronomy, for observing distant star clusters. Potential applications also include radiation monitoring, optimisation of nanofabrication, and AI-assisted materials research. Smartphone camera sensors are thus evolving into universal detectors for science and innovation.

M. Berghold et al., Real-time antiproton annihilation vertexing with submicrometer resolution, Sci. Adv. 11, eads1176 (2025)
DOI: 10.1126/sciadv.ads1176

Measurements were conducted within the AEgIS experiment at CERN using a detector developed at MLZ.

TECHNOLOGY TO PREVENT SPACE DEBRIS

Tungsten nozzles made by additive manufacturing enable high-performance arcjets that rapidly deorbit satellites, preventing space debris and supporting sustainable orbital infrastructure. Advanced imaging highlights both the potential and limits of this technology for safe, reliable spaceflight.

The rapid increase in small satellites in Earth orbit raises the risk of collisions and space debris accumulation. Thermal arcjet thrusters are being developed at the Institute of Space Systems to actively remove satellites from low Earth orbit at the end of their operational lifetime, improving spaceflight safety. These systems heat a gas by means of an electric arc and accelerate it through a nozzle to generate thrust. The nozzle geometry and material are crucial for both performance and service life.

3D-printed tungsten:
Precision meets extreme heat

Tungsten withstands extreme temperatures and erosion, making it ideal for arcjet nozzles. Additive manufacturing enables complex geometries and features that can enhance performance. However, neutron tomography shows that while performance met expectations, internal voids and deformations in the nozzle's critical throat may reduce performance over time. Precise, high-quality manufacturing is essential for reliable operation.

A look inside – Arcjets for sustainable spaceflight

Combining additive manufacturing with advanced imaging such as neutron tomography allows for detailed examination of tungsten nozzles, which conventional X-rays can hardly achieve. This reveals differences in manufacturing and early material damage, offering insights for improvement. Using robust tungsten alloys and optimised geometries, future arcjets could operate more reliably, supporting the safe deorbiting of ageing satellites.

J. Skalden, M. Ehresmann, G. Becatti, M. Schulz, A. Gustschin, J. Rebelo Kornmeier, Z. Kis, L. Szentmiklósi, G. Herdrich, Neutron imaging investigation of additively manufactured tungsten nozzles for an arcjet deorbit system, J Electr Propuls 4, 52 (2025)
DOI: 10.1007/s44205-025-00150-0

Measurements with neutrons were carried out at NORMA at BNC.

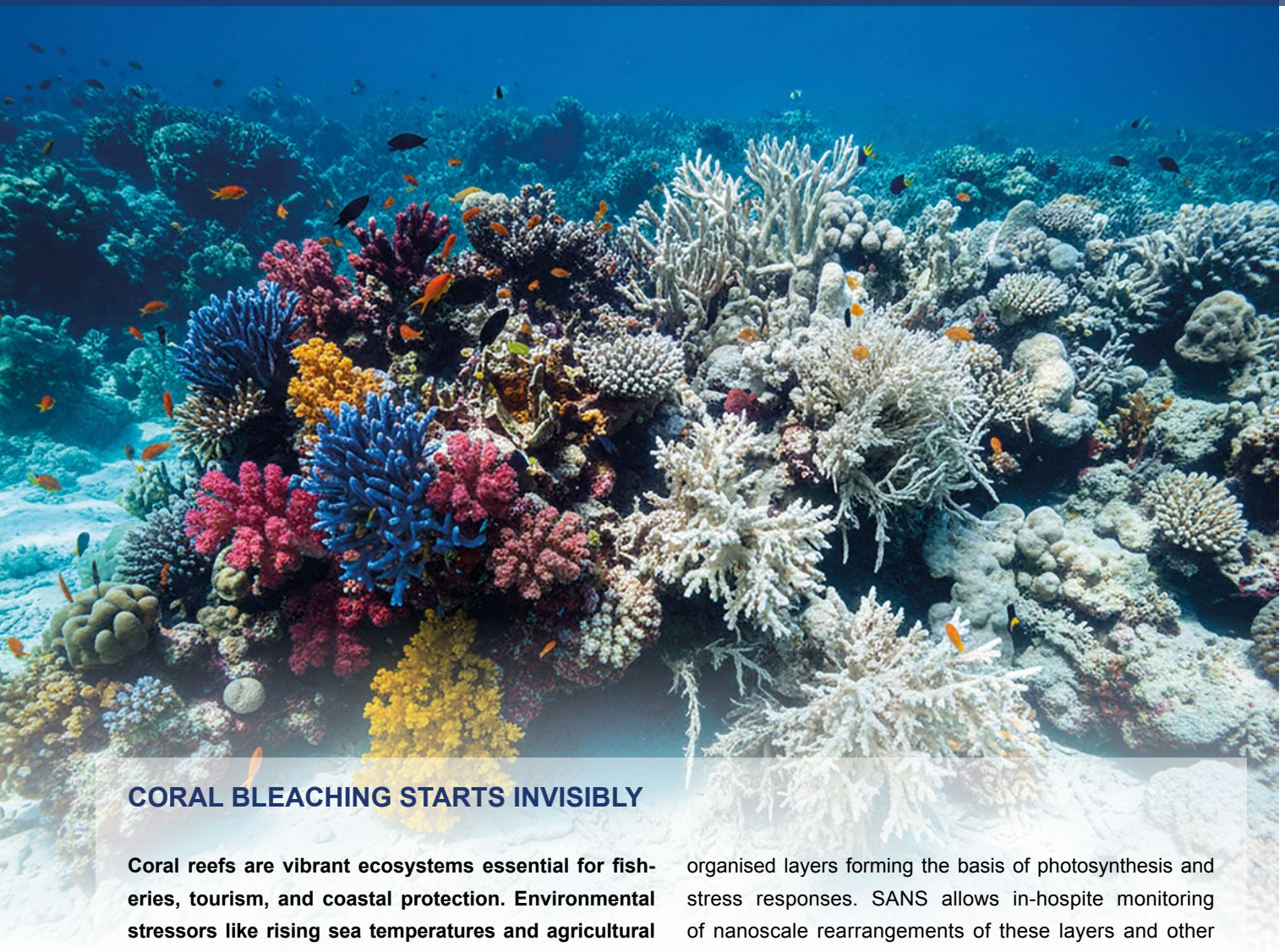

CORAL BLEACHING STARTS INVISIBLY

Coral reefs are vibrant ecosystems essential for fisheries, tourism, and coastal protection. Environmental stressors like rising sea temperatures and agricultural run-off can cause bleaching. Exploring coral-algae symbiosis offers insights into this crucial marine partnership.

Coral reefs are among the most diverse ecosystems on Earth. Nutrient-poor, their stability depends on a close symbiosis between coral polyps and single-celled algae of the genus Symbiodinium. During photosynthesis, Symbiodinium harvests sunlight to produce energy storage molecules for the host, forming a key input for the ecosystem. Environmental stress, such as elevated temperatures, can disrupt this partnership. Algae are expelled, corals bleach, and lose their foundation for survival. Bleaching often leads to the death of reef-forming corals. A central, previously hard-to-access element is the real-time response of the algae's photosynthetic membranes to high light and temperature, when expulsion is most likely.

A look inside living cells

Using Small-Angle Neutron Scattering (SANS), researchers have, for the first time, studied the membrane architecture in living algae. They analysed thylakoid membranes, organised layers forming the basis of photosynthesis and stress responses. SANS allows in-hospite monitoring of nanoscale rearrangements of these layers and other molecular constituents of the photosynthetic apparatus. Such minimal structural shifts are sensitive indicators of stress responses.

Safeguarding marine ecosystems

The findings open new possibilities for detecting early signs of coral bleaching and engineering interventions via more resilient Symbiodinium species. Understanding these microscopic processes improves prediction of stress responses in reef systems. In an era of climate change, coral reef preservation depends not just on surface conditions but on the integrity of the smallest biological structures.

R. W. Corkery, C. J. Garvey, J. E. Houston, In hospite and ex hospite architecture of photosynthetic thylakoid membranes in Symbiodinium spp. using small-angle neutron scattering, J. Appl. Cryst. 58, 1516 (2025)
DOI: 10.1107/S1600576725007332

Measurements were carried out at KWS-2 at MLZ.

KEY MECHANISMS FOR PET RECYCLING

Polyethylene terephthalate (PET) is an indispensable part of daily life: beverage bottles, food packaging, films – many products are made from this durable plastic. Its stability is technically desirable but becomes an environmental problem when bottles and packaging turn into long-lasting waste after only short-term use.

PET can be chemically broken down under strongly alkaline conditions, but these processes are energy- and resource-intensive. An alternative is enzymes – biological catalysts that can degrade PET under much milder conditions. This approach is considered promising for more sustainable recycling. However, enzymatic degradation currently slows rapidly and does not yet allow the complete breakdown of larger PET products.

Enzymes in action: Limits of PET degradation

Neutron reflectometry experiments have tracked enzymatic PET degradation directly at the nanometre scale for the first time. They reveal that water rapidly penetrates the near-surface polymer layer, allowing enzymes to access the polymer chains. The initial phase of degradation is therefore efficient. After a short time, however, the reaction slows significantly: degradation products accumulate on the surface, partially inhibit the enzymes, and gradually reduce their effectiveness. The combination of initially good accessibility and increasing product inhibition explains the observed decrease in reaction speed.

Towards bio-based recycling strategies

Understanding the microscopic mechanisms of enzymatic PET degradation makes it possible to identify weaknesses and make recycling faster and more efficient. Enzymes can be optimised, reaction conditions adjusted, and inhibitory degradation products removed. This could increase the efficiency of the process from the laboratory to industrial scale. PET waste could be recycled to a high standard, resources kept in circulation, and the demand for new plastic reduced. Bio-based recycling could thus become a central component of a resource-efficient and climate-friendly circular economy.

R. Machatschek, N.A. Tarazona, M. Balk, F. Göttsch, R. Wei, U.T. Bornscheuer, J.-F. Moulin, M. Keller, N. Schneider, P. Gutfreund, M. Müller, F.M. Toma, G. Mangiapia, Direct observation of alkaline and enzymatic poly(ethylene terephthalate) hydrolysis via neutron reflectivity: Kinetics and mechanistic insights, J. Colloid Interface Sci. 698, 138021 (2025) DOI: 10.1016/j.jcis.2025.138021

Measurements were carried out at FIGARO at ILL.

GUARDIAN OF DNA IN THE FIGHT AGAINST CANCER

The enzyme MTH1 recognises damaged DNA building blocks and chemically breaks them down – knowledge that could be crucial in the fight against cancer. X-ray and neutron crystallography help to unravel its mechanisms.

Our DNA is constantly under attack, which can lead to damage and potentially cancer. MTH1 acts as a guardian. It identifies damaged nucleotides (the building blocks of DNA) before they can be incorporated into DNA and cause mutations. Without this protection, faulty nucleotides could seriously compromise the genome. Researchers have now directly observed how the enzyme recognises these harmful molecules.

The intricate chemical dance

Using specialised X-ray and neutron techniques, researchers have found that certain parts of MTH1's active site adapt their shape and electric charge, depending on the damaged nucleotides. This flexibility explains why MTH1 is so efficient at identifying and removing different harmful nucleotides. The breakdown occurs with high precision: MTH1 uses three metal ions working together with an activated water molecule to split the damaged nucleotide, rendering it harmless. These findings show how the enzyme orchestrates complex chemical reactions to protect DNA from mutations.

MTH1 – promising for cancer research

Cancer cells produce large amounts of damaged nucleotides. The guardian enzyme MTH1 normally prevents these faulty building blocks from being incorporated into DNA. In cancer cells specifically, inhibition of MTH1 leads to an accumulation of damaged nucleotides, causing DNA damage and ultimately the death of the cancer cell. Normal cells are less affected because they produce fewer damaged nucleotides. This difference makes guardian enzyme a promising target for selective cancer therapy. At the same time, boosting MTH1 in healthy cells may help protect DNA and could potentially slow ageing-related diseases such as Alzheimer's and Parkinson's.

K. Hirata, K. Fujimiya, A. Ostermann, T.E. Schrader, T. Hiromoto, M. Goto, T. Arimori, Y. Hirano, K. Kusaka, T. Tamada, T. Nakamura, Neutron and time-resolved X-ray crystallography reveal the substrate recognition and catalytic mechanism of human Nudix hydrolase MTH1, PNAS 122(29), e2510085122 (2025)
DOI: 10.1073/pnas.2510085122

Measurements with neutrons were carried out at BIODIFF at MLZ and BL03 iBIX at J-PARC.

RAPESEED PROTEIN – A KEY TO PLANT-BASED EMULSIONS!

Cruciferin, a protein derived from rapeseed, can stabilise oil-water mixtures – making it ideal for vegan products. This plant-based protein has the potential to make our diets more sustainable and diverse.

Cruciferin, the main storage protein in rapeseed, possesses functional properties that make it particularly well-suited for use in plant-based emulsions, such as beverages, dressings, or meat and dairy alternatives. Small-angle neutron and X-ray scattering, together with neutron spin echo spectroscopy, have shown that Cruciferin retains a trimeric structure at the oil-water interface and forms networks with flexible "arms," resulting in elastic, gel-like films. These molecular properties help enhance interfacial stability and prevent phase separation – a key mechanism for sustainable protein-based technologies.

From molecular insights to next-generation plant-based products

Rapeseed is a globally cultivated oil crop with a high protein content, traditionally used primarily for animal feed. However, plant proteins like rapeseed Cruciferin can play a significant role in the diets of the future, as they contain essential amino acids and can complement or replace other plant based protein sources such as soy. The challenging task is to find and extract the right protein source for applications in food, healthcare and pharmacy with the desired functionality. This requires molecular understanding of all interactions between oils, solvents, proteins and other constituents.

Towards a more sustainable global protein supply

Rapeseed proteins hold great potential for applications in food, but require further understanding for the right molecular functionality such as emulsion stabilisation properties. These insights deepen the molecular understanding of proteins at oil-water interfaces and pave the way for developing new plant-based emulsion products – a step toward a more sustainable global protein supply.

O. Holderer et al., Dynamic Interfacial Architectures: Cruciferin-Stabilized Oil/Water Interfaces for Sustainable Emulsions, Adv. Mater. Interfaces 12(17), e00368 (2025)
DOI: 10.1002/admi.202500368

Measurements were conducted at SANS-1 at PSI, KWS-X at MLZ and SNS-NSE at ORNL.

METALLIC SUDDENLY BECOMES INSULATING

One material, two states: both conductive and insulating. Rare earth nickelates such as lanthanum nickel oxide ($LaNiO_3$) change their behaviour as soon as hydrogen enters the material. This reversible phase transition could enable sensors, memory devices and smart materials of the future.

Modern materials continue to surprise with unexpected properties. Nickelates are unusual materials in which electrons react very sensitively to small changes. When hydrogen enters the material, electrical resistance changes from very low (metallic state) to very high (insulating) and back. Exposing the material to hydrogen gas allows the flow of electrons to be adjusted, almost akin to turning a knob. Nickelates such as $LaNiO_3$ illustrate how closely chemical processes and electronic properties are linked.

Changing electronic states

The key point is that hydrogen does not act alone. As it moves into the nickelate, it simultaneously bonds oxygen within the material. This exchange alters the structure and, consequently, the conductivity. Metallic, insulating, metallic again. The material changes its “electronic state” depending on the hydrogen content. These reversible phase transitions show how small chemical changes can have large effects on electron motion. The phenomenon is studied using high-resolution in situ techniques such as neutron reflectometry and X-ray absorption spectroscopy. Combining structural and electronic analysis allows for a detailed understanding of the mechanisms controlling the metal-insulator transition.

When hydrogen controls electrons

The ability to deliberately change the electrical state opens up many possible applications in the future. Nickelates such as $LaNiO_3$ could in future serve as hydrogen sensors, chemically controlled switches, or novel memory elements that operate at room temperature. Controlled hydrogen incorporation may also be relevant for energy technologies, for example to optimise catalysts for hydrogen production or fuel cells. Understanding proton motion and oxygen dynamics could therefore lead to new concepts for adaptive, switchable materials.

L. Guasco, R. Pons, D. Cortie, L. J. Bannenberg, P. Wochner, E. Goering, P. Nagel, S. Schuppler, S. Hayashida, R. Merkle, B. Keimer, T. Keller, E. Benckiser, Understanding the Role of Hydrogen and Oxygen in Electronic Phase Changes of Nickelates, Adv. Funct. Mater. 35, 2419253 (2025)
DOI: 10.1002/adfm.202419253

Measurements were carried out at SPATZ at ANSTO, ROG at TU Delft, NREX at MLZ and MPI-FKF and WERA at KIT.

HOW INTELLIGENT WERE OUR ANCESTORS?

230 million years ago, *Massetognathus pascuali* shared the world with the first dinosaurs. Its small brain and senses reveal how early relatives of mammals took the first steps towards complex behaviour and survival.

In the late Triassic, *Massetognathus pascuali*, an early relative of today's mammals, roamed the Earth. About the size of a dog, it belonged to the cynodonts, meaning "dog-toothed." Herbivorous and up to 70 centimetres long, it had hairless, reptile-like skin. Despite its reptilian appearance, it played a key role in mammalian evolution. Neutron tomography offers insights into why these animals managed to survive the Triassic.

Secrets in the skull

Particularly fascinating is the head of *Massetognathus pascuali*. Neutron tomography produced precise 3D models of the skull, brain cavity, and nerve pathways. The brain was small relative to the body, elongated in shape, and grew little during its life, although early structures such as the neocortex were already forming. The branched nervous system in the upper jaw indicates that the snout and possible tactile organs, such as whiskers, were still barely mobile. These details reveal how the brain and senses enabled perception, movement, and behaviour – foundations likely crucial to survival, even during the mass extinction at the end of the Triassic.

From the Triassic to mammals: Understanding evolution

The results provide insights into how the brains and senses of our earliest ancestors developed step by step. High-resolution images reveal even the smallest details and show which adaptations facilitated survival in the late Triassic. Future analyses could provide further puzzle pieces to better understand the evolution of perception, movement, and survival strategies in mammals.

T. G. Medina, A. G., Martinelli, L. C. Gaetano, L. Roese-Miron, A. Tartaglione, A. Backs, F. E. Novas, L. Kerber, Revisiting the neuroanatomy of Massetognathus pascuali (Eucynodontia: Cynognathia) from the early Late Triassic of South America using Neutron Tomography, Sci. Nat., 112, 7 (2025) DOI: 10.1007/s00114-024-01955-z

Measurements were carried out at ANTARES at MLZ.

CULTURAL HERITAGE

SILICON BOOSTS ENERGY, CHALLENGES STABILITY

Lithium-ion batteries power our devices and vehicles every day, but they still have limits. Silicon could make lithium-ion batteries far more powerful, but its expansion creates stress inside the anode. Understanding these effects is key to longer-lasting, higher-capacity energy storage for vehicles and devices.

Lithium-ion batteries are everywhere, from smartphones and laptops to electric vehicles and renewable energy grids. Yet even these ubiquitous power sources have limits in how much energy they can store, how fast they charge, and how long they last. Adding silicon to traditional graphite anodes offers a way to push those limits. Batteries with silicon could store far more energy, potentially extending driving ranges, powering devices longer, and making renewable energy storage more efficient.

Material behaviour under the microscope

Silicon expands strongly during charging, up to 300 percent, which creates mechanical stress and can gradually damage the electrode structure. Operando techniques, such as neutron powder diffraction and X-ray computed tomography, allow direct observation of these changes inside the battery while it operates. Lithium first enters the silicon before reaching the graphite. This delayed uptake can increase capacity but also leads to uneven lithium distribution and micro-cracks in the material, which ultimately reduce the battery's lifespan and performance.

Future prospects for energy storage

Batteries with higher silicon content could extend the range of electric vehicles, reduce charging times, and improve the utilisation of renewable energy. Used vehicle batteries could even be repurposed for stationary storage, giving them a second life and maximising their value. A better understanding of silicon's behaviour could lead to safer, higher-capacity batteries that transform e-mobility, portable devices, and renewable energy systems.

T. Hölderle, D. Petz, V. Kochetov, V. Baran, A. Kriele, Z. Hegedüs, U. Lienert, M. Avdeev, P. Müller-Buschbaum, A. Senyshyn, Structural Response of Silicon-containing Graphite Anodes On Lithium Intercalation, Energy Storage Mater. 75, 104042 (2025)
DOI: 10.1016/j.ensm.2025.104042

Measurements were carried out at ECHIDNA at ANSTO, SPODI at MLZ and P21.2 at PETRA at DESY.

NEW BATTERIES WITHOUT LITHIUM

Lithium is expensive and scarce. But inside new materials, an alternative emerges: sodium-ions. If they move particularly quickly in solid-state materials, batteries could be developed that are safer, longer-lasting, and more affordable for electric vehicles and sustainable energy storage.

Modern batteries must be safe, powerful, and durable at the same time. Lithium-ion systems are widespread but reaching their limits. Lithium is costly and limited, and liquid electrolytes are sensitive to heat and can be flammable. Sodium-ion batteries offer an attractive alternative. For high-performance batteries, it is crucial how sodium ions move and how changes in the material's structure affect energy transfer.

Optimising ion movement

NASICON stands for "sodium superionic conductor" and refers to ceramic solid-state materials with a stable metal-oxygen framework in which sodium ions are particularly mobile. The ions move in two ways: short, local jumps within small cages and longer movements through the material. The structure and composition of the material, as well as temperature changes, can influence the ions' pathways. Furthermore, targeted doping with elements such as scandium or aluminum/yttrium can stabilise the structure, shift the phase transition, and enhance the mobility of sodium. Neutron measurements with the so-called quasi-elastic neutron scattering technique provide crucial insights where and how fast the sodium ions move. Such information enables the development of materials for more efficient and stable ion transport.

Next-generation batteries

Sodium has a lower energy density than lithium. This means sodium-ion batteries store less energy than lithium-ion batteries. Current research focuses on increasing this energy density. It also aims to reduce charging times and extend battery life. Safety is another key goal, especially reducing the risk of fire. If these challenges are addressed, sodium-ion batteries could become a stable and environmentally friendly alternative to lithium-ion systems.

I. Pivarnikova, S. Seidlmayer, M. Finsterbusch, G. Dück, N. Jalarvo, P. Müller-Buschbaum, R. Gilles, Understanding the structure and mechanism of Na^+ diffusion in NASICON solid-state electrolytes and the effect of Sc and Al/Y-substitution, J. Mater. Chem. A 13, 14353 (2025)
DOI: 10.1039/D5TA00826C

Measurements with neutrons were carried out at BASIS at ORNL.

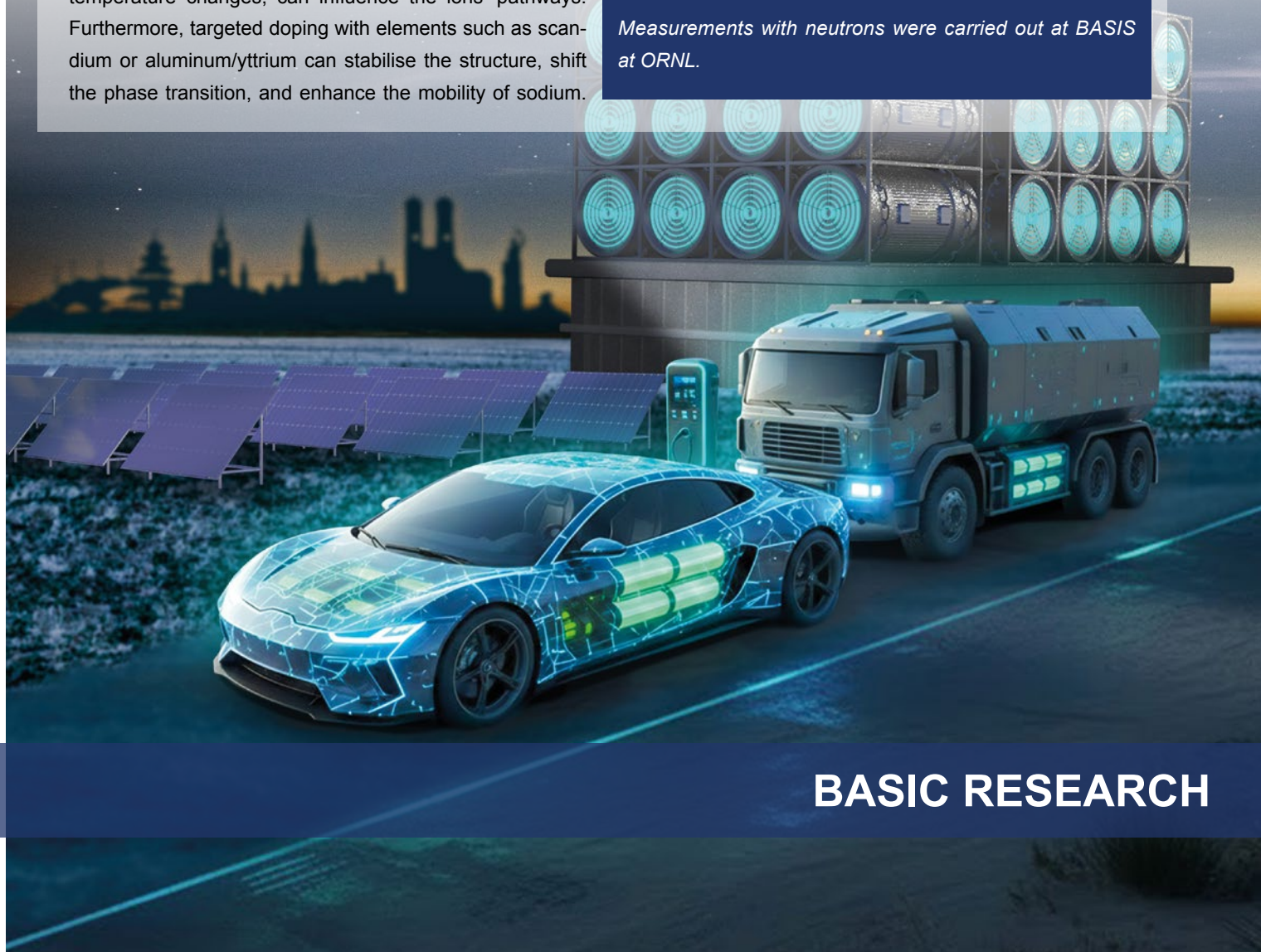

Scientific Reports

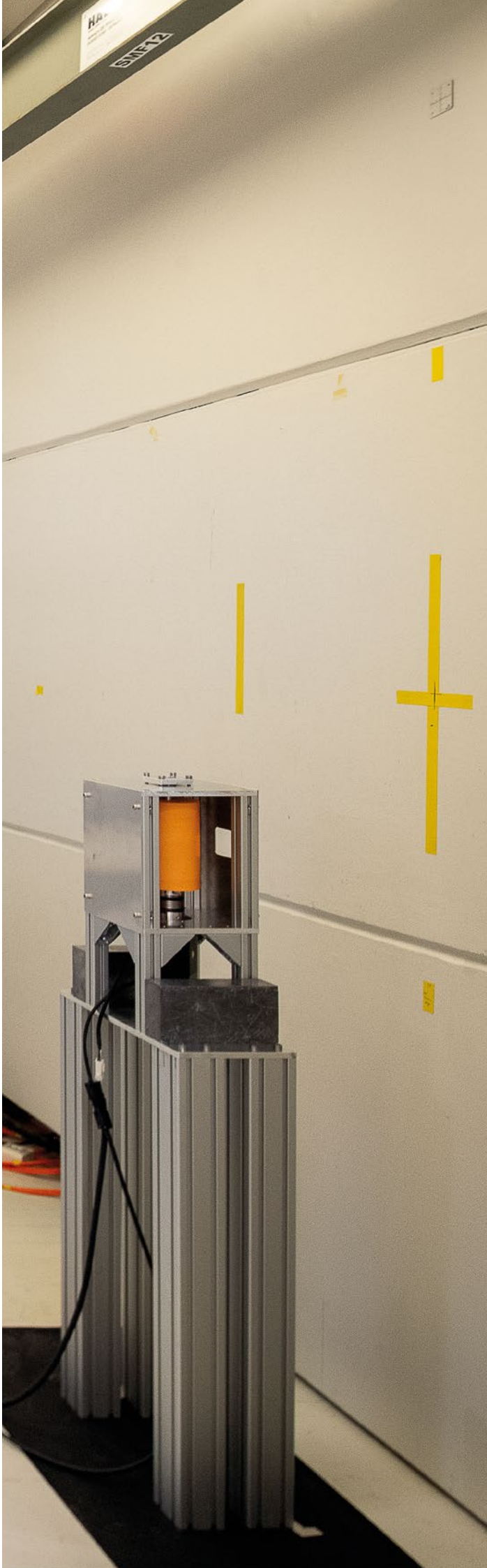

Lithium loss in 5 Ah multilayer pouch cells with silicon-dominant anodes and NCA cathodes

R. Gilles[1], T.A. Pham[1,5], S. Friedrich[2], A. Sommer[2], C. Didier[3], B. Maroti[14], A. Jossen[2], V.K. Peterson[3], P. Müller-Buschbaum[5]

[1]Heinz Maier-Leibnitz Zentrum (MLZ), Technical University of Munich, Garching, Germany; [2]Institute for Machine Tools and Industrial Management, TUM School of Engineering and Design, Technical University of Munich, Garching, Germany; [3]Australian Centre for Neutron Scattering, Australian Nuclear Science and Technology Organisation, Lucas Heigts, Australia; [4]Budapest Neutron Centre, HUN-REN Centre for Energy Research, Budapest, Hungary; [5]Department of Physics, TUM School of Natural Sciences, Technical University of Munich, Garching, Germany

Cyclic ageing leads to lithium (Li) loss in the silicon-containing (Si) anode of $LiNi_{0.8}Co_{0.15}Al_{0.05}O_{1.985}$ (NCA) cells. Multilayer pouch cells featuring NCA cathodes and Si-dominant anodes are compared at the beginning of life and at the state of health at 70 %. To investigate the underlying structural changes, operando neutron diffraction is used to study the cells during cycling and to identify structural changes in the NCA cathode associated with Li loss.

Silicon-dominant anodes

One of the major developments over the past decades has been the exploration of silicon as an anode active material. Silicon forms the $Li_{15}Si_4$ phase at full lithiation, yielding an almost ten times higher gravimetric capacity of 3579 mAh/g at room temperature compared to traditional graphite anodes, making silicon additives an attractive option for increasing battery energy density.

Operando neutron diffraction

The ageing and cycling behaviour of multilayer pouch cells with NCA and Si-dominant electrodes was investigated using operando neutron diffraction (ND), enabling the degree of NCA lithiation to be followed through changes in lattice parameters. The results emphasise the importance of studying large-format full cells to understand degradation mechanisms and identify potential routes for improvements at the material level that can translate to the cell level. Since cell fabrication was carried out in-house, the chemical composition is well known, and the cycling procedure is well documented, the analytical methods could be combined with the electrochemical data to gain further insight into cell degradation.

Li loss

A gradual decrease in the lithiation of the NCA cathode in the discharged state, estimated from the transferred charge, was observed with ageing, suggesting a progressive Li trapping in the Si-containing anode. Operando ND on the multilayer pouch cells at the beginning of life (BOL) and end of life (EOL) were performed at Wombat, ANSTO, and confirmed discharge fading of the NCA cathode. Shifts of the NCA 003 and 113 reflections during cycling are smaller for the EOL cell than for the BOL cell, which can be traced back to the decreased Li inventory. From the evolution of the NCA lattice parameters, the lithiation degree in the discharged state is shifted to higher x values with ageing (Fig. 1, left), consistent with the electrochemical data. Elemental analysis via prompt gamma activation analysis at the Budapest Neutron Centre performed on both electrodes confirmed the Li loss from NCA at EOL, while more Li was found to be trapped in the Si-containing anode compared to BOL (Fig. 1, right). Continuous solid-electrolyte interphase formation is considered one of the leading causes of Li loss.

[1] T.A. Pham et al., Understanding lithium loss in 5 Ah multilayer pouch cells with silicon-dominant anodes and NCA during cyclic ageing, J. Power Sources 654, 237769 (2025) DOI: 10.1016/j.jpowsour.2025.237769

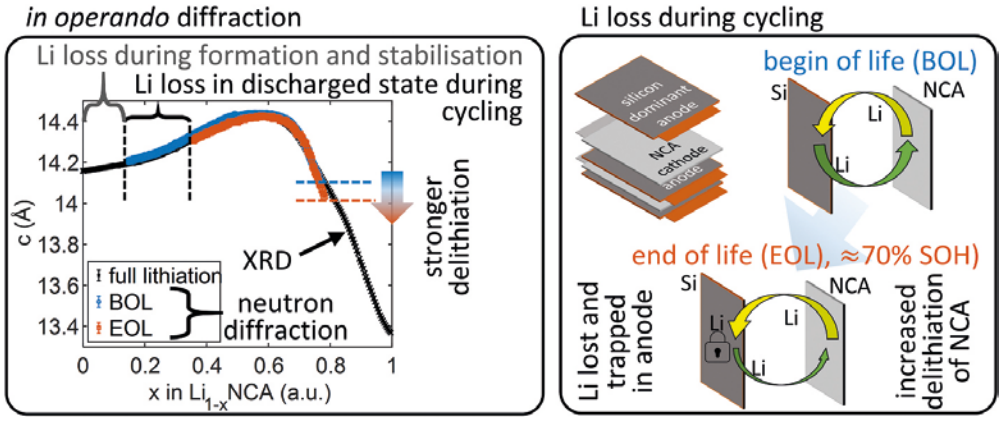

Figure 1: (left) Evolution of the c lattice parameter as a function of NCA lithiation during C/10 charging for beginning (blue) and end of life (red) as determined from neutron powder diffraction; (right) scheme of Li loss during cycling, illustrating Li trapping in the anode and increased delithiation of the NCA cathode.

Influence of hydrogen on the γ-matrix lattice parameters of a Ni-based superalloy

M. Fritton[1], A. Mutschke[1], O. Nagel[2], A. Stark[3], M. Hafez Haghighat[4], B. Gehrmann[4], S. Neumeier[2], R. Gilles[1]

[1]Heinz Maier-Leibnitz Zentrum (MLZ), Technical University of Munich, Garching, Germany; [2]Department of Materials Science and Engineering, Friedrich-Alexander University Erlangen-Nürnberg, Erlangen, Germany; [3]Helmholtz-Zentrum hereon GmbH, Geesthacht, Germany; [4]VDM Metals International GmbH, Frankfurt am Main, Germany

Hydrogen uptake in the Ni-based superalloy (VDM® Alloy 780) was investigated using electrochemical charging and high-energy synchrotron diffraction at the HEMS beamline at PETRA III, DESY. Interstitial hydrogen caused a slight lattice expansion that vanished during in situ heating, demonstrating reversible hydrogenation. Hot-gas extraction measurements confirmed increasing hydrogen content with longer charging times and highlighted the critical role of the effusion temperature.

Hydrogen leaves a fingerprint in the crystal lattice

Hydrogen embrittlement remains a key challenge for metallic materials in hydrogen-based energy systems. Hydrogen is difficult to detect directly with X-rays due to its low atomic scattering power and low concentrations (ppm range). In this work, we use high-energy synchrotron X-ray diffraction (HEXRD) as an indirect but highly sensitive probe to detect hydrogen through its impact on the crystal lattice of solution-annealed VDM® Alloy 780.

Electrochemical hydrogen charging leads to a measurable expansion of the γ-matrix lattice parameter. With increasing charging time, the lattice parameter increases until saturation is reached, consistent with hydrogen occupying interstitial sites in the face-centred cubic lattice (Fig. 1). Although hydrogen primarily enters near-surface regions, the high precision of HEXRD allows detection of even small average lattice changes in bulk measurements.

Reversible hydrogen uptake

In situ heating experiments reveal that the hydrogen-induced lattice expansion is fully reversible. Upon heating, the lattice parameters of hydrogen-charged and reference samples converge at around 500 °C, indicating thermally activated hydrogen effusion (Fig. 1). Complementary hot-gas extraction measurements confirm increasing hydrogen release with temperature and support the interpretation that weakly bound interstitial hydrogen leaves the lattice at moderate temperatures.

Mechanical properties

Mechanical testing shows only a minor reduction in ductility for hydrogen-charged specimens, consistent with hydrogen being confined to near-surface regions. Fractographic analysis confirms a localised brittle fracture mode near the surface, while the bulk remains ductile. Overall, this study demonstrates that synchrotron diffraction provides a powerful, non-destructive tool to track hydrogen in metals and to distinguish reversible lattice effects from hydrogen trapped at stronger binding sites.

[1] M. Fritton et al., Influence of hydrogen on the γ-matrix lattice parameters of a Ni-based superalloy – A synchrotron diffraction study, J. Alloy. Compd. 1014, 178693 (2025) DOI: 10.1016/j.jallcom.2025.178693

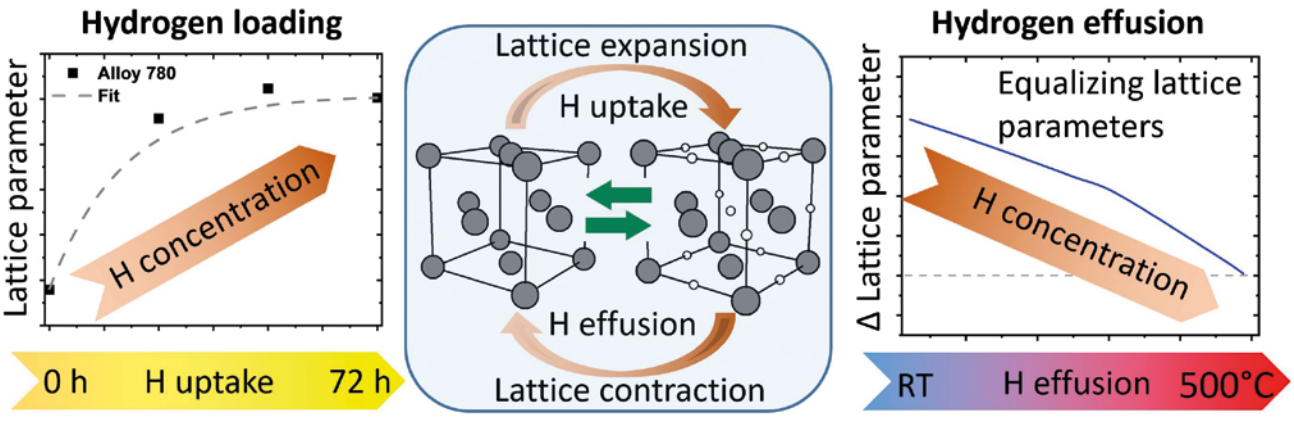

Figure 1: Hydrogen uptake and effusion in VDM® Alloy 780 visualised via lattice parameter evolution. Electrochemical charging expands the γ-matrix lattice parameter; in situ heating reverses this effect, indicating thermally activated hydrogen release.

How hydrogen localises in CoNiCr superalloys and triggers embrittlement at critical microstructural sites

O. Nagel[1], M. Fritton[2], A. Mutschke[2], M. Spörlein[1], A. Stark[3], D. Cheptiakov[4], C. Höschen[5], P. Felfer[1], R. Gilles[2], S. Neumeier[1]

[1] Department of Materials Science and Engineering, Institute I: General Materials Properties, Friedrich-Alexander-Universität Erlangen-Nürnberg, Erlangen, Germany; [2] Heinz Maier-Leibnitz Zentrum (MLZ), Technical University of Munich, Garching, Germany; [3] Institute of Materials Physics, Helmholtz-Zentrum hereon GmbH, Geesthacht, Germany; [4] Laboratory for Neutron Scattering and Imaging, Paul Scherrer Institute (PSI), Villigen, Switzerland; [5] Department of Life Science Systems, TUM School of Life Sciences, Technical University of Munich, Freising, Germany

Hydrogen embrittlement limits the safe use of advanced superalloys in hydrogen-rich environments. Using NanoSIMS, synchrotron and neutron diffraction, and tensile testing, this study reveals that hydrogen preferentially accumulates in the μ phase of a CoNiCr-based superalloy. Local lattice expansion and increased γ/γ′ misfit promote crack initiation and interfacial fracture, explaining the pronounced loss of ductility after hydrogen charging.

Where hydrogen accumulates in the microstructure

Hydrogen embrittlement remains difficult to predict because hydrogen is hard to detect and interacts selectively with microstructural features. In a γ/γ′-strengthened CoNiCr-based superalloy, we combined spatially resolved hydrogen mapping with diffraction-based lattice analysis to identify where hydrogen resides and how it weakens the alloy (Fig. 1). NanoSIMS measurements clearly show that hydrogen concentrates most strongly in the μ phase, a grain-boundary pinning phase that already acts as a preferred crack initiation site (Fig. 1a).

Lattice strain is indirectly linked to hydrogen distribution

Synchrotron (HEMS beamline at PETRA III, DESY) and neutron diffraction (HRPT at SINQ, PSI) reveal that hydrogen uptake causes measurable lattice expansion and increased microstrain (Fig. 1d – e). Neutron data further indicate that the γ′ phase expands slightly more than the γ phase, leading to a small increase in γ/γ′ lattice misfit. Tensile tests show a significant reduction in elongation at fracture after hydrogen charging (Fig. 1c), even after long room-temperature storage when the overall hydrogen content has decreased. This demonstrates that hydrogen trapped at energetically deep sites – μ phase particles and γ/γ′ interfaces – dominates embrittlement. EBSD analysis confirms a transition from mainly intergranular cracking in uncharged material to additional transgranular cracking after hydrogen exposure (Fig. 1b). Together, the results show that localised hydrogen trapping, not bulk hydrogen content, controls embrittlement in this alloy [1].

[1] O. Nagel et al., Impact of high-pressure hydrogen charging on mechanical behaviour and lattice parameters of a polycrystalline CoNiCr-based superalloy, Scr. Mater. 260, 116594 (2025)

DOI: 10.1016/j.scriptamat.2025.116594

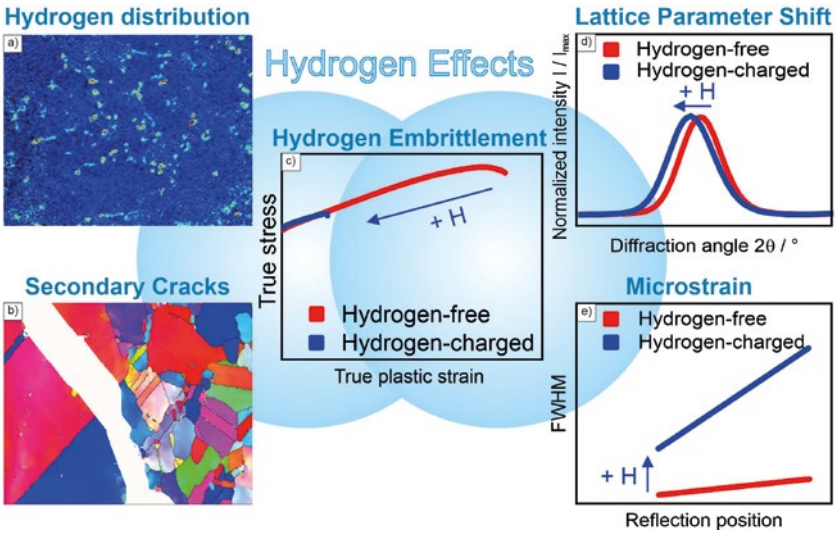

Figure 1: Combined NanoSIMS, synchrotron and neutron diffraction, and tensile testing elucidate the mechanisms of hydrogen embrittlement in a CoNiCr-based superalloy. NanoSIMS measurements (a) reveal preferential hydrogen accumulation in the μ phase, while diffraction results (d – e) demonstrate hydrogen-induced lattice expansion and increased microstrain within the combined γ/γ′ phase. These hydrogen-related lattice distortions promote transgranular cracking after hydrogen charging (b), which ultimately contributes to hydrogen embrittlement (c).

Lattice-driven gating in a Cu-based ZIF for high temperature hydrogen isotope separation

M. Jung[1], J. Park[1], R. Muhammad[1], T. Park[2], S.Y. Jung[1], J. Yi[1], C. Jung[3], J. Ollivier[4], A.J. Ramirez-Cuesta[5], J.T. Park[6], J. Kim[3], M. Russina[7], H. Oh[1,2]

[1]Department of Chemistry, Ulsan National Institute of Science and Technology (UNIST), Ulsan, Republic of Korea; [2]Graduate School of Carbon Neutrality, Ulsan National Institute of Science and Technology (UNIST), Ulsan, Republic of Korea; [3]Department of Chemistry, Soongsil University, Seoul, Republic of Korea; [4]Institut Laue-Langevin (ILL), Grenoble, France; [5]Neutron Scattering Division, Oak Ridge National Laboratory, Oak Ridge, Tennessee, USA; [6]Heinz Maier-Leibnitz Zentrum (MLZ), Technical University of Munich, Garching, Germany; [7]Helmholtz-Zentrum Berlin für Materialien und Energie, Berlin, Germany

A copper-based zeolitic imidazolate framework shows kinetic quantum sieving (KQS) for hydrogen isotope separation at temperatures above 120 K, unlike typical KQS systems which operate below 77 K. Its narrow 2.4 Å pores create a temperature-dependent diffusion barrier through lattice-driven gating. Quasi-elastic neutron scattering (QENS) at IN5 (ILL) and X-ray diffraction confirm distinct isotope mobility and lattice expansion, enabling isotope separation at temperatures of the LNG cryogenic infrastructure.

The usage of deuterium enhances the durability of semiconductor and display devices, which boosts industrial demand for energy-efficient hydrogen isotope separation. However, separation remains challenging due to the almost identical physicochemical properties of hydrogen isotopes. Recently, kinetic quantum sieving (KQS) in confined porous systems has emerged as an effective isotope separation mechanism by exploiting differences in the de Broglie wavelengths of isotopes at cryogenic temperatures. Efficient KQS requires isotope-dependent diffusion barriers; however, achieving sufficient barrier differences above 77 K is difficult. To address this limitation, this study proposes a Cu-based framework that utilises lattice-driven gating for efficient hydrogen isotope separation.

Lattice-driven gating in Cu-ZIF-gis

A copper-based zeolite imidazolate framework, the so-called Cu-ZIF-gis, features a gis-type zeolitic imidazolate framework with an ultranarrow straight channel along the c-axis, whose aperture is smaller than the kinetic diameter of hydrogen isotopes at low temperature (Fig. 1). Temperature-dependent powder X-ray diffraction reveals a gradual and reversible lattice expansion upon heating, inducing a lattice-driven gating effect that increases the effective pore aperture and modulates the diffusion barrier in a temperature-dependent manner.

Hydrogen isotopes diffusion dynamics

QENS experiments were conducted to investigate hydrogen isotope diffusion dynamics in Cu-ZIF. The elastic incoherent structure factors (EISF) for H_2 and D_2 at various temperatures were obtained by fitting the QENS spectra with the diffusion-in-a-sphere model. The analysis reveals a stronger confinement effect for D_2 than for H_2, as evidenced by its smaller localisation radius and reduced mobile fraction, indicating more restricted motion under confinement. As a result, lattice-driven gating in this flexible ZIF induces distinct isotope-dependent diffusion dynamics, enabling efficient hydrogen isotope separation in Cu-ZIF even at LNG-relevant temperatures of 111 K.

[1] M. Jung et al., Lattice-driven gating in a Cu-based zeolitic imidazolate framework for efficient high-temperature hydrogen isotope separation, Nat. Commun. 16, 2032 (2025) DOI: 10.1038/s41467-025-56649-5

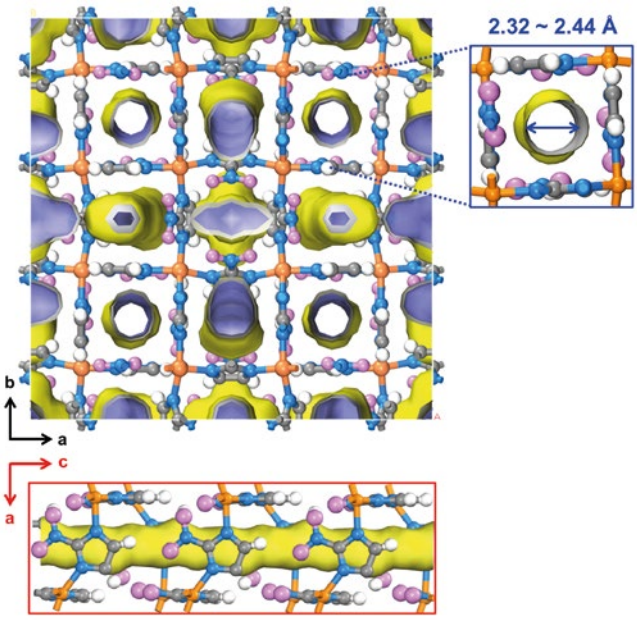

Figure 1: The structure of Cu-ZIF-gis that shows cylindrical straight channels along the c-axis. The pores were calculated with Connolly surfaces with a probe of 1.1 Å. (Cu, orange; N, blue; C, grey; O, magenta; H, white).

Understanding hydrogen effects in hybrid biomedical implants

R. Kumar[1], C. Solis[1], P. Trtik[2], A. Kriele[1], W. Limberg[3], D. C. F. Wieland[3], J. Moosmann[4], M. Serdechnova[5], C. Blawert[5], T. Ebel[3], R. Willumeit-Römer[3], V. M. Garamus[3]

[1] German Engineering Materials Science Centre (GEMS) at MLZ, Helmholtz-Zentrum hereon GmbH, Garching, Germany; [2] Paul Scherrer Institute (PSI), Villigen, Switzerland; [3] Institute of Metallic Biomaterials, Helmholtz Zentrum hereon GmbH, Geesthacht, Germany; [4] Institute of Material Physics, Helmholtz Zentrum hereon GmbH, Geesthacht, Germany; [5] Institute of Surface Science, Helmholtz Zentrum hereon GmbH, Geesthacht, Germany

Hybrid Ti-Mg implants combine the mechanical strength of Ti with the degradability of Mg for temporary support and bone regeneration. Mg degradation releases hydrogen, which can affect Ti stability. Ti64-MgZnCa samples were degraded in saline (0–120 h) and analysed via neutron tomography, synchrotron X-ray diffraction, SEM, and gas fusion. The hydrogen diffused radially, expanding the Ti lattice at room temperature, with no hydride formation.

Hybrid biomedical implants combining permanent and degradable materials are an emerging strategy to improve the performance of medical implants. Systems integrating permanent titanium (Ti) alloys with degradable magnesium (Mg) alloys aim to provide long-term mechanical stability while supporting temporary load bearing and enhanced biological response. As magnesium degrades in physiological environments, it releases hydrogen gas, which may migrate into adjacent titanium components. Understanding these interactions is essential for ensuring the long-term safety, reliability, and clinical viability of hybrid implants.

Advanced imaging and structural analysis

Hybrid samples composed of Ti64 and Mg-Zn-Ca alloys were produced using metal injection moulding. To replicate physiological conditions, the samples were immersed in saline to induce controlled magnesium corrosion (Fig. 1a). As degradation progressed, hydrogen evolved at the interface. The study evaluated hydrogen uptake and distribution in the titanium alloy. Advanced characterisation techniques – including neutron tomography at NEUTRA, PSI, synchrotron X-ray tomography and diffraction at DESY, scanning electron microscopy, and hydrogen content analysis – enabled three-dimensional visualisation and quantitative assessment of the influence of hydrogen on the titanium crystal structure.

Supporting safer design of Ti-Mg implants

The results showed hydrogen diffusion into titanium even at room temperature. Hydrogen was uniformly distributed and not just limited to the surface layer, with variations along height (Fig. 1b). Structural analysis confirmed hydrogen uptake into the β-phase of Ti, causing lattice expansion, but no titanium hydrides were detected. These findings demonstrate that hydrogen from degrading magnesium can alter the Ti crystal structure, which may affect long-term mechanical behaviour and performance. Overall, this work provides valuable guidance for the safe and reliable design of next-generation hybrid biomedical implants.

[1] R. Kumar et al., Characterising effects of hydrogen ingress in Ti-Mg based hybrid implant materials, RSC Adv. 15, 4472 (2025)
DOI: 10.1039/D4RA08586H

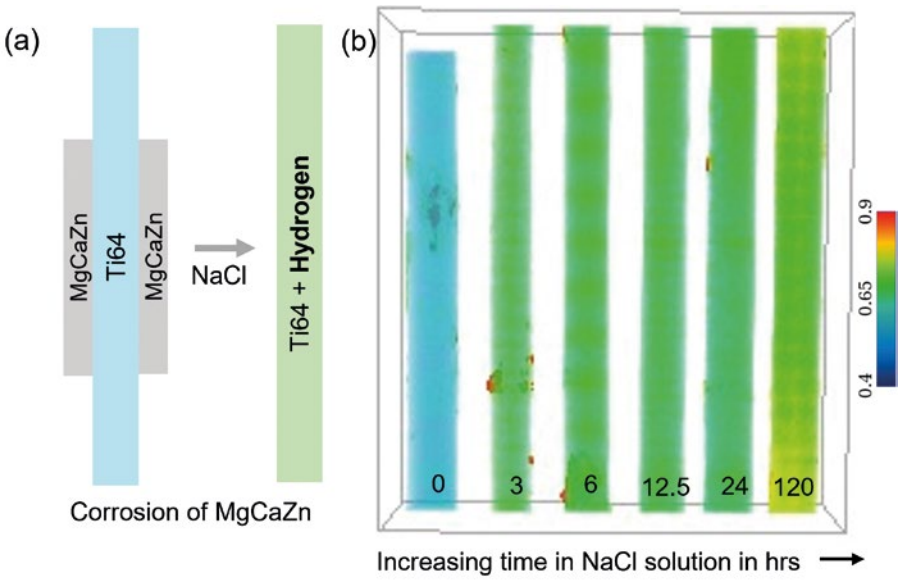

Figure 1: (a) Schematic representation of corrosion of hybrid Ti-Mg samples. (b) Vertical slice extracted from the 3D neutron tomography volume of the samples after different corrosion durations. The colours represent neutron attenuation coefficient values (cm^{-1}).

High temperature dilatometry compression induced α to γ phase and morphology evolutions in TiAl

M. Keita[1,2], C. Solís[1], W.M. Gan[1], J.-F. Moulin[1], Y.D. Zhang[2], E. Bouzy[2]

[1] German Engineering Materials Science Centre (GEMS) at MLZ, Helmholtz-Zentrum hereon GmbH, Garching, Germany;
[2] LEM3, University of Lorraine, Metz, France

Hot compression tests on TNM were performed by the unique GEMS dilatometers available at both MLZ and DESY. A detailed crystallographic study based on in situ diffraction, ex situ pole figures and EBSD of the α and γ phases in the deformed samples revealed that the early formed γ lamellar underwent a morphological transition into the γ nodules as deformation progressed, involving fragmentation, spheroidisation, coarsening and boundary sliding. The insight advances the understanding of TNM for high-performance and high-temperature applications.

The 3rd generation β-solidifying Ti-Al-Nb-Mo-B (TNM) alloys, which are promising for aerospace applications, exhibit remarkable mechanical properties and excellent thermal stability. The performance of TNM is strongly influenced by their microstructural constituents, including lamellar colonies, globular γ, α/α2 and β/β0 components. Hot deformation is commonly used to optimise TNM alloys for different purposes, typically below the (α+β) phase region (below γ- solvus temperature).

Emergence of the instable γ phase during compression

In this study, large strain hot compression was performed using a special modulus of the GEMS dilatometers (DIL805, TA Instruments) available at MLZ. The deformation took place at 1280 °C (in the α+β phase region) with two thickness reductions at a strain rate of 10^{-2} s^{-1}. Unexpectedly, the γ phase (marked within a red oval in Fig. 1a) resurged abnormally from the α phase despite its thermodynamic instability at equilibrium, as shown by high-energy X-ray diffraction (HEXRD) patterns obtained in situ during compression by using a similar dilatometer (at P07 line, DESY) [1].

Hot deformation-induced α → γ transformation and formation of γ nodules

The texture of the α phase exhibits a strong basal fibre (pole figures in Fig. 1b), which indirectly evidences a dominant basal slip of α phase. Besides, EBSD (Fig. 1c) revealed that the transformation follows the Blackburn orientation relationship, and the formation of the γ lamellae is related to the activation of the basal slip system of the α matrix with the highest Schmid factor. It was possible to prove that the early formed γ lamellae underwent a morphology transition to the γ nodules with continuous deformation through fragmentation, spheroidisation, coarsening, and boundary sliding.

This work provided useful information on the underlying mechanism of the hot deformation-induced α → γ transformation and the formation mechanisms of the resultant microstructure, which advances the understanding of TNM alloys for high-performance and high-temperature applications.

[1] M. Keita et al., High-temperature compression induced α to γ phase transformation and related phase morphology transition in TiAl alloy, J. Alloy. Compd. 1042, 184044 (2025) DOI: 10.1016/j.jallcom.2025.184044

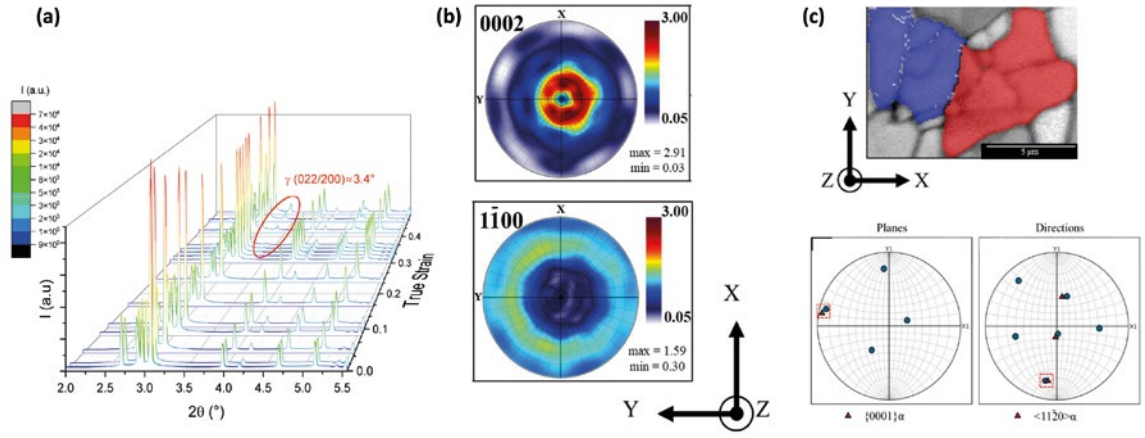

Figure 1: (a) HEXRD patterns of a TNM sample as a function of applied compressive strain up to 40 %; (b) pole figures of the α phase in a fully compressed sample; and (c) SEM-EBSD (top) micrographs of a α (red) and γ (blue) grains, and their direct stereographic projections (bottom) of the Blackburn OR planes and directions, respectively.

Residual stresses in an ITER-like tungsten-monoblock type plasma-facing component

J.-H. You [1], M. Hofmann [2], W. M. Gan [3], R. Coppola [4]

[1] Max Planck Institute for Plasma Physics (IPP), Garching, Germany; [2] Heinz Maier-Leibnitz Zentrum (MLZ), Technical University of Munich, Garching, Germany; [3] German Engineering Materials Science Centre (GEMS) at MLZ, Helmholtz-Zentrum hereon GmbH, Garching, Germany; [4] ENEA-Casaccia, Rome, Italy

The effects of residual stress in dedicated small-scale tungsten mock-up samples of plasma-facing components (PFC) were compared prior to and after being subjected to operational heat loads which were simulated using a high-power neutral hydrogen beam facility available at the IPP Garching. Stress contributions from the manufacturing as well as from the thermal loads were determined non-destructively by means of neutron diffraction measurements.

Divertor targets

In a fusion power reactor, the divertor target is a key in-vessel component playing a crucial role in exhausting “burned-up” particles from the plasma and removing the corresponding heat. Its plasma-facing side is made of tungsten as divertors are supposed to withstand the extremely high heat flux (HHF) during operation. This introduces cyclic thermal stresses in the wall material, which interact with residual stresses from the fabrication process and thus directly affect the lifetime of the component. Therefore, to ensure the structural integrity and reliability of the targets, information on the stress state in such a component and the impact of HHF is essential.

Experiments on mock-up samples

A small-scale mock-up of a tungsten monoblock-type divertor target was fabricated via a hot radial pressing technique to join four tungsten armour blocks to a cooling pipe made of CuCrZr alloy (Fig. 1, left). The thermal load was simulated using the high-power neutral hydrogen beam facility GLADIS at the IPP Garching. Due to the high absorption of X-rays in tungsten, the only possible technique to determine non-destructively the stress profile in such a component are neutrons. Therefore, neutron diffraction measurements were carried out on this mock-up before and after the HHF loading test to measure potential thermal induced changes in stress profiles.

Stress profiles

While the initial residual stress profile was measured only at STRESS-SPEC, the stress distribution after HHF was additionally examined at the RSI instrument (HANARO). The results show a significant increase in compressive stress behaviour close to the interlayer. The good agreement in stress profiles (Fig. 1, right) between the measuring campaigns conducted at different diffractometers indicates a real impact of the cyclic HHF loading on stress whereas the effect of technical errors is deemed minor. In conclusion, this substantial change of stress states in the tungsten armour block during HHF loads must be taken into account in the design process.

[1] J.-H. You et al., Impact of high heat flux loads on the residual stress in a tungsten-monoblock plasma-facing component, Fusion Eng. Des. 212, 114804 (2025)
DOI: 10.1016/j.fusengdes.2025.114804

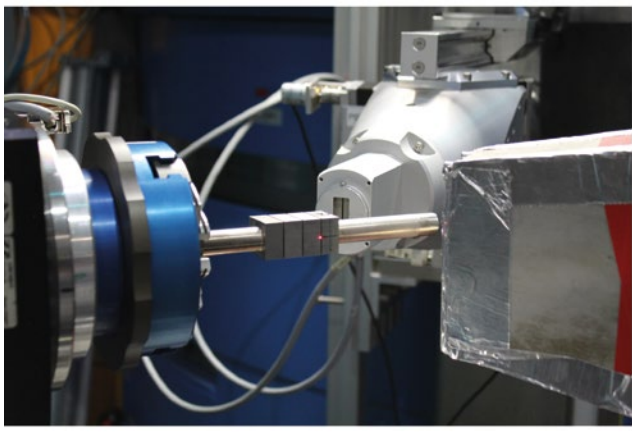

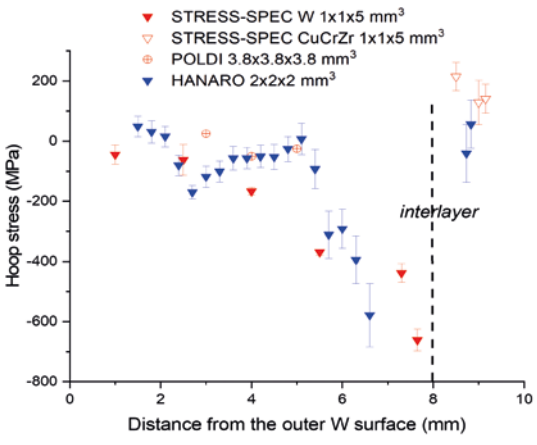

Figure 1: (left) Setup of the mock-up sample at the instrument STRESS-SPEC. (right) Comparison of determined hoop stresses after GLADIS testing. Measurements were undertaken at FRM II (STRESS-SPEC), HANARO (RSI) and additionally at SINQ (POLDI). The gauge volumes used in the respective measurements are indicated in the caption. The line marks the interface to the CuCrZr cooling pipe.

Experimental constraints on the origin of metal and carbon in ureilite meteorites

N. P. Walte [1], M. Collinet [2], C. A. Goodrich [3]

[1] Heinz Maier-Leibnitz Zentrum (MLZ), Technical University of Munich, Garching, Germany;
[2] Institute of Life, Earth, and Environment (ILEE), University of Namur, Namur, Belgium;
[3] Lunar and Planetary Institute, USRA, Houston, Texas, USA

Ureilites are unique meteorites that contain carbon and metal situated in fractures and along the grain boundaries of silicates. It has long been debated whether either phase was endogenous or derived from an external impactor during a destructive collision. Using deformation experiments with SAPHiR, we show that the metal was injected from the impactor and the carbon was part of the original material that accreted in the ureilite parent body.

Ureilites, an enigmatic class of meteorites

Ureilite meteorites are samples from the interior of a planetesimal that formed within the first Myr of our solar system. The parent body suffered a destructive collision ca. 4 Myr later, which reaccreted to a daughter body from which the meteorites that are recovered on Earth are derived. There are many open questions about ureilites, including where the metal and the up to 7 vol% carbon (mainly in the form of graphite) come from and why these phases are present predominantly in fractures and as narrow grain boundary linings between large olivines and pyroxenes (Fig. 1a–d).

Deformation experiments with SAPHiR

In order to explore whether the elongated metal-graphite textures are related to shock deformation during the collision, we performed high strain-rate deformation experiments ($\dot{\varepsilon} \approx 1 \times 10^{-2}\ s^{-1}$) with SAPHiR at a temperature of 1300 °C in a model system composed of olivine, graphite, and FeS melt (analogue for metal melt). To explore the difference between the endogenous or exogenous nature of either phase, we inserted a central cavity filled with either FeS melt or graphite in the centre of the sample that was surrounded by polycrystalline olivine mixed with the other phase (Fig. 1e). Upon deformation, the cavity collapsed and part of the material was injected into the olivine matrix. Our experiments revealed that the two phases spread along olivine grain boundaries, forming linings similar to ureilite textures (Fig. 1f–h).

Metal-graphite textures in ureilites were formed by a cosmic collision

Comparisons between the experiments and ureilites showed that the grain boundary linings were formed by exogenous metal melt that intruded along grain boundaries and mixed with locally deformed graphite. Hence, graphite was likely to be a part of the original ureilite parent body composition; its presence weakened the cohesion of the welded silicate grain boundaries thus promoting dispersive intrusion of the metal melt from the impactor into the mantle during the cosmic collision.

[1] N. Walte et al., Experimental constraints on the origin of metal and carbon in ureilite meteorites, Meteorit. Planet. Sci. 60, 2715 (2025)
DOI: 10.1111/maps.70063

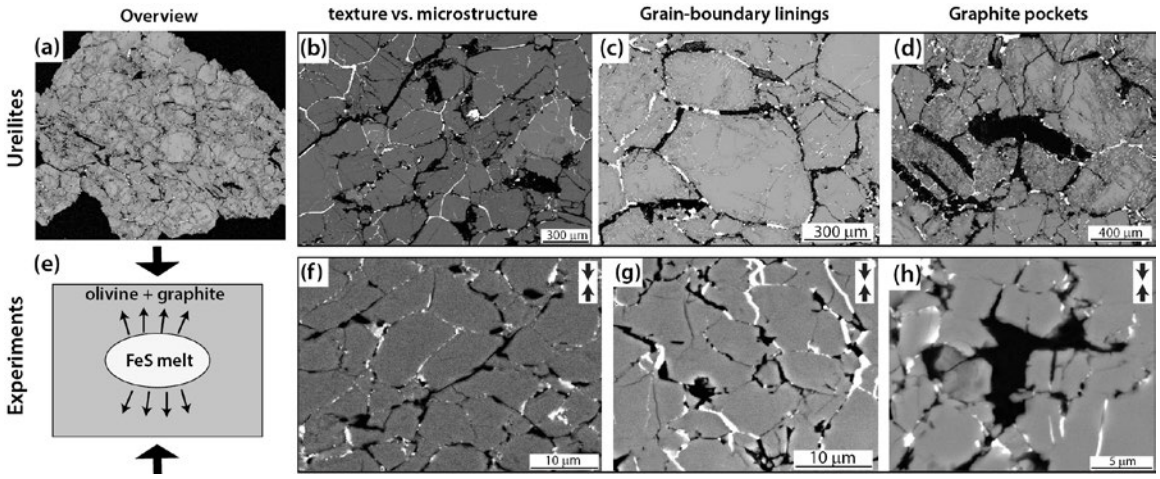

Figure 1: (Top row) Overview (a) and textural details of metal (white) and graphite (black) in silicate grains (grey). (Bottom row) (e) Overview of the sample setup for simulating FeS melt intrusion during deformation. (f–h) Microstructural details of the experiments are similar to the respective ureilite textures above.

Neutron imaging to assess the serial production of electric motors with increased efficiency

P. Stöcks-Morgan [1], T. Neuwirth [2], A. Douiri [3], S. R. Sebold [2], A. Kaestner [4], C. Hartmann [1], N. Leuning [3], M. Schulz [2], W. Volk [1]

[1] Chair of Metal Forming and Casting, TUM School of Engineering and Design, Technical University of Munich, Garching, Germany; [2] Heinz Maier-Leibnitz Zentrum (MLZ), Technical University of Munich, Garching, Germany; [3] Institute of Electrical Machines, RWTH Aachen University, Aachen, Germany; [4] Paul Scherrer Institute (PSI), Centre for Neutron and Muon Sciences, Villigen, Switzerland

Modern electric drives require magnetic anisotropy in the rotor. Typically, this is achieved by cut-out flux barriers that weaken the electrical steel sheets comprising the rotor. Embossed flux barriers offer a magnetically effective and mechanically robust flux-guidance alternative. This study evaluates the transfer to large-scale manufacturing using neutron imaging and demonstrates a straightforward integration into electric drive production.

Electrical steel is used in modern electric machines due to its magnetic properties and is conventionally shear-cut to the desired geometry. Modern machines require high magnetic anisotropies, typically achieved by material removal. While magnetically effective, this weakens the material mechanically. The local micro-embossing of electrical steel introduces steep residual stress gradients that reduce relative permeability due to inverse magnetostriction. This enables mechanically improved rotor geometries, allowing for higher rotational speeds and increased energy density and efficiency. While the technique has been studied at laboratory scale, its transferability to large-scale manufacturing must be assessed to determine industrial applicability.

Neutrons to study magnetic properties

Since flux barriers are highly localised, spatially resolved relative permeability assessment is required, which conventional methods, such as single-sheet testers, cannot provide. Neutrons possess a magnetic moment, enabling them to interact with magnetic structures. Neutron grating interferometry exploits this property to create qualitative maps of the magnetic flux in electrical steel samples.

Straightforward process integration

Exemplifying the transferability of this approach to industry, as demonstrated in the paper, we present our results on the combination of shear cutting and embossing. With shear cutting being the primary method to obtain the rotor geometry, it is imperative that embossing and shear cutting can be performed on the same rotor lamella without disrupting the magnetic flux guidance. In Fig. 1 we compare the dark field image of four differently manufactured electrical steel sheets (shear-cut reference, shear-cut embossed, wire-cut reference and wire-cut embossed). Additionally, we demonstrate free process sequencing and the transferability to industrial high-speed presses. These results enable the straightforward integration of embossed flux barriers into industrial electrical machine manufacturing.

[1] P. Stöcks-Morgan et al., Towards large-scale production of improved magnetic flux guidance structures in non-grain-oriented electrical steel, CIRP Ann-Manuf. Technol. 74, 411 (2025)

DOI: 10.1016/j.cirp.2025.03.021

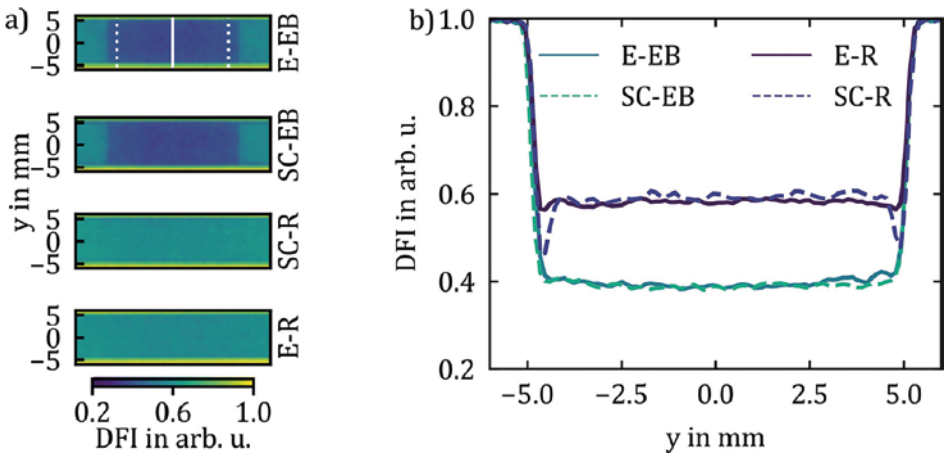

Figure 1: a) Dark field images (DFI), obtained from neutron grating interferometry for four different samples of electrical steel. Sample edges were either shear-cut (SC) or wire-cut (E). Furthermore, these edges were studied solely (R) or with embossing superimposed (EB). b) The DFIs show that a cutting-edge effect is clearly visible in the shear-cut sample but not in the wire-cut, as expected. When superimposed with embossing, neither sample shows a cutting-edge effect. The measurements were performed at the ICON neutron imaging beamline (PSI) using the neutron grating interferometry setup developed at MLZ.

Spatially resolved in situ defect spectroscopy during tensile tests using a scanning positron beam

C. Hugenschmidt[1], M. Thalmayr[1], T. Gigl[1]

[1] Heinz Maier-Leibnitz Zentrum (MLZ), Technical University of Munich, Garching, Germany

We present an in situ defect analysis method during tensile testing using a scanning positron microbeam at our coincidence Doppler broadening spectrometer. Local defect concentrations can be mapped in two dimensions with 250 µm resolution within 35 s. Elastic strain showed no effect whereas plastic deformation was clearly detected, which in turn allows for the prediction of crack initiation at the maximum defect density.

Doppler broadening spectroscopy (DBS) is highly sensitive to open-volume defects that trap thermalised positrons. After implantation, positrons diffuse through the lattice and annihilate with electrons, emitting two 511 keV gamma quanta. The electron momentum at the annihilation site causes Doppler broadening of the annihilation line. Annihilation in vacancies reduces core-electron contributions with high Doppler shifts, leading to line narrowing, which is quantified by the so-called S parameter. Our monoenergetic scanning positron microbeam enables depth- and laterally resolved defect analysis and 3D defect imaging.

Tensile tests set-up in the CDB-spectrometer

The tensile-test machine is integrated into the CDB spectrometer. A monoenergetic positron beam is accelerated by high voltage and focused onto the sample using electrostatic lenses in the ultra-high-vacuum (UHV) system. The annihilation gamma quanta are detected by HPGe detectors. The sample chamber provides sufficient inner diameter to accommodate the tensile stage and beam optics. In the centre of the sample chamber, the specimen is clamped in a sled whose guidance is electrically insulated by PEEK brackets. The sled and moving components are driven by a stepper motor. The applied load is measured by an air-side mounted force gauge. Below the sample, a cylindrical permanent magnet is mounted on an insulator on top of a bar connected to the chamber via bellows. A stepper-motor-driven x – y translator moves the magnet beneath the sample to deflect the positron beam toward the magnet axis. An additional z translator adjusts the magnet-sample distance.

2D-defect mapping during mechanical load

We performed spatially-resolved in situ DBS during tensile loading of AlMg4.5Mn and Al99.5 to correlate atomic-scale defect formation with applied stress and strain. The reduced section of an annealed AlMg4.5Mn sample was scanned at ten deformation stages using the same specimen as for the stress-strain curve (Fig. 1). Two-dimensional defect maps reveal strain localisation, necking, and increased defect density, enabling crack initiation and failure prediction.

[1] C. Hugenschmidt et al., Spatially resolved in situ defect spectroscopy during tensile tests using a scanning positron beam, Physica B 715, 417613 (2025)
DOI: 10.1016/j.physb.2025.417613

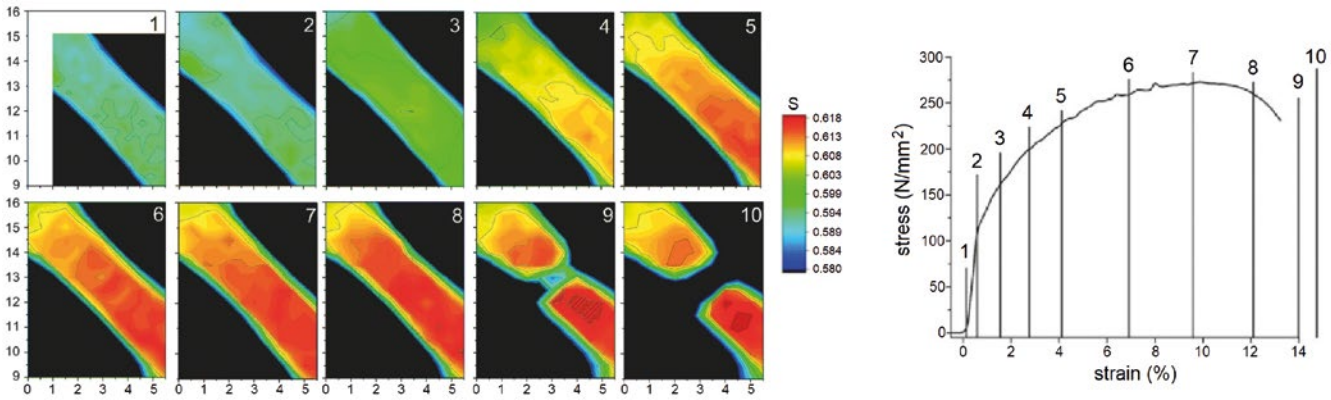

Figure 1: 2D maps of the defect-related S parameter during tensile testing of annealed AlMg4.5Mn at different stages. Coordinates correspond to magnet deflection units (1 unit = 0.83 mm) with a step width of 0.5 mm. Scan (1) shows the undeformed sample, (2) the elastic region, (3) – (8) plastic deformation with necking at (7), and (9) – (10) the fractured state.

Copper precipitation in aluminium alloys observed by coincidence Doppler-broadening spectroscopy and positron annihilation lifetime spectroscopy

L. Mathes[1,2], M. Suhr[1], L. Heinl[3], M. Butterling[4], E. Hirschmann[4], M.O. Liedke[4], C. Hugenschmidt[1]

[1]Heinz Maier-Leibnitz Zentrum (MLZ), Technical University of Munich, Garching, Germany; [2]Department of Physics, School of Natural Sciences, Technical University of Munich, Garching, Germany; [3]Institute of Casting Research, Montanuniversität Leoben, Leoben, Austria; [4]Institute of Radiation Physics, Helmholtz-Zentrum Dresden-Rossendorf (HZDR), Dresden, Germany

The properties of Al alloys are significantly affected by Cu content. We used coincidence Doppler-broadening spectroscopy (CDBS) to study Cu precipitation in T4-treated AlCu (with 1–3 wt.% Cu) and AlCuMg alloys. CDBS reveals the local chemical surroundings of the annihilation site. This allows us to identify positrons trapped in Cu precipitates. We demonstrate that the precipitation increases with higher Cu concentration.

Probing Cu precipitation with SLOPE

AlCu alloys are pivotal in aerospace and automotive engineering due to their high strength-to-weight ratio. Their mechanical properties depend heavily on the microstructure formed during precipitation, specifically the formation of Guinier-Preston (GP) zones. Using the setup for low-energy positron experiments (SLOPE) at MLZ, we employed CDBS alongside positron annihilation lifetime spectroscopy (PALS) at ELBE (HZDR, Dresden) to investigate the microstructures in T4-treated AlCu and AlCuMg alloys [1].

Enhanced sensitivity to local environments

We analysed high-purity AlCu alloys with varying Cu contents (1–3 wt.%) and a commercial AlCuMg alloy. A key advantage of positron annihilation spectroscopy is the high affinity of positrons for Cu. Thermalised positrons are efficiently trapped in Cu-rich precipitates, allowing CDBS to provide background-suppressed information about the local chemical environment.

Our measurements revealed a distinct Cu signature, which intensified as the Cu content increased (Fig. 1). Notably, the “Cu fraction” detected by positrons was significantly higher than the nominal bulk concentration, e.g., 33 % detected in AlCuMg versus a nominal 4 %. This overestimation confirms that CDBS probes the specific local environment of the trap (GP zones), demonstrating exceptional sensitivity to nascent clustering stages often undetectable by other techniques.

Atomic-scale defect characterisation

Complementary PALS measurements confirmed that positrons primarily annihilate in vacancy-like defects. The observed lifetimes (224–232 ps) align with theoretical predictions for vacancy-Cu complexes (V_{Al}–Cu and V_{Al}–2Cu) located at precipitate-matrix interfaces. A systematic reduction in lifetime in correlation with a higher Cu content suggests the formation of larger vacancy-Cu clusters. These findings highlight the capability of SLOPE to resolve atomic-scale precipitation phenomena, offering valuable data for optimising thermal treatments and alloy development.

[1] L. Mathes et al., Copper precipitation in aluminium alloys observed by coincidence Doppler-broadening spectroscopy and positron annihilation lifetime spectroscopy, J. Phys.: Conf. Ser. 3149, 012015 (2025)
DOI: 10.1088/1742-6596/3149/1/012015

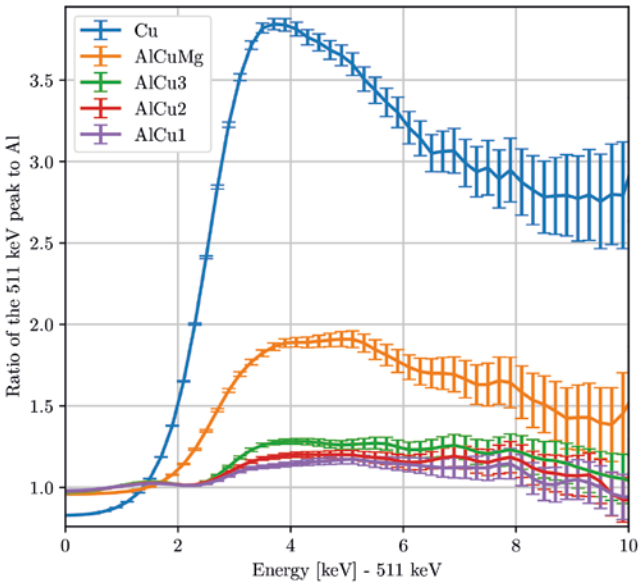

Figure 1: CDBS ratio curves of pure Cu, AlCu alloys (1–3 wt.% Cu), and AlCuMg. Normalised to pure Al, the high-momentum region reveals a distinct Cu signature that intensifies with increasing Cu content. This trend reflects element-specific annihilation characteristics, where higher momentum electrons in Cu contribute more significantly to the Doppler-broadening of the annihilation line compared to Al.

Local crystallisation inside the polymer electrolyte for lithium metal batteries observed by operando nanofocus WAXS

F.A.C. Apfelbeck[1], G.E. Wittmann[2], M.P. Le Dû[1], L. Cheng[1], Y. Liang[1], Y. Yan[1], A. Davydok[3], C. Krywka[3], P. Müller-Buschbaum[1]

[1]Department of Physics, School of Natural Sciences, Technical University of Munich, Garching, Germany; [2]Heinz Maier-Leibnitz Zentrum (MLZ), Technical University of Munich, Garching, Germany; [3]Helmholtz-Zentrum hereon GmbH, Geesthacht, Germany

Nanofocus X-ray wide-angle scattering (nWAXS) is used to detect possible lithium-based crystallites in the polymer-based electrolyte. We perform operando scanning nanofocus wide-angle X-ray scattering on a composite gel-type polymer consisting of poly(vinylidene fluoride-co-hexafluoropropylene) (PVDF-HFP) and the single-ion conducting polymer poly((trifluoromethane) sulfonimide lithium styrene) (PSTFSILi) in a lithium symmetric cell.

In this work, we perform operando scanning nWAXS at room temperature on a symmetric lithium cell with a polymer-based electrolyte (PVDF-HFP/PSTFSILi in a mixture of ethylene carbonate and propylene carbonate (EC/PC)), which is specially designed for synchrotron experiments to spatially and temporally resolve the crystalline structure of the electrolyte on a nanoscale (Fig. 1). With such an approach, we are able to identify rare crystallisation events in the early stages of cell operation. Besides detecting metallic lithium in the polymer electrolyte, we observe the unexpected local kinetics of lithium carbonate and lithium hydroxide inside the polymer during three half-cycles (plating, stripping, plating) over a depth of approximately 16 µm.

Obstacles for lithium-ion transport

As expected, the overpotential of the operando cell is high. In general, the observed crystallites inside the polymer-based electrolyte can be responsible for the higher ionic bulk resistance of the lithium symmetric cell compared to the stainless-steel cell, as they can act as an ion-conducting barrier. Therefore, the movement of the lithium ions can be hindered, especially as the ionic conductivity of bulk LiOH at room temperature is quite low. Li_2CO_3 and LiOH are an essential part of the SEI layer and the native passivation layer of the lithium metal electrode surface. Consequently, considering the solubility of Li_2CO_3 and LiOH in EC and PC, which is rather high compared to other SEI layer compounds, a possible explanation for the presence of these compounds can be given: Due to the contact of the lithium electrode with the soaked electrolyte film, the crystallites of the lithium surface can be dissolved, forming CO_3^{2-}, OH^-, and Li^+, which diffuse into the electrolyte.

We observe the early stages of the formation of pure metallic lithium inside the electrolyte, which is not necessarily connected to the lithium metal surface but can lead to dendritic structures. With our work using nano-sized X-ray beams, we open up the opportunity to further understand the components of lithium batteries and, in the next step, create better batteries.

[1] F. Apfelbeck et al., Local crystallisation inside the polymer electrolyte for lithium metal batteries observed by operando nanofocus WAXS, Nat. Commun. 16, 8958 (2025) DOI: 10.1038/s41467-025-64736-w

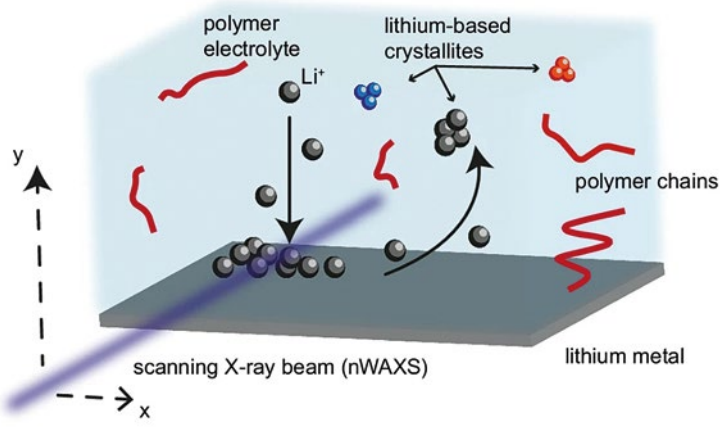

Figure 1: Illustration of the synchrotron experiment. The nano-sized X-ray beam penetrates and scans the polymer electrolyte during electrochemical cycling at room temperature.

Evaluating oxide nanoparticle exsolution by ex situ SAXS/WAXS analysis

A. J. Carrillo [1], M. Balaguer [1], C. Solís [2], A. López-García [1], S. Haas [3], M. Fabuel, B. Delgado-Galicia [1], I. Rodriguez [1], E. Vøllestad [4], S. Wachowski [5], R. Strandbakke [4,6], T. Norby [6], J. M. Serra [1]

[1] Instituto de Tecnología Química, Universitat Politècnica de València, Consejo Superior de Investigaciones Científicas, Valencia, Spain; [2] German Engineering Materials Science Centre (GEMS) at MLZ, Helmholtz-Zentrum hereon GmbH, Garching, Germany; [3] Deutsches Elektronen Synchrotron (DESY), Hamburg, Germany; [4] Sustainable Energy Technology, SINTEF Industry, Oslo, Norway; [5] Institute of Nanotechnology and Materials Engineering, Faculty of Applied Physics and Mathematics, and Advanced Materials Centre, Gdansk University of Technology, Gdansk, Poland; [6] Department of Chemistry, University of Oslo, Centre for Materials Science and Nanotechnology, Oslo, Norway

Oxide nanoparticle exsolution in double perovskites for proton ceramic electrochemical electrodes was investigated under reducing conditions. The effects of A-site deficiency and exsolution temperature were analysed by conventional techniques and synchrotron-based SAXS. Unlike metal exsolution, A-site deficiency had little impact, while higher temperatures increased particle size, highlighting the complexity of oxide exsolution.

Nanoparticle exsolution is an effective strategy for functionalising redox oxides in high-temperature energy applications, such as fuel cells and electrolysers. While metallic nanoparticle exsolution is well studied, the exsolution of multicomponent oxide nanoparticles, capable of forming different compositions with diverse electrocatalytic properties, remains poorly understood and largely unexplored.

Tuning oxide exsolution in PBC double perovskites

Oxide exsolution from $PrBa_{1-x}Co_2O_{6-\delta}$ (PBC) double perovskites has been evaluated, paying particular attention to the effects of A-site deficiency and variations in the temperature treatment on the nanoparticle properties. Nanoparticles of different shapes and compositions ($BaCoO_3$, Co_3O_4, and $BaCO_3$) were observed via TEM and SEM, and corroborated by Raman spectroscopy. Unlike in metallic exsolution, A-site deficiency did not help increase the number of exsolved nanoparticles, but a slight increase in particle size was observed on increasing the reducing temperature under inert conditions ($pO_2 \sim 10^{-5}$ atm), as observed by SEM and SAXS measurements (Fig. 1 a–d and e–f, respectively).

Oxide exsolution beyond metallic paradigms: SAXS insights

The results obtained demonstrate that oxide nanoparticle exsolution is a much more complex phenomenon than metallic exsolution, for which oxide reduction thermodynamics in H_2 provides a reliable initial predictor for the design of exsolved metallic nanocatalysts. In contrast, oxide-nanoparticle exsolution in double perovskites can occur at much higher pO_2 levels and may result in the exsolution of perovskites, spinels, or amorphous carbonate phases. Several of these phases may contain multiple cations present in the pristine double perovskite. More mechanistic studies are required to define oxide exsolution guidelines that could result in functionalised electrodes with higher electrocatalytic activity. This work also provides one of the first demonstrations that SAXS can play a critical role in exsolution investigation, as it enables the analysis of a substantially more representative volume fraction than conventional microscopy techniques.

[1] A. J. Carrillo et al., Evaluating oxide nanoparticle exsolution on A-site deficient $PrBaCo_2O_{6-\delta}$ electrodes, J. Phys. Energy 7, 025007 (2025)

DOI: 10.1088/2515-7655/ada8de

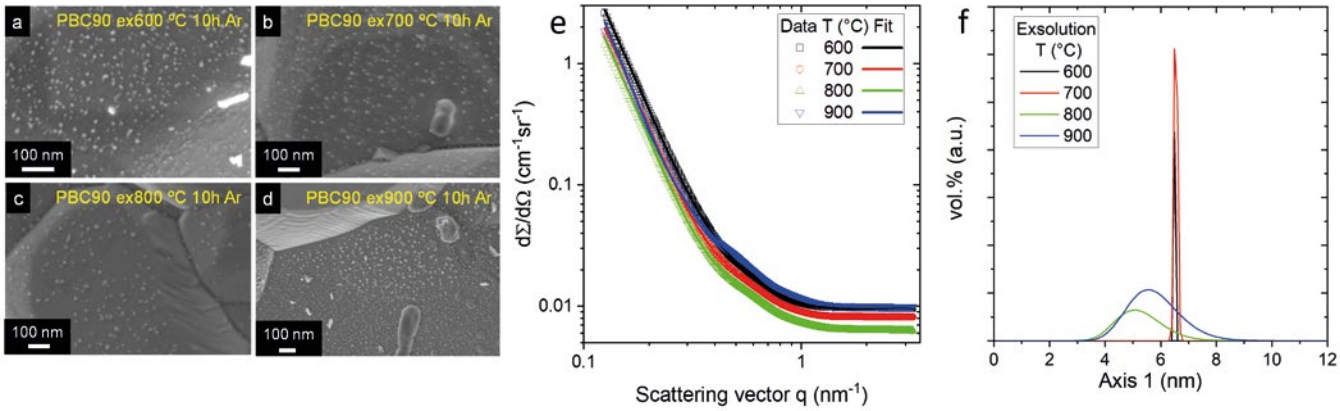

Figure 1: Exsolved nanoparticles of $PrBa_{0.90}Co_2O_{6-\delta}$ (PBC90) obtained at different temperatures, observed by SEM (a–d), with corresponding SAXS curves (e) and the lognormal size distribution of the rotational axis of the ellipsoid used for fitting the exsolved nanoparticles (f).

Impact of coating type on structure and magnetic properties of biocompatible iron oxide nanoparticles

A. Nasser[1,2], A. Qdemat[3], H. Unterweger[4], R. Tietze[4], X. Sun[5], J. Landers[6], J. Kopp[6], B. Wu[2], M.-S. Appavou[2], A. Murmiliuk[2], E. P. Gilbert[7], O. Petracic[3], A. Feoktystov[2]

[1] Department of Physics, Technical University of Munich, Garching, Germany; [2] Jülich Centre for Neutron Science (JCNS) at MLZ, Forschungszentrum Jülich GmbH, Garching, Germany; [3] Jülich Centre for Neutron Science (JCNS-2), Forschungszentrum Jülich GmbH, Jülich, Germany; [4] ENT Department, Section of Experimental Oncology and Nanomedicine (SEON), University Hospital Erlangen, Erlangen, Germany; [5] Deutsches Elektronen-Synchrotron DESY, Hamburg, Germany; [6] Faculty of Physics and Centre for Nanointegration Duisburg-Essen (CENIDE), University of Duisburg-Essen, Duisburg, Germany; [7] Australian Nuclear Science and Technology Organisation (ANSTO), Lucas Heights, Australia

Superparamagnetic iron oxide nanoparticles (SPIONs) are promising for biomedical applications. However, the agglomeration limits the performance. In this work, SPIONs coated with sodium citrate, (3-aminopropyl)triethoxysilane (APTES), and dextran were investigated to control the agglomeration. Structural and magnetic properties were characterised using cryogenic transmission electron microscopy, magnetometry, Mössbauer spectroscopy, and small-angle X-ray (KWS-X instrument at MLZ) and neutron scattering. The coating agents stabilise the nanoparticles, forming clusters of varied sizes and modifying the magnetic behaviour via interparticle interactions. In addition, we studied the oxidation kinetics and find differences in the long-term stability.

Controlled agglomeration of SPIONs has attracted attention because the formation of larger assemblies enhances the magnetic response [1]. While many studies have examined the cluster formation and physicochemical properties, the impact of coating type on magnetic behaviour remains debated.

Magnetic size determination

Magnetic small-angle neutron scattering (QUOKKA instrument at ANSTO) was employed to determine the magnetic size of the citrate-coated samples. At zero applied magnetic field, the scattering intensity contains 2/3 of the magnetic contribution. Dispersing the nanoparticles in D_2O allows the nuclear contrast to be suppressed, enabling the separation of the magnetic scattering contribution from the nuclear scattering. Thus, the magnetic size of the clusters at ambient conditions constituted approximately 17 nm.

Fig. 1a shows the scattering intensity of the citrate-coated nanoparticles in D_2O extracted from detector sectors parallel ($H \parallel Q$) and perpendicular ($H \perp Q$) to the applied field. Upon application of a saturating magnetic field, a pronounced anisotropy developed due to field-dependent magnetic scattering distribution. Pure magnetic scattering was separated at large fields close to saturation by subtracting the parallel-sector intensity (nuclear contribution) from the perpendicular-sector intensity (nuclear + magnetic contribution), as shown in Fig. 1b. At large fields, magnetic scattering showed a Guinier regime with size approximately 35 nm, smaller than the structural cluster (~56 nm), indicating a multi-domain structure even under saturation conditions.

Overall, SAXS results indicate that the type of coating influences the organisation of nanoparticles, with citrate and dextran forming compact clusters, and APTES promoting fractal-like assemblies. The differences in oxidation behaviour of nanoparticles with different coatings are related to particle size resulting from the coating agent used and the synthesis route.

[1] A. Nasser et al., Impact of coating type on structure and magnetic properties of biocompatible iron oxide nanoparticles: insights into cluster organisation and oxidation stability, Phys. Chem. Chem. Phys. 26, 24912 (2024)
DOI: 10.1039/d4cp01735h

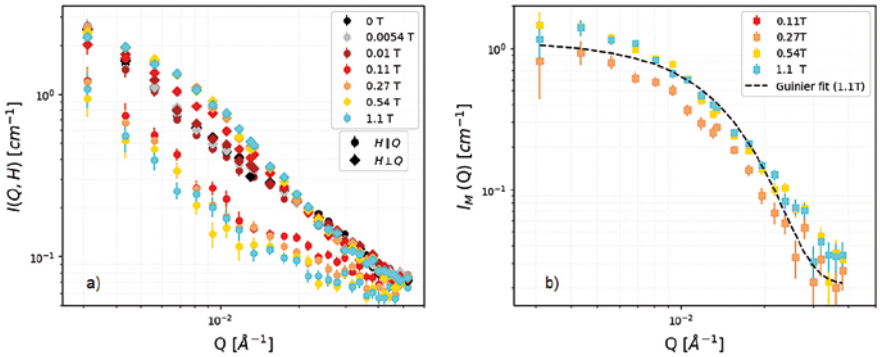

Figure 1: Small-angle neutron scattering of the citrate-coated nanoparticles dispersed in D_2O. (a) Scattering intensity in the sectors parallel ($H \parallel Q$) and perpendicular ($H \perp Q$) to the applied field. (b) Pure magnetic scattering at large magnetic fields close to saturation, used to determine the magnetic size via a Guinier approximation.

Exploring the limits of passive macromolecular translocation through phospholipid membranes

E. Kostyurina[1], R. Biehl[1], M. Kruteva[1], A. Koutsioubas[2], H. Frielinghaus[2], N. R. Yepuri[3], S. Förster[1], J. Allgaier[1]

[1] Jülich Centre for Neutron Science (JCNS-1), Forschungszentrum Jülich GmbH, Jülich, Germany;
[2] Jülich Centre for Neutron Science (JCNS) at MLZ, Forschungszentrum Jülich GmbH, Garching, Germany;
[3] National Deuteration Facility, Australian Nuclear Science and Technology Organisation, Lucas Heights, Australia

The transportation of active macromolecules through cell membranes is an essential biological process. For hydrophilic macromolecules, the hydrophobic interior of lipid bilayers suppresses passive translocation. We use alternating amphiphilic polymers (AAPs) in which the sizes of the hydrophilic and hydrophobic units can be varied over a broad range, keeping the polymers water-soluble. The optimal conditions for translocation of AAPs are determined.

For the transport of molecules across cell membranes, the membrane has a barrier function, where the hydrophobic interior of the lipid bilayer prevents the passive cross-membrane diffusion of polar molecules. Therefore, small molecules of moderate polarity can, for the most part, cross lipid membranes by passive diffusion, whereas macromolecules generally translocate through the membrane via endocytosis and exocytosis pathways or, in the case of highly charged molecules, via pore formation. The translocation of alternating and random polymers was predicted by theory and also observed for a few synthetic amphiphilic polymers. In a previous study, we showed that non-ionic AAPs of intermediate polarity can cross lipid membranes by passive diffusion in the time scale from minutes to hours depending on the AAP length, lipid composition, temperature, and other factors. Thus, AAPs are promising candidates as drug carriers in medical applications.

The strategy

In this work [1], we explored the translocation phenomenon for more hydrophilic AAPs. AAPs with a given lower critical solution temperature can have very different polarity profiles along the chain, which are expected to strongly influence the translocation behaviour. Increasing the size of both the hydrophilic and hydrophobic units leads to the limiting case of long, blocky structures with reduced translocation capability known from block copolymers.

The optimal conditions

Pulse field gradient NMR measurements and neutron reflectivity experiments at MARIA (MLZ) show that AAPs with short units have a high solubility in the membrane hydrophobic interior that allows the chains to passively translocate. Increasing the length of the hydrophilic units leads to more polar AAPs with low membrane solubility and a reduced translocation speed (Fig. 1). If both moieties are increased in size, the AAPs have a strong amphiphilic character and adsorb to lipid membranes only with their hydrophobic units, have a high membrane concentration, and have an overall fast translocation kinetics.

[1] E. Kostyurina et al., Exploring the limits of passive macromolecular translocation through phospholipid membranes, Biomacromolecules 26, 6917 (2025)
DOI: 10.1021/acs.biomac.5c01234

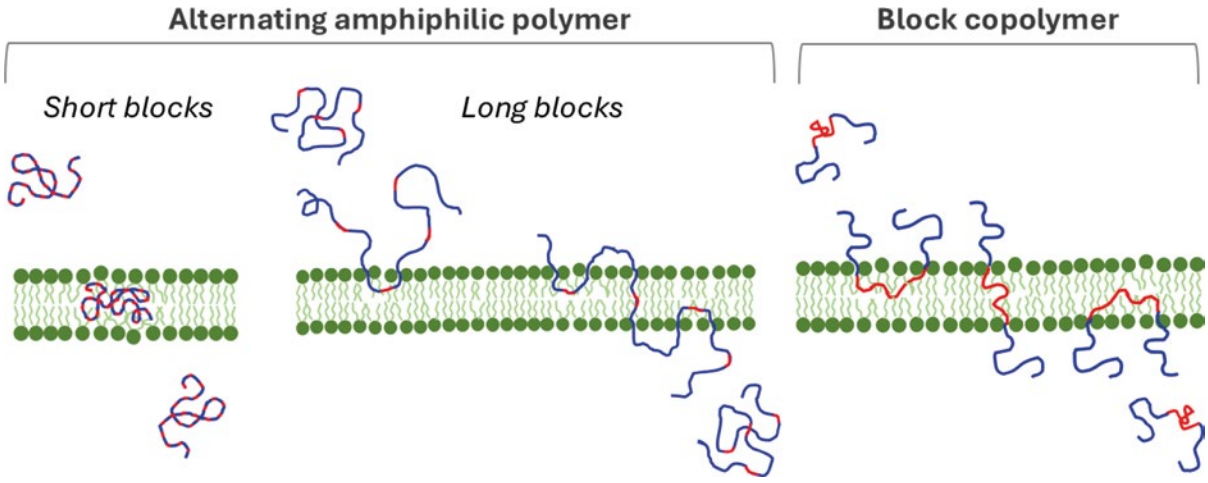

Figure 1: Schematic illustration of translocation mechanisms of AAPs with hydrophobic (red) and hydrophilic (blue) moieties having a more homogeneous polarity profile, amphiphilic AAPs, and the Pluronic triblock (from left to right) as resolved from pulse field gradient NMR and neutron reflectivity measurements with lipid bilayers (green) as model cell membranes. Promising candidates may serve as drug carriers in medical applications.

Structure and chain dynamics of self-healing telechelic polymer networks

R. Lund[1], L. Willner[2], O. Holderer[3]

[1] Department of Chemistry and Hylleraas Centre for Quantum Molecular Sciences, University of Oslo, Oslo, Norway;
[2] Jülich Centre for Neutron Science (JCNS-1), Forschungszentrum Jülich GmbH, Jülich, Germany;
[3] Jülich Centre for Neutron Science (JCNS) at MLZ, Forschungszentrum Jülich GmbH, Garching, Germany

Hydrogel networks with transient bond structure are capable of healing defects induced by rupture and damage. Telechelic polymers, having functional end groups, are able to form such "self-healing" hydrogels, interesting for fundamental research and possible applications alike. SANS at KWS-2 and neutron spin echo measurements at J-NSE in different contrasts revealed the roles of the micellar cores formed by the hydrophobic end groups and the chains spanning the hydrogel.

Self-healing materials have attracted increasing interest over the last years, from a fundamental point of view due to their fascinating molecular properties, and also for potential applications. Polymers with functional chain ends, so-called telechelic polymers, possess the capability of forming networks with transient bonds, which can form and dissociate and therefore have self-healing properties. In this study, the functional hydrophobic end-groups can self-assemble in micelles, acting as cross-linking points, with the polymers connecting different micelles or forming loops around one micellar core, and building in this way a gel-like network (see Fig. 1).

Contrast variation as key

The properties of such gels are determined by their structure and, equally important, by the dynamics, i. e. the thermally driven motion of the polymer chains and the micellar cores of the gel. Contrast variation makes it possible to gain deep insight into different parts of the gel, such as the micellar core structure and dynamics or the chain segmental motion in the gel or in the precursor solution. Fig. 1 highlights two situations, where the polymer chains are invisible, with the same scattering length density (SLD) as the solvent, and only the micellar cores dominate the scattering, and the inverse, where the core SLD is matched with the solvent and only the polymer chains are studied.

NSE shows molecular motion

Neutron spin echo spectroscopy (NSE) permitted tagging the slow diffusive motion of the micellar cores formed by the hydrophobic end groups in one contrast, and the segmental motion of the PEO polymer chains in the other case (Fig. 1, right). The chain dynamics in the gel resembles that of an ideal polymer in solution (Zimm dynamics), even under rather crowded conditions, where in other gels additional interactions have been observed. The micellar cores appear to be responsible for ensuring that the network is well stretched. The fast, relatively unconstrained chain dynamics plays an important role in the "self-healing" capability, while the micellar cores are important in the rheological response.

[1] R. Lund et al., Structure and chain dynamics of self-healing telechelic polymer networks, Macromolecules 58, 9754 (2025)
DOI: 10.1021/acs.macromol.5c01216

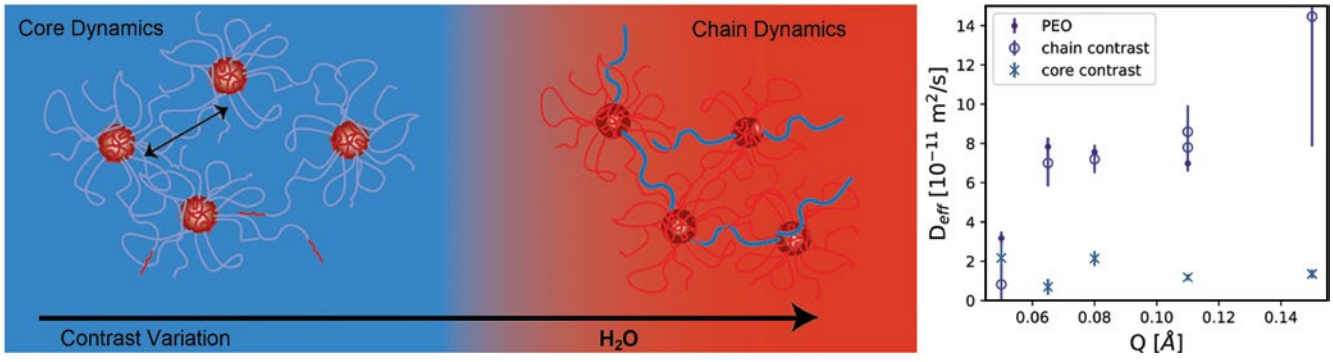

Figure 1: (left) Schematic picture of the hydrogel network with micellar cores built by the hydrophobic chain ends. (right) Depending on the polymer labelling scheme and the solvent scattering length density, neutron scattering makes it possible to discern the diffusive motion of the cores with Zimm like chain dynamics of the polymers spanning the hydrogel (visible in the diffusion coefficients).

Impact of humidity on water dynamics and conductivity in PEDOT:PSS/CNF films

L. P. Kreuzer[1], M. Betker[2], M. Wolf[1], B.-J. Niebuur[3], J. Ollivier[4], L. D. Söderberg[5], S. V. Roth[2,5]

[1] Heinz Maier-Leibnitz Zentrum (MLZ), Technical University of Munich, Garching, Germany; [2] Deutsches Elektronen-Synchrotron DESY, Hamburg, Germany; [3] INM – Leibniz-Institute for New Materials, Saarbrücken, Germany; [4] Institut Laue-Langevin (ILL), Grenoble, France; [5] Department of Fibre and Polymer Technology, KTH Royal Institute of Technology, Stockholm, Sweden

Conductive PEDOT:PSS/cellulose nanofibril films were characterised as a function of humidity using quasi-elastic neutron scattering with respect to applicability as organic electronics across numerous fields, such as batteries, supercapacitors, and solar cells. The integration of PEDOT:PSS into a matrix of organic nanofibers mitigates humidity-induced internal stresses, thereby ensuring structural stability and preserving device performance.

Water dynamics under changing humidity

Quasi-elastic neutron scattering at IN5 (ILL) was employed to probe the motion of water in PEDOT:PSS/cellulose nanofibril nanocomposite films during three consecutive cycles of low and high relative humidity. Two distinct water populations were identified inside the films: fast-moving bulk water and slow-moving hydration water bound to the polymer matrix. In humid environments, both species coexist, while bulk water is fully released under dry conditions. Hydration water remains present even at low humidity and exhibits significantly slowed, localised dynamics, reflecting strong interactions with, in particular, hydrophilic groups of PEDOT:PSS.

Coupling structure, dynamics and conductivity

The first humidity cycle induces irreversible structural rearrangements caused by a kinetically trapped morphology formed during rapid spray-deposition on a heated Si substrate. A high fraction of hydration water enhances polymer chain mobility, enabling PEDOT:PSS to de-wet from cellulose nanofibrils and form larger clusters, which leads to reduced electrical conductivity. Upon drying, bulk water and part of the hydration water are released, promoting re-wetting of the nanofibrils and recovery of conductivity. Subsequent humidity cycles show reproducible and reversible behaviour, with stable water populations and reversible nano-structural changes (Fig. 1) directly reflected in the electrical response.

Implications for organic electronics

By explicitly linking nanostructure, water dynamics and electrical performance, this study provides a microscopic understanding of humidity effects in conductive biopolymer composites. The quantitative description of hydration water diffusion, including residence times and jump lengths, offers valuable input for molecular simulations and materials design. These insights support the development of mechanically stable, humidity-tolerant organic electronic materials based on sustainable nanocellulose-polymer architectures.

[1] L. P. Kreuzer et al., Impact of humidity on water dynamics and electrical conductivity in PEDOT:PSS/cellulose nanofibril nanocomposite films: Insights from quasi-elastic neutron scattering, Macromolecules 58, 2247 (2025)
DOI: 10.1021/acs.macromol.4c02412

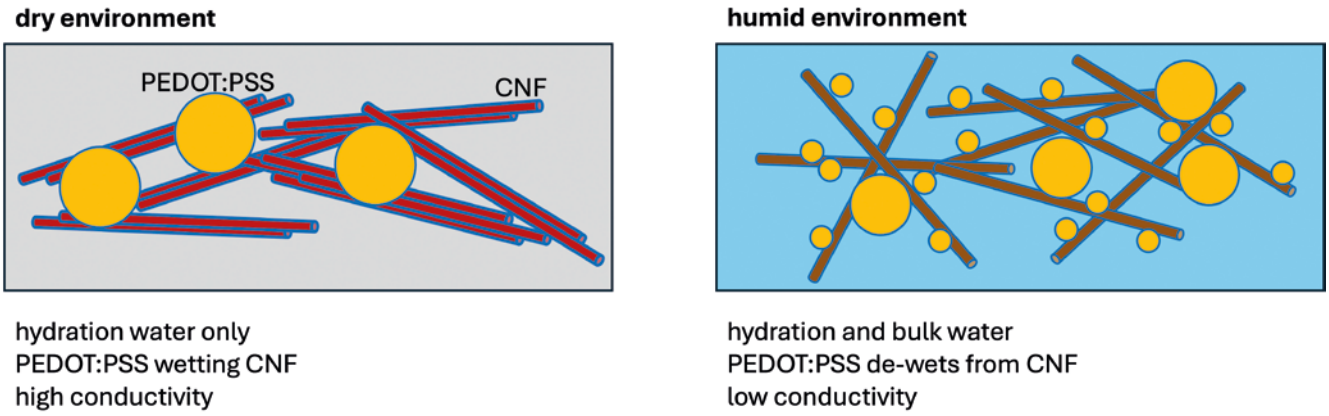

Figure 1: Schematic illustration of humidity-dependent water dynamics and nano-structural rearrangements in PEDOT:PSS/cellulose nanofibril films. Quasi-elastic neutron scattering reveals two water species: fast bulk water and slow hydration water. Bulk water is released upon drying, while hydration water remains, controls polymer mobility, and governs reversible changes in wetting and electrical conductivity.

Proteins derived from green biomass: Alfalfa and water lentil concentrate for emulsions

M. Müller[1], O. Holderer[1], K. Schwärzer[2], A. Wiese-Klingenberg[3], B. Förster[4], S. Förster[1,2], J. Kohlbrecher[5], K. Wood[6], B. Wu[1], S. Hauschild[2], H. Frielinghaus[1], T. Heiden-Hecht[1]

[1] Jülich Centre for Neutron Science (JCNS) at MLZ, Forschungszentrum Jülich GmbH, Garching, Germany; [2] Jülich Centre for Neutron Science (JCNS-1), Forschungszentrum Jülich GmbH, Jülich, Germany; [3] Institute of Bio- and Geoscience (IBG-4: Bioinformatics), Bioeconomy Science Centre (BioSC), Forschungszentrum Jülich GmbH, Jülich, Germany; [4] Ernst Ruska-Centre for Microscopy and Spectroscopy with Electrons, Physics of Nanoscale Systems (ER-C-1), Forschungszentrum Jülich GmbH, Jülich, Germany; [5] Paul Scherrer Institut (PSI), Villigen, Switzerland; [6] Australian Centre for Neutron Scattering (ANSTO), Lucas Heights, Australia

Alfalfa and water lentil concentrates, known for their high protein content, have been investigated for their potential in stabilising emulsions for food applications. With their main protein component RuBisCo, the concentrates are able to stabilise oil-water interfaces in emulsions and may therefore be used for plant-based “milk”. SAXS and SANS experiments contribute to the characterisation of the complex stabilisation mechanism and the structure at the interface.

The sustainability of food products is an increasingly important issue, and plant-based proteins can help in tackling this challenge. Protein sources that have received little attention in nutrition to date are particularly interesting in this context. Green biomass from alfalfa and water lentils have been investigated in this context, with the aim of stabilising plant-based emulsions as a replacement for animal-based milk. A variety of techniques have been used to approach the interfacial details, including cryo-TEM, proteomics or confocal laser scanning microscopy. Fig. 1 illustrates the materials and ideas featured in this investigation.

The flavours of small-angle scattering

The complex multicomponent system of an emulsion is very difficult to study on molecular length scales, and a combination of different techniques is key to understanding the details of what goes on at the border between oil and water. With the availability of X-rays (SAXS) and neutrons (SANS) and, in the case of the latter, the possibility of varying the contrast in the emulsion by exchanging oil and water with their deuterated counterparts, structural details of the stabilisation process were able to be obtained.

Food for thought

The RuBisCo rich protein isolates were capable of forming oil-in-water emulsions. Structural rearrangements at the oil-water interface could be observed with SANS (SANS-1, PSI and Quokka, ANSTO) and SAXS (KWS-X, MLZ) and were more prominent for concentrates from alfalfa as compared to the water lentil source. The combination with phenolic compounds resulted in aggregates, which increased the complexity of the system and requires further studies for an even deeper understanding of the stabilisation process of these isolates.

[1] M. Müller et al., Proteins derived from green biomass: Alfalfa (Medicago sativa L.) and water lentil concentrate (Lemna minor L.) in the focus as stabilisers for emulsions, Food Hydrocolloids Health 8, 100233 (2025)
DOI: 10.1016/j.fhfh.2025.100233

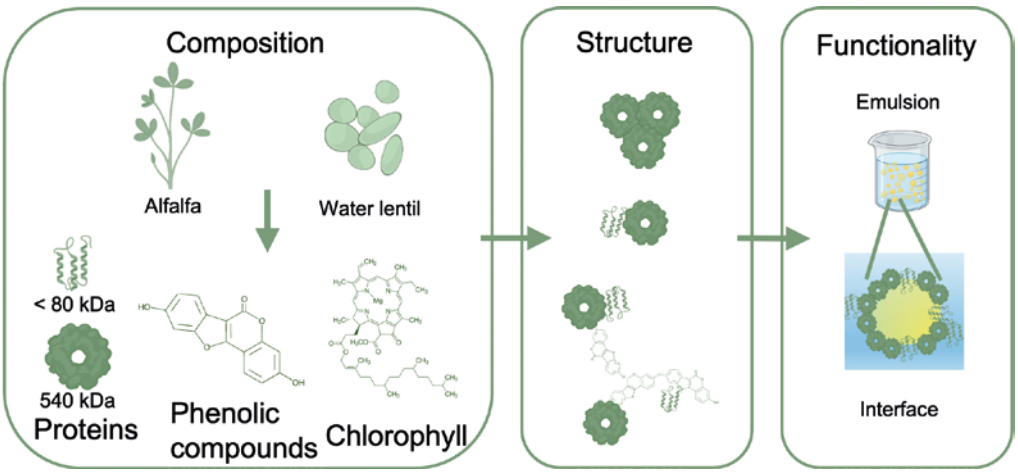

Figure 1: Concentrates from alfalfa and water lentil contain RuBisCo as a main protein fraction, but also many other components, which are involved in forming protein aggregates in solution, and also play a role in their capacity to form oil-in-water emulsions. Solution and emulsion structures are investigated with SAXS and SANS under different contrast conditions.

Neutron structural study of the proton transfer pathway in NADH-cytochrome b_5 reductase

Y. Hirano[1,2,3], K. Kurihara[4], K. Kusaka[5], A. Ostermann[6], M. Hikita[7], S. Kimura[8], K. Miki[9], T. Tamada[1,3]

[1] Institute for Quantum Life Science, National Institutes for Quantum Science and Technology, Chiba, Japan; [2] PRESTO, The Japan Science and Technology Agency, Saitama, Japan; [3] Center of Quantum Life Science for Structural Therapeutics, Chiba University, Chiba, Japan; [4] Institute for Quantum Life Science, National Institutes for Quantum Science and Technology, Ibaraki, Japan; [5] Neutron Industrial Application Promotion Centre, Comprehensive Research Organisation for Science and Society, Ibaraki, Japan; [6] Heinz Maier-Leibnitz Zentrum (MLZ), Technical University of Munich, Garching, Germany; [7] Structural Biology Research Centre, High Energy Research Organisation, Ibaraki, Japan; [8] Graduate School of Science and Engineering, Ibaraki University, Ibaraki, Japan; [9] Graduate School of Science, Kyoto University, Kyoto, Japan

NADH-cytochrome b_5 reductase (b5R) has the redox reaction cycle with electron, proton (H^+), and hydride (H^-) transfer steps via FAD and NADH cofactors. Due to a lack of information about hydrogen atoms directly involved in the redox reaction, the precise molecular mechanism for the H^+ transfer step remains unclear. The neutron structures determined at different pD-values reveal the structural basis for the proton transfer catalysed by b5R.

Neutron crystal structures at different pD-values

His49, located near FAD, is conserved in the mammalian NADH-cytochrome b_5 reductase (b5R) family, and its mutation influences the electron transfer rate. We determined the neutron crystal structures of the oxidised form of b5R for two pD conditions around the pKa of histidine [1]. Large crystals for neutron diffraction data collection were prepared for two pD conditions (6.5 and 7.5). The diffraction data sets were collected using the iBIX diffractometer of J-PARC (pD 6.5) and the BIODIFF diffractometer at MLZ (pD 7.5). The hydrogen bonds around FAD bound to the oxidised form of b5R were confirmed by observing the hydrogen atoms of water molecules and of amino acid residues. The orientations of water molecules that form hydrogen bonds with the FAD isoalloxazine ring are conserved in both structures. The hydrogen-bonding environment highlights its role in defining the position of the isoalloxazine ring during the redox reaction. The amide hydrogen of Thr66 forms the hydrogen bond with the N5 of the FAD isoalloxazine ring. This amide hydrogen was observed as hydrogen in both structures (H_N in Fig. 1), although the crystals were incubated in the deuterated solutions. This result indicates that a protected stable hydrogen-bond formed between Thr66 and FAD is important for stabilising the oxidised state. On the other hand, we found a structural difference between the structures at the two pD conditions in the hydrogen-bond between His49 and Tyr51. His49 is a charged state at pD 6.5 and a neutral state at pD 7.5 (see Fig. 1). Thus, the hydrogen-bond network extends from FAD to Tyr51 at pD 6.5, while the corresponding network is broken between His49 and Tyr51 at pD 7.5. The stopped-flow spectroscopy measurements showed that the turnover reaction rates for the b5R redox cycle below pH 6.5 were faster than those above pH 6.8. These structural and spectroscopic results indicate that the continuous hydrogen-bond network from FAD to the protein surface (Tyr51) is involved in the proton transfer pathway in b5R.

[1] Y. Hirano et al., Structural basis of hydride and proton transfer reactions revealed by the detection of hydrogen atoms in mammalian NADH-cytochrome b5 reductase, Structure 34(1), 76 (2026)
DOI: 10.1016/j.str.2025.10.006

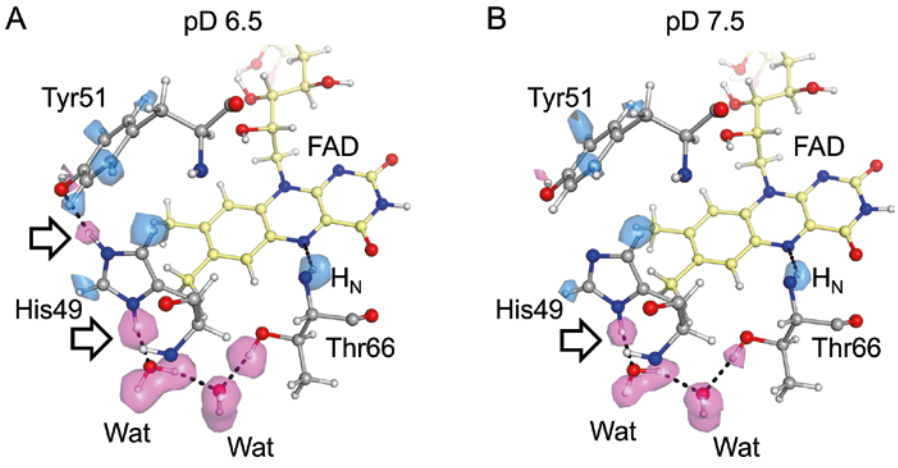

Figure 1: Hydrogen-bond network from FAD to the protein surface in two pD conditions. (A) The hydrogen bonds at pD 6.5. (B) The hydrogen bonds at pD 7.5. Deuterated states of His49 are indicated by arrows. The Thr66 H_N positions are indicated in the figures. mF_o-DF_c H omit map (-3.5σ level) is shown as a blue surface and D omit map (+4.0σ level) is shown as a pink surface. Hydrogen bonds are indicated as dotted lines.

Structure stabilisation by inductive effect on TM-O-B bonds of NCM811 cathode materials

B. Ying[1], Z. Teng[1], A. Senyshyn[2], M. Avdeev[3,4], A. Jonas[5], J. Peng[6], S. Simonsen[7], S. Indris[6], O. Dolotko[6], R. Schmuch[8], P. Yan[9], M. Merz[10,11], P. Nagel[10,11], S. Schuppler[10,11], H. Ehrenberg[6], M. Winter[1,9], K. Kleiner[1]

[1] MEET, Battery Research Centre, University of Muenster, Muenster, Germany; [2] Heinz Maier-Leibnitz Centre (MLZ), Technical University of Munich, Garching, Germany; [3] Australian Centre for Neutron Scattering, ANSTO, Lucas Heights, Australia; [4] School of Chemistry, The University of Sydney, Sydney, Australia; [5] Physikalisch-Technische Bundesanstalt (PTB), Berlin, Germany; [6] Institute for Applied Materials, Karlsruhe Institute of Technology, Eggenstein-Leopoldshafen, Germany; [7] Department of Energy Conversion and Storage, DTU Energy, Technical University of Denmark, Kongens Lyngby, Denmark; [8] Fraunhofer Research Institution for Battery Cell Production FFB, University Muenster, Münster, Germany; [9] Helmholtz-Institute Muenster, IEK-12, Research Institute in Jülich, Muenster, Germany; [10] Institute for Quantum Materials and Technologies, Karlsruhe Institute of Technology, Karlsruhe, Germany; [11] Karlsruhe Nano Micro Facility, Karlsruhe Institute of Technology, Eggenstein-Leopoldshafen, Germany

Boron doping has emerged as an effective strategy for enhancing the electrochemical properties of nickel-rich lithium layered oxides, such as NCM811. Despite the industrial use of boron-coated NCMs, the underlying mechanism in these materials remains insufficiently understood. In this study, boron was homogeneously incorporated into the tetrahedral site of NCM811, exerting an inductive effect on transition-metal (*TM*)-O-B bonds that delayed structural collapse and reduced oxygen release, thereby enhancing cycling performance.

B occupation of tetrahedral sites

NCM811_xB ($LiNi_{0.8}Co_{0.1}Mn_{0.1}O_2$, x = 0, 0.5, 1, 2, 5 at.%) materials with different boron contents were synthesised via the conventional co-precipitation method. To identify the boron incorporation site, neutron diffraction performed at ECHIDNA, ANSTO was conducted on NCM811_5B and NCM811 with ^{11}B used to enhance the signal. Structural refinements were carried out, considering possible boron occupation at 3a (*TM*), 3b (Li), 6c (O), and tetrahedral sites. Substitution of Li^+, TM^{n+}, or O^{2-} by B^{3+} slightly improved the refinement compared to the boron-free model; however, a significantly better fit was obtained when boron was placed in the tetrahedral sites. As shown in Fig. 1a, b, the inclusion of tetrahedral boron noticeably reduces the mismatch between experiment and model, indicating that boron does not substitute specific lattice atoms but, instead, occupies tetrahedral interstitial sites.

Inductive effect

To investigate the stabilisation mechanism, near-edge X-ray absorption fine structure (NEXAFS) measurements in fluorescence yield mode were performed for NCM811, NCM811_2B, and NCM811_5B at the WERA beamline of the Karlsruhe synchrotron light source KARA and the PGM beamline of BESSY II. As shown in Fig. 1c, increasing boron content leads to reduced Ni-O hybridisation, reflected by changes in the O_1 (~529 eV) and O_2 (~530 eV) features corresponding to Ni t_{2g}/e_g-O 2p hybridisation, suggesting a weakening of the Ni and O bonds. Ni L-edge spectra (Fig. 1d) further reveal a decrease in Ni^{3+} (N_2) accompanied by an increase in Ni^{2+} (N_1), supporting the formation of more localised electronic states with an increase in the B content. As illustrated in Fig. 1e, tetrahedrally incorporated boron has an inductive effect on *TM*-O-B bonds due to its higher electronegativity relative to *TM*s, increasing the ionic character of *TM*-O bonds, reducing bonding-antibonding orbital separation, and shifting the reaction peak to higher voltages.

[1] B. Ying et al., Insights into homogeneous bulk boron doping at the tetrahedral site of NCM811 cathode materials: structure stabilisation by inductive effect on TM-O-B bonds, Small 21, 2409743 (2025)
DOI: 10.1002/smll.202409743

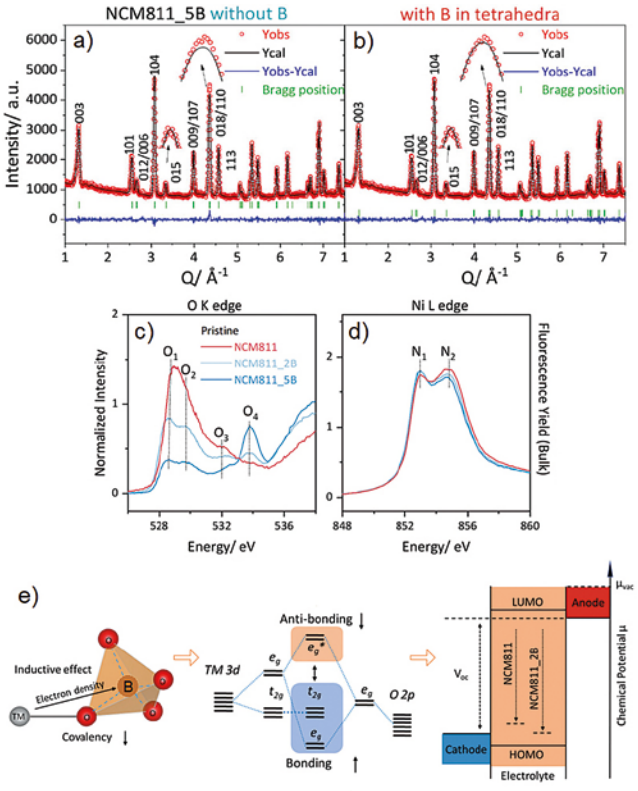

Figure 1: Rietveld refinement of neutron diffraction data for NCM811_5B: (a) without B, (b) with B at the tetrahedral site. NEXAFS spectra of pristine NCM811_xB (x = 0, 2, 5 at.%): (c) O K-edge and (d) Ni L-edge. (e) Inductive effect lowers *TM*-O bonding energy, reducing covalency and chemical potential μ.

Understanding the thermal decomposition of commercial nickel-cobalt-aluminium oxide cathodes

T. Hölderle [1,2], V. Baran [3], A. Schökel [3], L. Westphal [1,2], R. U. Stelzer [4], R. Niewa [4], P. Müller-Buschbaum [2], A. Senyshyn [1]

[1] Heinz Maier-Leibnitz Zentrum (MLZ), Technical University of Munich, Garching, Germany; [2] Department of Physics, TUM School of Natural Science, Technical University of Munich, Garching, Germany; [3] Deutsches Elektronen-Synchrotron DESY, Hamburg, Germany; [4] Institute of Inorganic Chemistry, University of Stuttgart, Stuttgart, Germany

The development of next-generation high-energy batteries with improved performance and safety is directly related to the structural performance of commercial nickel-cobalt-aluminium oxide (NCA) cathodes. In this contribution, synchrotron-based techniques revealed the dependency of temperature and state-of-charge (SOC) on the structural stability of NCA electrodes, highlighting the trade-off between energy density and thermal safety.

New insights in the phase evolution of NCA

The thermal structural stability of commercial NCA cathodes at different SOC was investigated using synchrotron-based powder X-ray diffraction at the beamline P02.1 (PETRA III, DESY). At room temperature, all samples show a layered α-$NaCrS_2$-type rhombohedral structure, characterised by SOC-dependent positions of the (003)L and (104)L reflections (Fig. 1). Upon heating, these reflections initially shift due to thermal expansion and subsequently disappear as intermediate spinel phases emerge. The type of spinel formed depends on the lithium content. LiM_2O_4-type spinels dominate at low SOC, while M_3O_4-type spinels preferentially form at high SOC. Further heating leads to the transformation into a rock-salt-type structure, which occurs at higher temperatures for low-SOC samples. Complementary low-temperature XRD confirms structural stability independent of SOC, indicating that degradation processes are thermally activated.

Thermal decomposition pathways and mass-loss mechanisms

Thermogravimetric analysis reveals that the lithium concentration has a strong influence on thermal decomposition. Fully lithiated NCA (SOC = 0 %) shows a single continuous mass-loss step, whereas partially delithiated samples (SOC > 20 %) exhibit a two-step mass loss. The first step (2 – 3 %) corresponds to the release of oxygen during the layered-to-spinel transition. The second, larger mass loss is associated with the reduction of Ni^{4+} and Co^{4+} and the collapse of the oxygen framework, resulting in the formation of the rock-salt phase and is consistent with the observed phase transitions in Fig. 1. Total mass loss increases linearly with decreasing lithium content, indicating reduced thermal stability at high SOC due to highly oxidised transition metal cations and increased oxygen vacancy formation. These findings underscore the crucial role of delithiation in determining NCA thermal stability and are important for enhancing the safety of NCA-based cathodes.

[1] T. Hölderle et al., Understanding the temperature-induced decomposition of commercial nickel-cobalt-aluminium oxide ($LiNi_{0.8}Co_{0.15}Al_{0.05}O_2$) electrodes, Batteries Supercaps 8, e202500421 (2025)

DOI: 10.1002/batt.202500421

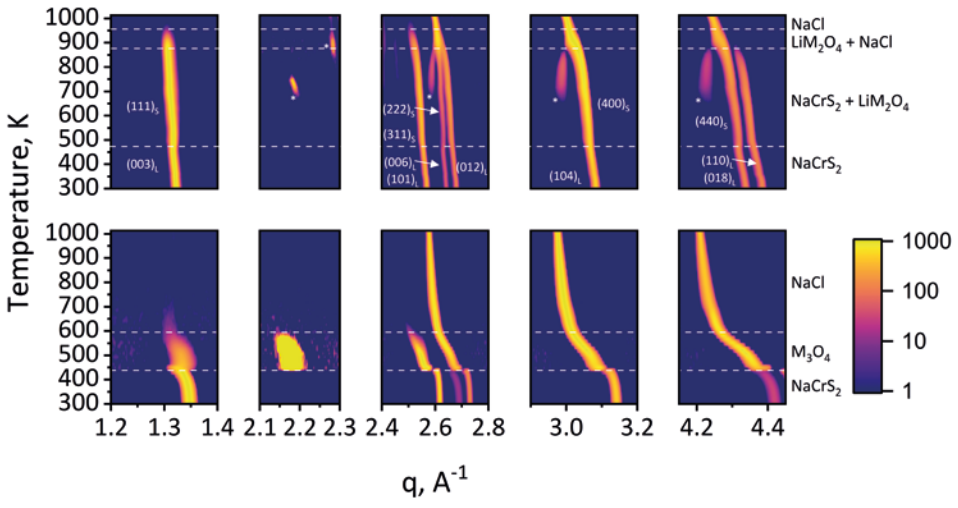

Figure 1: High-temperature diffraction signatures of structural evolution during heating of selected NCA samples at SOC 0 % (upper row) and SOC 100 % (lower row). Asterisks mark superstructural reflections and dashed lines mark phase transitions.

Performance and ageing behaviour of multi-tab 26650-type LFP lithium-ion batteries

D. Petz [1,2], M. J. Mühlbauer [1,3], V. Baran [1,4], J. Rebelo Kornmeier [1], A. Schökel [4], T. Pirling [5], P. Müller-Buschbaum [2], A. Senyshyn [1]

[1] Heinz Maier-Leibnitz Zentrum (MLZ), Technical University of Munich, Garching, Germany; [2] Department of Physics, TUM School of Natural Sciences, Technical University of Munich, Garching, Germany; [3] Institute for Applied Materials (IAM), Karlsruhe Institute of Technology (KIT), Karlsruhe, Germany; [4] Deutsches Elektronen-Synchrotron DESY, Hamburg, Germany; [5] Institut Laue-Langevin (ILL), Grenoble, France

The cycling data and heterogeneous lithium distribution of 26650-type LFP lithium-ion batteries were linked to accelerated ageing. The results show that external geometry does not reflect internal changes, stressing the need for spatially resolved diagnostics and highlighting how connection design, lithium uniformity, and mechanical integrity influence lifetime in both current and next-generation cylindrical Li-ion cells.

Spatially resolved lithiation of electrode material

The local lithium content in the anode and cathode (x in Li_xC_6 and y in Li_yFePO_4) was determined non-destructively by XRD-CT at beamline P02.1 of PETRA III (DESY). Measurements were performed on fresh, fully charged cells, probing the in-plane lithium distribution at mid-height. Lithium concentrations are presented as false-colour maps for anodes and cathodes in Fig. 1.

Both cells exhibit similar average anode lithiation, with plane-averaged x values of 0.919 for cell 1 and 0.922 for cell 2. Despite their similar lithiation grade, their spatial lithium distributions differ remarkably. Cell 1 exhibits a largely uniform in-plane anode lithiation, consistent with literature reports, whereas cell 2 displays pronounced heterogeneities correlated with the current tab positions. Ring-shaped regions of reduced lithiation were observed near the tabs, centre pin, and housing.

The average in-plane lithium content of the cathode was y = 0.100 for cell 1 and y = 0.043 for cell 2. Both lithium distributions in the anode and cathode are complementary: regions of lower anode lithiation correspond to higher cathode lithium content. In cell 1, the cathode shows a weak gradient from the cell centre towards the housing, while in cell 2, higher cathode lithiation coincides with anode tab locations. Compared to single-tab 18650-type cells, the multi-tab design of cell 1 effectively reduces edge-related inhomogeneities.

Determining lithiation hotspots in the battery jelly roll

An activity parameter A = x – y was introduced to quantify local electrode usage. Mean A values of 0.819 for cell 1 and 0.879 for cell 2 indicate higher local stress in cell 2. Spatial analysis reveals a homogeneous activity distribution in cell 1, whereas cell 2 shows reduced activity at current tab locations and higher stress elsewhere, suggesting accelerated degradation despite its initially higher capacity. The XRD-CT spatial resolution (1 × 1 mm²) does not resolve individual electrode layers or microscopic effects but is sufficient to capture macroscopic lithium gradients relevant to cell ageing.

[1] D. Petz et al., Influence of current tabs on performance and ageing of multi-tab 26650-type LFP lithium-ion batteries, J. Energy Storage 115, 115911 (2025)
DOI: 10.1016/j.est.2025.115911

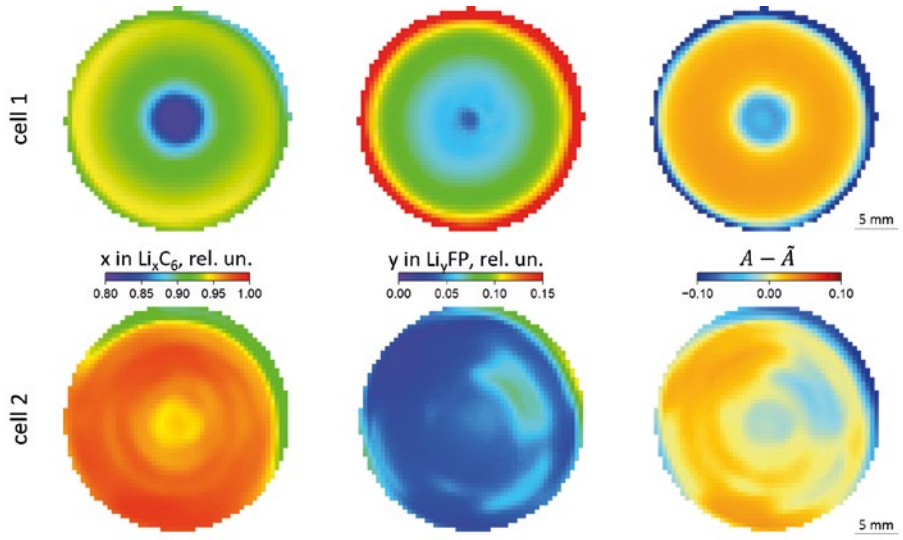

Figure 1: Spatial distributions of lithium content, Li_xC_6 in the graphite anode (left) and Li_yFePO_4 in the LFP cathode (centre), are shown for cell 1 (top) and cell 2 (bottom). The right panel presents the corresponding in-plane distribution of electrode utilisation ($A - \tilde{A}$).

Temperature-resolved crystal structure of ethylene carbonate

L. Westphal[1,2], V. Kochetov[2], V. Baran[3], T. Hölderle[1,2], M. Avdeev[4,5], V. Diadkin[6], K. Marshall[6], A. Schökel[3], K. Opri[7], R. Niewa[7], F. Porcher[8,9], P. Müller-Buschbaum[1], A. Senyshyn[2]

[1]Department of Physics, TUM School of Natural Sciences, Technical University of Munich, Garching, Germany; [2]Heinz Maier-Leibnitz Zentrum (MLZ), Technical University of Munich, Garching, Germany; [3]Deutsches Elektronen-Synchrotron DESY, Hamburg, Germany; [4]Australian Centre for Neutron Scattering, Australian Nuclear Science and Technology Organisation (ANSTO), Lucas Heights, Australia; [5]School of Chemistry, University of Sydney, Sydney, Australia; [6]Swiss-Norwegian Beamlines, ESRF-The European Synchrotron, Grenoble, France; [7]Institute of Inorganic Chemistry, University of Stuttgart, Stuttgart, Germany; [8]Laboratoire Léon Brillouin, CEA-CNRS UMR 12, Gif-sur-Yvette, France; [9]European Spallation Source ERIC, Lund, Sweden

Ethylene carbonate (EC) is an organic solvent of the class of carbonate esters, used in state-of-the-art Li-ion batteries as part of the charge-mediating electrolyte mixture. This contribution presents temperature-dependent neutron and synchrotron powder diffraction data to study the unit cell volume of EC from 3 K up to its melting point, along with synchrotron total scattering and pair distribution function analysis in the liquid state.

The liquid electrolyte is an important component of the battery, responsible for ion transfer during the (dis-)charge process. Almost all commercially available Li-ion batteries contain ethylene carbonate (EC), which plays a crucial role in forming the solid electrolyte interface and protecting the anode surface from continuous electrolyte reduction.

Combining neutron and synchrotron powder diffraction

At low temperatures, EC molecules arrange in a monoclinic crystal lattice. The unit cell model is displayed in Fig. 1a. In order to study the unit cell from 3 K up to the melting point at 309 K, we combined neutron and synchrotron powder diffraction data at SPODI (FRM II), Echidna (ANSTO) and P02.1 (PETRA III, DESY) The combined data refinements reveal the temperature-dependent evolution of the cell parameters *a*, *b* and *c*, the monoclinic angle *β* and the corresponding unit cell volume, as presented in Fig. 1b. Over the whole temperature range, EC retains the space group *C*2/*c*, while showing a strong thermal expansion. This thermal expansion can be described by the Mie-Grüneisen equation of state. The equation contains two Debye terms that account for separate contributions from the molecules and the whole lattice to the crystal's internal energy. The fit is shown in Fig. 1b. Calculations of the volumetric thermal expansion coefficient also support the presence of two Debye temperatures.

What happens above the melting point?

Total scattering experiments on EC were performed at P02.1 and BM31 (ESRF) to calculate the pair distribution function (PDF) and to compare the short-range order of the molecule at room temperature with the long-range order determined by powder diffraction, as well as to analyse the short-range order in its liquid state. At room temperature, the short- and long-range orders are well in line. After heating the sample above its melting point, the PDF unambiguously shows that all long-range order vanishes, as expected, while the short-range order, which is everything up to the largest intramolecular distance, remains intact.

[1] L. Westphal et al., Temperature-resolved crystal structure of ethylene carbonate, J. Phys. Chem. C 129, 11546 (2025) DOI: 10.1021/acs.jpcc.4c08421

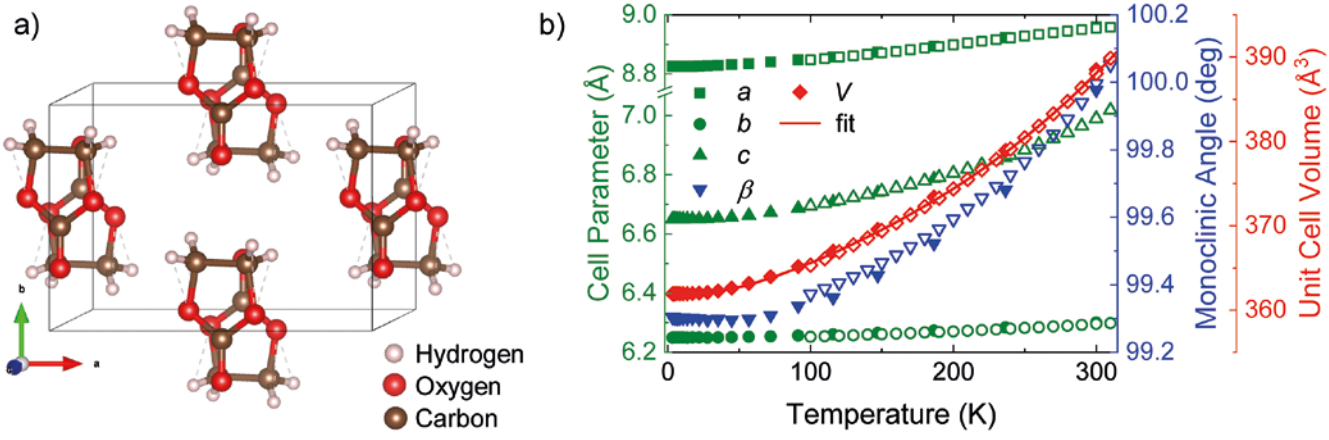

Figure 1: a) Unit cell model of ethylene carbonate at room temperature, obtained from neutron and synchrotron powder diffraction. b) Temperature evolution of the cell parameters *a*, *b*, and *c*, the monoclinic angle *β*, and the resulting unit cell volume *V* from neutron (3 – 300 K, solid symbols) and synchrotron (100–310 K, open symbols) diffraction data. The red line shows the fit of the volume data according to the Mie-Grüneisen equation of state.

Structure-electrochemistry relationship in P2-type Na_xMO_2 cathode materials for Na-ion batteries

L. F. Pfeiffer[1], M. Dillenz[2], N. Burgard[1], P. Beran[3,4], D. Roscher[5,6], M. Zarrabeitia[5,6], P. Drews[1], C. Hervoches[3], D. Mikhailova[7], A. Omar[7], V. Baran[8], N. Paul[9], M. Sotoudeh[2], M. Busch[10,11], M. Wohlfahrt-Mehrens[1], A. Groß[2], S. Passerini[6], P. Axmann[1]

[1] ZSW Centre for Solar Energy and Hydrogen Research Baden-Württemberg, Ulm, Germany; [2] Institute of Theoretical Chemistry, Ulm University, Ulm, Germany; [3] Nuclear Physics Institute, CAS, Rez, Czech Republic; [4] European Spallation Source, ERIC, Lund, Sweden; [5] Helmholtz Institute Ulm, Ulm, Germany; [6] Karlsruhe Institute of Technology (KIT), Karlsruhe, Germany; [7] Leibniz Institute for Solid State and Materials Research Dresden (IFW), Dresden, Germany; [8] Deutsches Elektronen-Synchrotron (DESY), Hamburg, Germany; [9] Heinz Maier-Leibnitz Zentrum (MLZ), Technical University of Munich, Garching, Germany; [10] Division of Materials Science, Department of Engineering Sciences and Mathematics, Luleå University of Technology, Luleå, Sweden; [11] Wallenberg Initiative Materials Science for Sustainability (WISE), Luleå University of Technology, Luleå, Sweden

In this collaborative work, we identify charge ordering arising from transition metal superstructure ordering as one of the main contributors to Na^+/vacancy ordering phenomena in P2-type Na_xMO_2 cathode materials for sodium-ion batteries. Based on our analysis, a guideline for the design of cathode compositions with disrupted Na^+/vacancy orderings and enhanced cycle life is postulated.

Sodium-ion batteries (SIBs) are currently developed as a cost-effective and sustainable complementary battery technology to today's ubiquitous lithium-ion batteries. On the cathode side of SIBs, layered P2-type sodium transition metal oxides are promising candidates for the next generation SIBs. However, their performance is often limited by Na^+/vacancy orderings. In this work, we systematically investigate how the transition metal superstructure affects Na^+/vacancy orderings and, consequently, electrochemical behaviour.

Structural analysis

The crystal structure of two representative compositions, P2-$Na_xNi_{1/3}Mn_{2/3}O_2$ and P2-$Na_xMn_{3/4}Ni_{1/4}O_2$, were analysed using a joint refinement of X-ray and neutron diffraction. P2-$Na_xNi_{1/3}Mn_{2/3}O_2$ exhibits a well-defined honeycomb Ni/Mn superstructure in the transition metal layers (see Fig. 1). In the case of P2-$Na_xMn_{3/4}Ni_{1/4}O_2$, this superstructure is partially disrupted by the additional Mn sitting on Ni sites.

Electrochemical performance

Using a combination of electrochemical characterisation, operando XRD, and DFT calculations, we connect these structural insights with the electrochemical response: In P2-$Na_xNi_{1/3}Mn_{2/3}O_2$, the Ni/Mn superstructure leads to transition metal charge orderings, which stabilise specific Na^+/vacancy arrangements at distinct sodium concentrations. This results in pronounced voltage steps during battery operation, associated with phase transitions driven by sodium ordering. In contrast, the partially disrupted transition metal superstructure in P2-$Na_xMn_{3/4}Ni_{1/4}O_2$, results in weakened charge orderings in the transition metal layer, disrupted Na^+/vacancy orderings and consequently a smoother electrochemical voltage profile.

Thus, the origin of Na^+/vacancy orderings in P2-type $Na_xNi_yMn_{1-y}O_2$ is investigated, crosschecking the findings over various transition metal compositions. A general guideline to suppress Na^+/vacancy orderings in P2-type Na_xMO_2 cathode active materials is postulated. Diffraction measurements were done at MEREDIT, Rez, and P02.1, DESY.

[1] L. F. Pfeiffer et al., From structure to electrochemistry: the influence of transition metal ordering on Na^+/vacancy orderings in P2-type Na_xMO_2 cathode materials for sodium-ion batteries, J. Mater. Chem. A 13, 540 (2025)
DOI: 10.1039/D4TA04786A

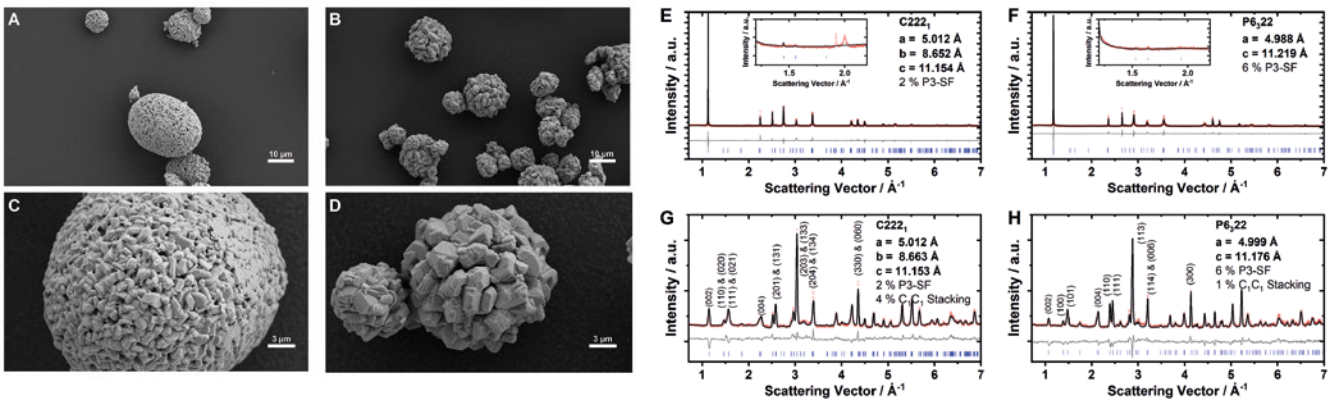

Figure 1: SEM images of the as-synthesised powders for (A, C) $Na_{2/3}Ni_{1/3}Mn_{2/3}O_2$ and (B, D) $Na_{0.60}Mn_{3/4}Ni_{1/4}O_2$. XRD data with refinement for (E) $Na_{2/3}Ni_{1/3}Mn_{2/3}O_2$, where reflections at Q = 1.9 Å^{-1} and 2.0 Å^{-1} originate from Na^+/vacancy orderings and (F) $Na_{0.60}Mn_{3/4}Ni_{1/4}O_2$, where they are absent. Neutron diffraction data with refinement for (G) $Na_{2/3}Ni_{1/3}Mn_{2/3}O_2$ and (H) $Na_{0.60}Mn_{3/4}Ni_{1/4}O_2$ indicate a Ni/Mn honeycomb ordering with predominantly C_2C_3 stacking sequence.

The relationship between anisotropic peak broadening and lattice symmetry in powder diffraction

P. Fabrykiewicz [1,2]

[1] Institute of Crystallography, RWTH Aachen University, Aachen, Germany;
[2] Jülich Centre for Neutron Science (JCNS) at MLZ, Forschungszentrum Jülich GmbH, Garching, Germany

Anisotropic peak broadening caused by lattice relaxation in powder diffraction can be modelled within the phenomenological model of anisotropic peak broadening. This approach shows the existence of specific relations between anisotropic peak broadening parameters that can be used to indicate an unresolved peak splitting due to lattice symmetry lowering.

Phenomenological model of anisotropic peak broadening

Anisotropic peak broadening, which is characterised by a peak width that is not a smooth function of d-spacing, is a common occurrence in powder diffraction patterns. This phenomenon is often modelled using a phenomenological approach which assumes that each crystallite in a polycrystalline sample is generally triclinic, and that only the average lattice parameters across the entire sample fulfil the restrictions of a given lattice symmetry. In this approach, the anisotropic contribution to the peak width is expressed as a fourth-order polynomial in the *h*, *k*, *l* indices. The polynomial coefficients (S_{HKL}) are linear combinations of the elements of the covariance matrix that describe the distribution of the lattice parameters in the polycrystalline sample. This approach is often used to improve the quality of the fit, due to its widespread implementation in Rietveld refinement software. However, the refined values of the S_{HKL} coefficients are rarely discussed.

A bridge between anisotropic peak broadening and lattice relaxation

Lattice relaxation, i. e. lattice symmetry lowering, leads to shifts in the positions of low-symmetry peaks in powder diffraction. The variance of slightly dispersed peaks' positions can be used to parameterise the anisotropic peak broadening caused by lattice relaxation. Calculating the variances for the relaxation schemes [1] gives a fourth-order polynomial in the *h*, *k*, *l* indices, which is analogous to that in the phenomenological anisotropic peak broadening model discussed above. However, the polynomial coefficients S_{HKL} are now proportional to the square of the lattice parameter increment, i. e. lattice distortion [1]. Furthermore, this approach imposes stronger restrictions on the S_{HKL} parameters than the phenomenological approach [1] as shown in Fig. 1. Fulfilling these stronger constraints could indicate possible unresolved peak splitting due to lattice symmetry lowering.

[1] P. Fabrykiewicz, A note on the relation of anisotropic peak broadening with lattice symmetry in powder diffraction, Acta Crystallogr. Sect. A 81, 245 (2025)
DOI: 10.1107/S2053273325003134

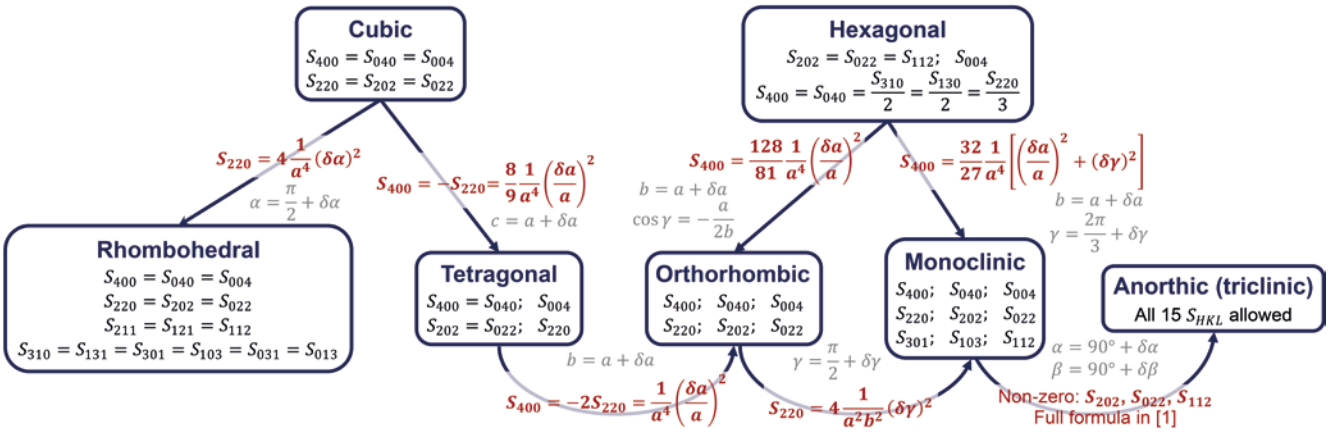

Figure 1: Each box represents a lattice and contains symmetry restrictions on the S_{HKL} coefficients. Each arrow denotes one of the lattice relaxation schemes specified by the grey equations. Calculating the variance of slightly dispersed peaks' positions due to each lattice relaxation scheme enables the S_{HKL} to be expressed in terms of lattice parameter increments, as shown by the red equations at the top of the arrows [1]. The value of the unlisted S_{HKL} coefficients is zero.

Field-induced quantum criticality and dimensional reduction of the sawtooth-chain compound atacamite

L. Heinze[1,2], T. Kotte[3], R. Rausch[4], A. Demuer[5], S. Luther[3], R. Feyerherm[6], E. L. Q. N. Ammerlaan[7], U. Zeitler[7], D. I. Gorbunov[3], M. Uhlarz[3], K. C. Rule[8], A. U. B. Wolter[9], H. Kühne[3], J. Wosnitza[3,10], C. Karrasch[4], S. Süllow[1]

[1] Institut of Condensed Matter Physics, TU Braunschweig, Braunschweig, Germany; [2] Jülich Centre for Neutron Science (JCNS) at MLZ, Forschungszentrum Jülich GmbH, Garching, Germany; [3] Dresden High Magnetic Field Laboratory (HLD-EMFL), HZDR, Dresden, Germany; [4] Institute of Mathematical Physics, TU Braunschweig, Braunschweig, Germany; [5] Laboratoire National des Champs Magnétiques Intenses, CNRS, Grenoble, France; [6] Helmholtz-Zentrum Berlin für Materialien und Energie GmbH, Berlin, Germany; [7] High Field Magnet Laboratory (HFML-EMFL), Radboud University, Nijmegen, The Netherlands; [8] Australian Nuclear Science and Technology Organisation, Lucas Heights, Australia; [9] Leibniz Institute for Solid State and Materials Research IFW Dresden, Dresden, Germany; [10] Institute of Solid State and Materials Physics, TU Dresden, Dresden, Germany

Atacamite $Cu_2Cl(OH)_3$, a dark green mineral named after its type locality in the Atacama Desert, has been found to represent a frustrated quantum magnet in which field-driven quantum criticality can be studied using macroscopic and microscopic measurement techniques. Its quantum critical point sits at 21.9(1) T (**H** || *c* axis) and it separates field regions with and without long-range order, although far from full field polarisation.

Frustrated quantum magnets such as atacamite are characterised by highly degenerate magnetic ground states, which makes them especially susceptible to tuning by applied pressure or external magnetic field. As a result, quantum phase transitions can occur which are driven by these external tuning parameters. In atacamite, the dominant exchange couplings form antiferromagnetic sawtooth chains with the exchange coupling J = 336 K running along the basal sites of the chain and J' = 102 K coupling basal and apical sites (Fig. 1a). Weak interchain couplings lead to long-range order below T_N = 8.9(1) K.

Unusual magnetisation and suppressed order

Experimentally, atacamite stands out through its unusual magnetisation closely resembling a wide 1/2-plateau with an abrupt flattening of the magnetisation at 21.9(1) T (Fig. 1b). It is in conjunction with this curious magnetisation behaviour that long-range magnetic order vanishes, as evidenced by ^{1}H-NMR in high magnetic fields (Fig. 1c). This applied-field behaviour is remarkable given that the material is still far from full field polarisation. The entropy landscape of atacamite is highly distorted, indicative of a quantum critical point at 21.9(1) T (Fig. 1d).

Dimensional reduction at half-saturation

Corroborated by numerical calculations, the quantum phase transition was found to be associated with a dimensional reduction of the spin system: When the spins on the apical sites of the chains are fully polarised by the external magnetic field, the exchange couplings between the sawtooth chains are effectively broken up and hence the long-range antiferromagnetic order is suppressed. The experimental observations support a high-field state of weakly polarised, disorganised basal spins in the spin-polarised background of the apical spins.

[1] L. Heinze et al., Atacamite $Cu_2Cl(OH)_3$ in high magnetic fields: Quantum criticality and dimensional reduction of a sawtooth-chain compound, Phys. Rev. Lett. 134, 216701 (2025)

DOI: 10.1103/PhysRevLett.134.216701

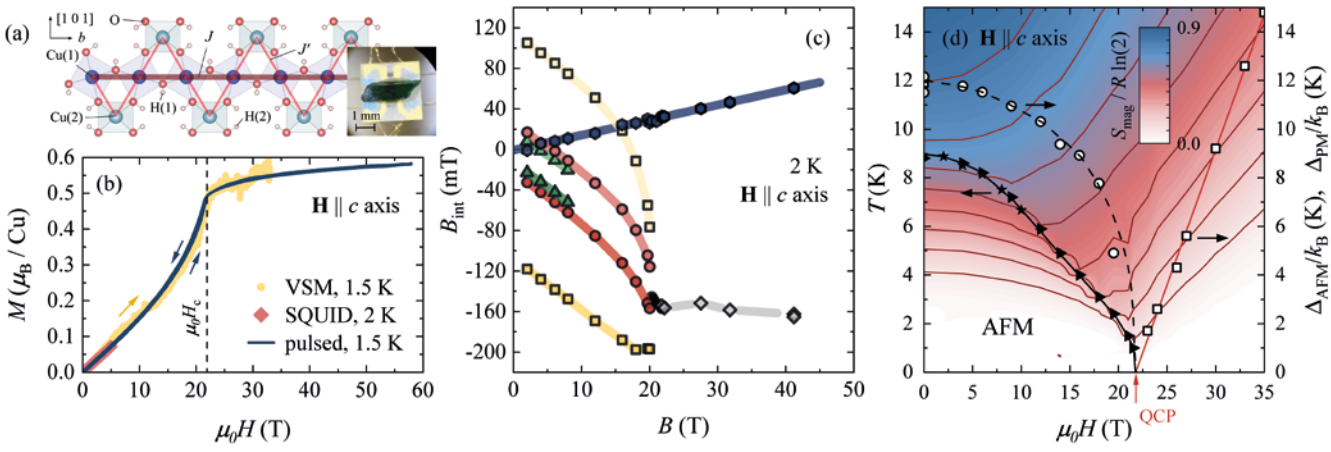

Figure 1: (a) Sawtooth-chain unit in atacamite formed by Cu(1) (basal) and Cu(2) (apical) sites. Inset: Atacamite single crystal on a puck for heat-capacity measurements. (b) High-field magnetisation of atacamite in dc as well as pulsed magnetic fields **H** || *c* axis. (c) Field dependence of the internal fields B_{int} of the individual resonance lines from ^{1}H-NMR for **H** || *c* axis. (d) Distorted entropy landscape of atacamite (**H** || *c* axis).

Magnetism of a frustrated triangular lattice antiferromagnet

N. Biniskos[1], F. J. dos Santos[2], M. Stekiel[3], K. Schmalzl[2,4], E. Ressouche[4], D. Sviták[1], A. Labh[1], M. Vališka[1], N. Marzari[4], P. Čermák[1]

[1] Faculty of Mathematics and Physics, Department of Condensed Matter Physics, Charles University, Prague, Czech Republic; [2] Paul Scherrer Institute (PSI), Centre for Scientific Computing, Villigen, Switzerland; [3] Jülich Centre for Neutron Science (JCNS) at MLZ, Forschungszentrum Jülich GmbH, Garching, Germany; [4] Institut Laue-Langevin (ILL), Grenoble, France

Neutron diffraction and heat capacity measurements reveal that $Na_2BaMn(PO_4)_2$, a spin-5/2 triangular-lattice antiferromagnet, hosts a rich set of field-induced magnetic phases. Guided by X-ray diffraction results and Monte Carlo modelling, we show that subtle frustrated interlayer couplings govern the evolution of the spin structures and the finite-temperature phase diagram.

Magnetic materials built from triangular lattices are known for their frustration, where competing interactions prevent simple magnetic order. Among them, systems with spin-½ and antiferromagnetic nearest-neighbour interactions are model systems envisioned to host exotic quantum properties. Such systems are, however, difficult to investigate experimentally due to their low magnetic moment and the fact that interactions beyond nearest-neighbours are almost always present in crystals. Here, we study manganese sodium phosphate (NBMPO), a representative of the $Na_2BaT(PO_4)_2$ (T = transition metal) family, which realises the triangular lattice antiferromagnet model. By investigating a compound with an elevated spin number, we enhance the magnetic scattering and gain insight into the mechanisms governing the behaviour of the corresponding spin-½ system.

Neutron diffraction uncovers a complex phase diagram

Based on the measurements at D23@ILL and complementary heat capacity data, we constructed the phase diagram of NBMPO, see Fig. 1a. The phase diagram hosts multiple incommensurate magnetic phases, evolving from an incommensurate Y-phase ground state. We also identify a pocket of the up-up-down phase, a hallmark of frustrated magnets. The presence of incommensurate order is unexpected and calls for an extension of the nearest-neighbour model.

Structure explains the hidden complexity

We carefully examined the structure of NBMPO single crystals using X-ray diffraction at the MLZ laboratories and identified subtle symmetry breaking that lifts the degeneracy of the interlayer couplings. Further Monte Carlo simulations confined the magnetic structure and show that two distinct interlayer interactions drive the observed interlayer spiralisation. On this basis, we develop a minimal microscopic model that reproduces the full magnetic phase diagram of NBMPO and deepens our understanding of triangular-lattice antiferromagnets.

[1] N. Biniskos et al., Spin structures and phase diagrams of the spin-5/2 triangular lattice antiferromagnet $Na_2BaMn(PO_4)_2$ under magnetic field, Phys. Rev. B 112, 174429 (2025) DOI: 10.1103/kszh-m6bf

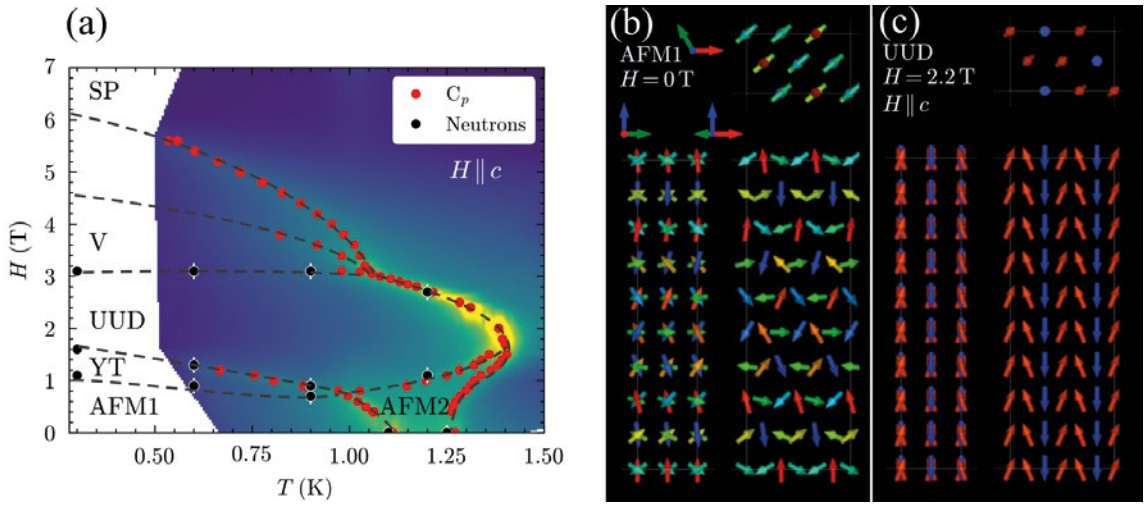

Figure 1: Multiple magnetic phases stabilised by applied field and thermal fluctuations in $Na_2BaMn(PO_4)_2$. (a) Phase diagram determined by neutron diffraction, showing several magnetic phases stabilised by field and evolving from the antiferromagnetic ground state, AFM1. The ground state is a Y phase (b), characterised by an out-of-plane, coplanar spin arrangement. An applied magnetic field stabilises the up-up down phase (c), a hallmark of frustrated magnetic systems.

Crystal growth and magnetic properties of the room-temperature van der Waals ferromagnet Fe_3GaTe_2

P.-C. Chang[1,2], Y. Zhou[1], Y.-H. Tung[1], S. Hammouda[1], C.-M. Liu[3], M. Skoulatos[4], C.-H. Du[2], W.-C. Lin[3], Y. Su[1]

[1] Jülich Centre for Neutron Science (JCNS) at MLZ, Forschungszentrum Jülich GmbH, Garching, Germany; [2] Department of Physics, Tamkang University, New Taipei City, Taiwan; [3] Department of Physics, National Taiwan Normal University, Taipei, Taiwan; [4] Heinz Maier-Leibnitz Zentrum (MLZ), Technical University of Munich, Garching, Germany

Fe_3GaTe_2 (FGaT) is a room-temperature ferromagnetic two-dimensional van der Waals (vdW) material that possesses a perpendicular magnetic anisotropy and exotic magnetic skyrmion phases. High-quality single-crystal samples are a prerequisite for a detailed investigation of the physical properties of this extraordinary material. We have grown high-quality, large single crystals using self-flux and chemical vapor transport (CVT) methods and characterised their structural and magnetic properties. This paves the way for a wide range of experimental studies of this compound, including magnetic force microscopy and single-crystal neutron diffraction.

Crystal growth and characterisation of FGaT

Two single-crystal growth methods, self-flux and CVT, were employed to synthesise FGaT single crystals. In the self-flux method, Fe, Ga, and Te were mixed in a molar ratio of 1:1:2. However, energy-dispersive X-ray spectroscopy indicated the presence of Ga_2Te_3 impurity phases on the crystal surface, which limit crystal size and purity for single-crystal neutron diffraction experiments. High-quality FGaT single crystals were subsequently grown using the CVT method. High-purity Fe, Ga, and Te were mixed in a stoichiometric ratio of 3:1:2 and sealed in an evacuated quartz ampoule with iodine (2 mg/cm^3) as the transport agent. The ampoule was placed in a two-zone furnace with a temperature gradient of 760–710°C for 7 days and then naturally cooled to room temperature. XRD and vibrating sample magnetometry measurements confirm that the CVT-grown FGaT crystals adopt a hexagonal layered structure with space group $P6_3/mmc$ (a = b = 4.08 Å, c = 16.09 Å) and exhibit no detectable impurity phases (Fig. 1a, b). Temperature-dependent magnetisation measurements reveal a clear ferromagnetic transition with a Curie temperature $T_C \approx 367$ K. Room-temperature magnetic hysteresis loops show that the out-of-plane saturation field is approximately one order of magnitude smaller than the in-plane value, demonstrating strong perpendicular magnetic anisotropy (Fig. 1c, d).

Localised bubble domains by conductive AFM

In this study, conductive atomic force microscopy (c-AFM) was used to locally generate magnetic bubble domains on the surface of FGaT. Under an applied out-of-plane magnetic field, a current was injected through the AFM tip to induce localised heating on the FGaT surface. Upon cooling, the locally heated regions stochastically transformed the original stripe domain configuration into magnetic bubble domains. Magnetic force microscopy (MFM) images (Fig. 1e, f) confirm that the bubble domains are stable at room temperature under ambient conditions. In addition, we have carried out a single-crystal neutron diffraction experiment for the determination of the magnetic structure of FGaT, which will be reported elsewhere.

[1] C.-M. Liu et al., Localised creation of bubble domains in Fe_3GaTe_2 by conductive atomic force microscopy, Appl. Surf. Sci. Adv. 26, 100718 (2025)
DOI: 10.1016/j.apsadv.2025.100718

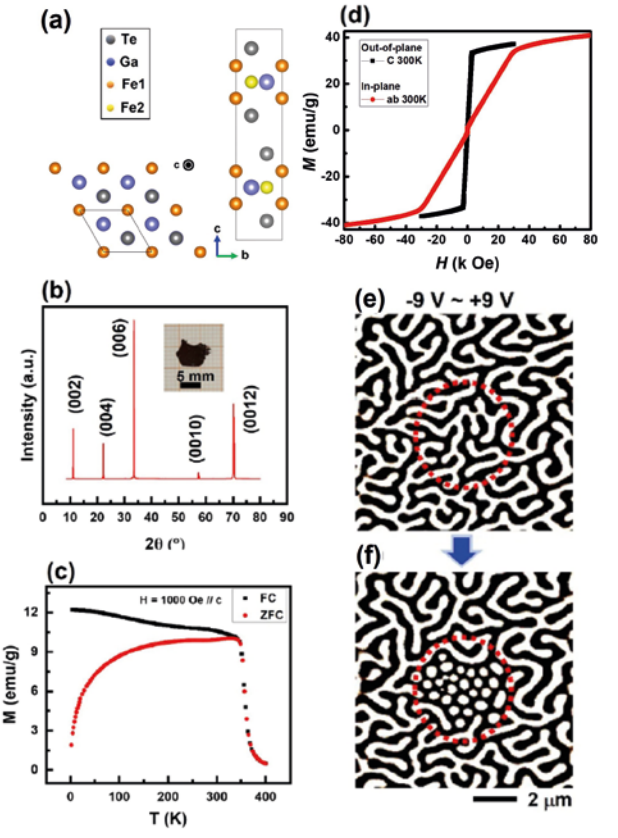

Figure 1: (a) Schematic side view of the vdW structure of FGaT. (b) XRD pattern measured along the c axis. (c) Temperature-dependent magnetisation measured under field-cooled (FC) and zero-field-cooled (ZFC) conditions. (d) Out-of-plane and in-plane magnetic hysteresis loop at RT. MFM images before and after applying bias voltage: (e) pristine domain structures, (f) dashed circles highlight newly formed bubble domains [1].

Ground-state magnetic structures of topological kagome metals RV_6Sn_6 (R = Tb, Dy, Ho, Er)

Y. Zhou[1,2], M.-K. Lee[3], S. Hammouda[1], S. Devi[1], S.-I. Yano[4], R. Sibille[5], O. Zaharko[5], W. Schmidt[6], K. Schmalzl[6], K. Beauvois[7], E. Ressouche[7], P.-C. Chang[1,8], C.-H. Huang[1], L.-J. Chang[3], T. Brückel[9], Y. Su[1]

[1] Jülich Centre for Neutron Science (JCNS) at MLZ, Forschungszentrum Jülich GmbH, Garching, Germany; [2] Department of Physics, TUM School of Natural Sciences, Technical University of Munich, Garching, Germany; [3] Department of Physics, National Cheng Kung University, Tainan, Taiwan; [4] National Synchrotron Radiation Research Centre, Hsinchu, Taiwan; [5] Laboratory for Neutron Scattering and Imaging, Centre for Neutron and Muon Sciences, Paul Scherrer Institute (PSI), Villigen, Switzerland; [6] Jülich Centre for Neutron Science (JCNS) at ILL, Forschungszentrum Jülich GmbH, Grenoble, France; [7] Université Grenoble Alpes, CEA, IRIG, MEM, MDN, Grenoble, France; [8] Department of Physics, Tamkang University, New Taipei City, Taiwan; [9] Jülich Centre for Neutron Science (JCNS) and Peter Grünberg Institute, JARA-FIT, Forschungszentrum Jülich GmbH, Jülich, Germany

V-based topological kagome metals RV_6Sn_6 (R = rare-earth element) exhibit a unique lattice geometry that can give rise to exotic electronic and magnetic phenomena, making them an ideal platform to study the interplay of topology and magnetism. To unravel their ground-state magnetic structures at very low temperatures, we have carried out comprehensive in-house characterisations and single-crystal neutron diffraction experiments on a series of RV_6Sn_6 compounds. These results allow to gain new insights into the complex magnetic interactions and diverse single-ion magnetic anisotropies in these compounds.

RV_6Sn_6: A novel topological quantum material

The recently discovered kagome metal RV6Sn6 series has attracted strong interests due to rich quantum phenomena and high diversity in magnetic properties, in which a magnetic R triangular layer is sandwiched between the non-magnetic V kagome bilayers, and the magnetic interaction is mainly contributed from the intralayer and interlayer R-R couplings. High-quality single crystals of RV_6Sn_6 (R = Tb, Dy, Ho, Er) were successfully grown via the flux method. Systematic investigations of crystal structure, low-temperature magnetic and thermodynamic properties of these compounds were performed via various in-house characterisation techniques. These studies pave the way for a microscopic investigation of magnetic order at low temperatures in these compounds via neutron scattering.

Ground-state magnetic structures in RV_6Sn_6

Using single-crystal neutron diffraction, we confirm the occurrence of a long-range magnetic order respectively below 4.3 K (Tb), 3.0 K (Dy), 2.4 K (Ho) and 0.6 K (Er) in these compounds. The ground-state magnetic structures of the studied compounds, including magnetic propagation vector and the size and direction of the ordered magnetic moment, are comprehensively determined via single-crystal neutron diffraction and magnetic crystallography refinements. As shown in Fig. 1, TbV_6Sn_6 and HoV_6Sn_6 are collinear ferromagnets with the ordered magnetic moments aligned along the c axis. DyV_6Sn_6 is also ferromagnetic but with the ordered magnetic moment tilted by about 20° away from the c axis. In contrast, ErV_6Sn_6 orders in an A-type antiferromagnetic structure with a magnetic propagation vector $\boldsymbol{k}$ = (0,0,0.5) and the ordered magnetic moment aligned in the ab-plane. The ordered magnetic moments are determined at 9.4(2), 6.6(2), 6.4(2) and 6.1(3) μB for R = Tb, Dy, Ho and Er, respectively. Together with bulk magnetisation and specific-heat measurements down to 50 mK, these results provide a quantitative microscopic benchmark for the RV_6Sn_6 series and a reference for comparison with the RMn_6Sn_6 kagome metal family.

The neutron diffraction experiments were performed at Sika (ANSTO), D23 (ILL) and Zebra (SINQ, PSI).

[1] Y. Zhou et al., Ground-state magnetic structures of topological kagome metals RV_6Sn_6 (R = Tb, Dy, Ho, Er), Phys. Rev. Res. 6, 043291 (2024)
DOI: 10.1103/PhysRevResearch.6.043291

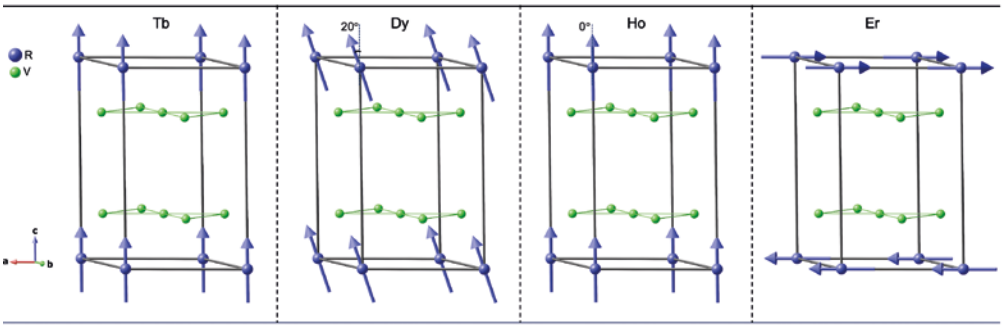

Figure 1: The ground-state magnetic structures of the topological kagome metals RV_6Sn_6 (R = Tb, Dy, Ho, Er) series, determined via single-crystal neutron diffraction [1]. Tb and Ho are collinear ferromagnets with moments along c; Dy is ferromagnetic with the moment tilted ~20° from c. Er shows A-type antiferromagnetism with $\boldsymbol{k}$ = (0,0,0.5) and in-plane moments.

Rotational magnetoelastic interactions in the Dzyaloshinskii-Moriya magnet $Ba_2CuGe_2O_7$

J. Sourd[1], T. Kotte[1], P. Wild[2], S. Mühlbauer[2], J. Wosnitza[1,3], S. Zherlitsyn[1]

[1] Dresden High Magnetic Field Laboratory (HLD-EMFL) and Würzburg-Dresden Cluster of Excellence ct.qmat, Helmholtz-Zentrum Dresden-Rossendorf (HZDR), Dresden, Germany; [2] Heinz Maier-Leibnitz Zentrum (MLZ), Technical University of Munich, Garching, Germany; [3] Institute of Solid State and Materials Physics, TU Dresden, Dresden, Germany

We report the magnetoelastic properties of $Ba_2CuGe_2O_7$ at low temperatures under a magnetic field applied along the tetragonal [001] axis. Our results extend the phase diagram determined for this compound by neutron scattering. In particular, we observe an unusual coupling between the transverse acoustic mode in the (001) plane and the cycloidal order at low field, which suggests a spin-strain mechanism caused by the Dzyaloshinskii-Moriya interaction.

The study of multiferroic materials, where multiple electric, magnetic, or elastic orders coexist, has been a very fruitful topic in recent decades, with important outcomes for both fundamental research and technological developments. In particular, significant effort has been made to identify the different mechanisms leading to the coexistence of electric and magnetic polarisations, starting from the microscopic constituents of a given material such as the spin, lattice, and orbital degrees of freedom.

Current state of knowledge

$Ba_2CuGe_2O_7$ is an antiferromagnetic insulator characterised by a tetragonal, non-centrosymmetric space group ($P\text{-}42_1m$, lattice parameters a = 8.466 Å, c = 5.445 Å) that exhibits both electric and magnetic ordering. The low temperature behaviour of $Ba_2CuGe_2O_7$ has been the subject of numerous experimental and theoretical studies establishing a long-range incommensurate, almost AF cycloidal spin spiral below the Néel temperature T_N ~3.05 K and a rich phase diagram for magnetic fields applied along the tetragonal [001] axis that has recently been theoretically described in great detail using a non-linear sigma model for the free energy density.

Unusual magnetoelastic coupling

In this paper, we present a detailed study of the magnetoelastic properties of $Ba_2CuGe_2O_7$ at low temperatures investigated by means of ultrasound measurements (Fig. 1). This technique makes it possible to scrutinise various acoustic modes of definite symmetry. This method is also sensitive to the quadrupole degrees of freedom. In our work, we reveal an unusual coupling between the magnetic order and the transverse acoustic modes in $Ba_2CuGe_2O_7$, expected from an involvement of quadrupolar degrees of freedom. Moreover, we show that this effect can be accounted for by considering the Dzyaloshinskii-Moriya interaction in the presence of strain. This leads to a specific spin-lattice coupling, having symmetry signatures different from the well-known exchange-striction mechanism.

[1] J. Sourd et al., Rotational magnetoelastic interactions in the Dzyaloshinskii-Moriya magnet $Ba_2CuGe_2O_7$, Phys. Rev. B 111, 224411 (2025)
DOI: 10.1103/PhysRevB.111.224411

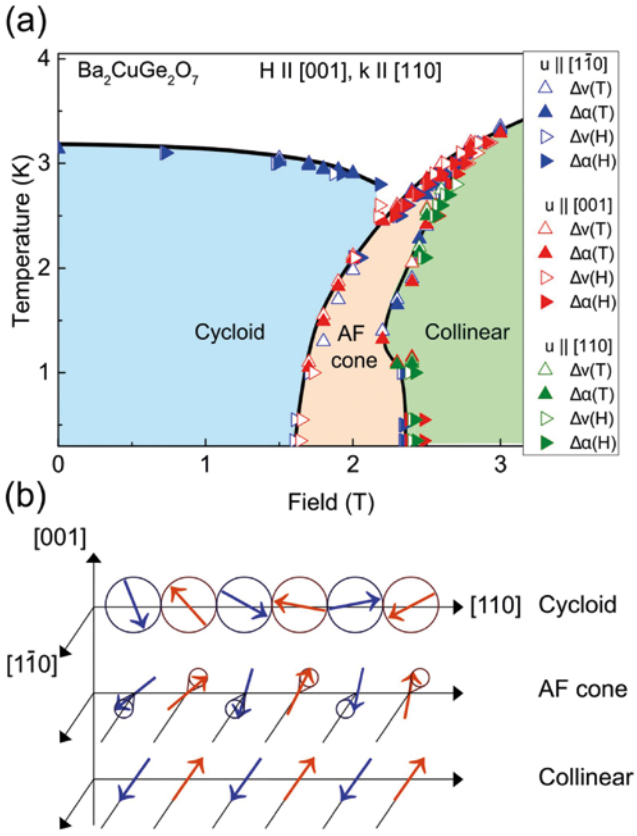

Figure 1: (a) Phase diagram constructed from the ultrasound results. (b) Sketch of the different magnetic orders determined from neutron diffraction. In the AF cone phase, the cone opening direction is [1 – 10].

Local reorganisation of the intermediate mixed state in niobium below the critical depinning current

X. S. Brems[1,2], S. Mühlbauer[2], R. Cubitt[1]

[1] Institut Laue-Langevin (ILL), Grenoble, France;
[2] Heinz Maier-Leibnitz Zentrum (MLZ), Technical University of Munich, Garching, Germany

The intermediate mixed state (IMS) under the influence of a transport current was studied using SANS. The internal magnetic domain structure consisting of a mixed state and flux free Meissner state was observed to rearrange at intermediate currents well before the critical depinning current. The local reorganisation is inherently linked to the interplay of the pinning landscape with the vortex lattice domain structure governed by the physics of the IMS.

Superconductors are classified based on their response to magnetic fields. Type-I superconductors expel an external magnetic field, referred to as the Meissner state, whereas type-II superconductors exhibit a second phase called the mixed state, in which the magnetic field enters in the form of flux lines. For superconductors with a Ginzburg-Landau parameter close to $\kappa_0 = 1/\sqrt{2}$, we find a broad range of degenerate exotic flux structures subsumed under the term intertype (IT) superconductivity. One of the most prominent manifestations of IT superconductivity is the IMS in niobium where Meissner state domains are interspersed with mixed state domains on the µm scale. In the IMS, vortex clustering can be explained via a partially attractive vortex interaction.

Intricate physics behind IMS rearrangement

Until recently, the effect of transport currents on the IMS domain structure in niobium remained experimentally unexplored. At the onset of flux flow marked by a finite voltage, the initial random domain structure of the IMS was found to rearrange into stripes parallel to the vortex motion and perpendicular to the applied current. It was argued that the rearrangement process is closely related to the underlying physics of the IMS leading to a vortex velocity that depends on the cluster size resulting in the rearrangement to stripes aligned along the direction of vortex motion. In this follow-up study, we focus on extending the range of currents and fields. The observation of the current-induced self-organisation into a stripe structure is confirmed. Additionally, by investigating currents below the critical depinning current I_{cV}, we find that the stripes are formed for currents well below I_{cV} (Fig. 1). The absence of similar precursors in the homogeneous mixed state points to a unique mechanism linked to the IMS. The rearrangement for currents $I < I_{cV}$ is attributed to the interplay of the underlying pinning landscape with the IMS domain structure governed by the intricate physics of the IMS. Our results highlight that the current-induced reorganisation of the IMS acts as a model system for studying complex ordering and reveals a rich area of physics.

The experiments were performed at the small-angle neutron scattering diffractometer D33 at ILL.

[1] X. S. Brems et al., Local reorganisation of the intermediate mixed state in niobium below the critical depinning current, Supercond. Sci. Technol. 38, 025004 (2025) DOI: 10.1088/1361-6668/ad9fe9

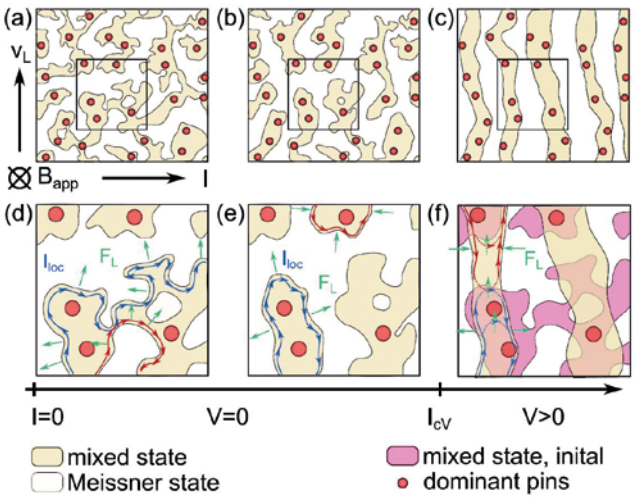

Figure 1: Schematic representation of the rearrangement process. (a) Pristine state: The domain structure is formed around strong pinning sites. (b) Gradual rearrangement of the domain structure for currents $I < I_{cV}$. (c) Domain structure in the flux flow state. The continuous flow of vortices induces a finite voltage. (d)–(f) Zoom on the domain structure within the black square shown in the first row showing the local current path and the resulting Lorentz force.

Quantifying Å-scale non-additive solvation at nanoparticle interfaces

X. Liu[1,2], N. Cai[1], Z. Liu[3], L. Zhu[1], Z. Chen[1], A. Radulescu[4], L. Porcar[5], H. Jiang[6,7], Y. Ke[6,7], Z. Luo[1]

[1] Guangdong Provincial Key Laboratory of Advanced Biomaterials, Department of Biomedical Engineering, Southern University of Science and Technology, Shenzhen, Guangdong, China; [2] Department of Biomedical Engineering, National University of Singapore, Singapore; [3] Department of Chemical and Biomolecular Engineering, National University of Singapore, Singapore; [4] Jülich Centre for Neutron Science (JCNS) at MLZ, Forschungszentrum Jülich GmbH, Garching, Germany; [5] Institut Laue-Langevin (ILL), Grenoble, France; [6] Institute of High Energy Physics, CAS, Beijing, China; [7] Spallation Neutron Source Science Centre, Dongguan, China

This work overturns the uniform solvent assumption of the colloid theory and shows that bulk nonideal mixing governs Å-scale interfacial solvation. Using SANS data measured at KWS-2, we revealed the solvent clustering and anisotropic deformation of ligand shells at nanoparticle surfaces for the first time. Our findings challenge the foundational premise of additivity and isotropy in classical models and confirm theoretical predictions of non-additive solvation behaviour.

Anisotropic deformation of ligand shells

Using analytical core-shell modelling combined with Monte-Carlo real-space reconstruction, we tracked how binary solvent mixtures reorganise within ligand coronas. In $CDCl_3$-MeOD and $CDCl_3$-THF mixtures, ellipsoid models consistently outperformed spherical descriptions, demonstrating the reversible deformation of ligand shells from near-isotropic to highly prolate geometries. Shell anisotropy, thickness, and preferential solvent uptake all displayed pronounced nonlinear dependence on solvent composition. Strikingly, maxima in anisotropy and solvent inclusion coincided precisely with each mixture's azeotropic composition, indicating that deviations from ideal mixing directly modulate interfacial structure.

Non-ideal mixing and azeotropes

Contrast-variation SANS of the pure solvent mixtures uncovered Å-scale composition fluctuations whose correlation lengths peaked at the azeotrope (Fig. 1). These transient clusters infiltrate ligand shells, amplifying local composition deviations and breaking spherical symmetry – a mechanism reproduced across ligands (C12 vs. C18) and chemically distinct solvent pairs. Thus, solvation at curved interfaces is governed not by continuum polarity but by discrete solvent microstructures.

Overall, this study establishes a quantitative experimental link between bulk non-ideal mixing and nanoscale interfacial symmetry. Solvent-driven interfacial phenomena affect heterogeneous catalysis, drug-delivery nanocarriers, electrochemical interfaces, and polymer-based soft materials. Our method represents a generalisable, broadly applicable tool for quantitatively exploring solvent structuring across diverse chemical contexts.

[1] X. Liu et al., Quantifying Å-scale non-additive solvation at nanoparticle interfaces, Angew. Chem. Int. Ed. 64, e202516308 (2025)
DOI: 10.1002/anie.202516308

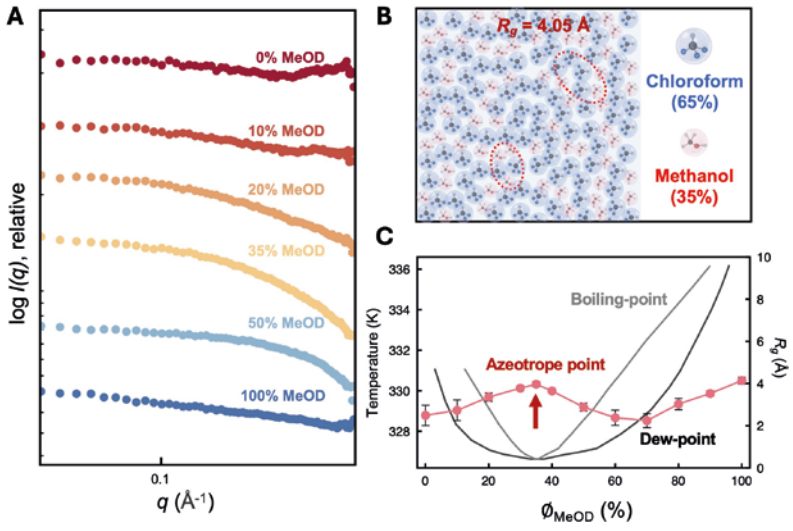

Figure 1: (A) SANS profiles of $CDCl_3$-MeOD mixtures. (B) Schematic illustration of transient $CDCl_3$-MeOD mixture clustering near the azeotrope. (C) Plots of $CDCl_3$-MeOD mixtures R_g values, together with the phase diagram of chloroform-methanol. The boiling-point and dew-point curves were plotted in grey and black, respectively. Error bars represent the standard deviations derived from the nonlinear least-squares fitting in PRIMUS.

Coherent multiple scattering in small-angle scattering experiments

H. Frielinghaus [1], C. J. Gommes [2]

[1] Jülich Centre for Neutron Science (JCNS) at MLZ, Forschungszentrum Jülich GmbH, Garching, Germany;
[2] Department of Chemical Engineering, University of Liège, Liège, Belgium

The transition from weak scattering with only single-scattering events to stronger and stronger multiple scattering in small-angle scattering experiments is described. When the coherent multiple scattering emerges – similar to the Mie scattering in light scattering – resonances at the colloidal surface develop and the scattering experiment reveals the surface scattering instead of classical bulk scattering.

What is its origin?

Weakly scattering samples can be described by the classical Born approximation, where scattering events happen only once for the neutron travelling inside the sample. When multiple scattering of strongly scattering samples starts to emerge [1], the first stage is connected to independently occurring scattering events over larger distances. Even stronger multiple scattering brings the scattering events closer and closer, such that the structural correlation length ξ is similar to, or larger than, the distance of the events. Here, the signals superimpose coherently or collectively – similar to the well-known Mie scattering in light scattering. When this effect slowly emerges, the collective scattering effects describe resonances at the surface of the colloidal structures. Consequently, the surface of the structure starts to display instead of the bulk structure that is observed in the classical 1st order Born approximation.

Surface interferences

For neutrons, there is a quantum mechanical theory without polarisation that corresponds to the Mie theory for electromagnetic light waves. This description is formulated exactly for simple colloidal shapes like spheres and cylinders. In parallel, the Born theory can be expanded to higher order terms describing multiple scattering, where surface scattering terms can be identified. The relative forward scattering (Fig. 1) as a function of the parameter $\kappa = |\Delta\rho|R/k$ describes the transition at $\kappa \approx 0.1$ from the classical Born approximation with a single scattering event to coherent multiple scattering. Here, $|\Delta\rho|$ is the scattering length density difference (or contrast) between the colloid and the solvent, R is the radius of the colloid, and k is the wavevector of the neutron. In a wide-range q-scan employing ultra and very small angle neutron scattering and classical small angle neutron scattering, the critical scattering vector $q_c = 8\pi|\Delta\rho|/k$ is connected to this transition. For smaller $q < q_c$, the surface scattering dominates, and for larger $q > q_c$ the classical bulk scattering displays.

[1] H. Frielinghaus et al., Coherent multiple scattering in small-angle scattering experiments: modelling approximations based on the Born expansion, J. Appl. Crystallogr. 58, 1553 (2025)
DOI: 10.1107/S1600576725006685

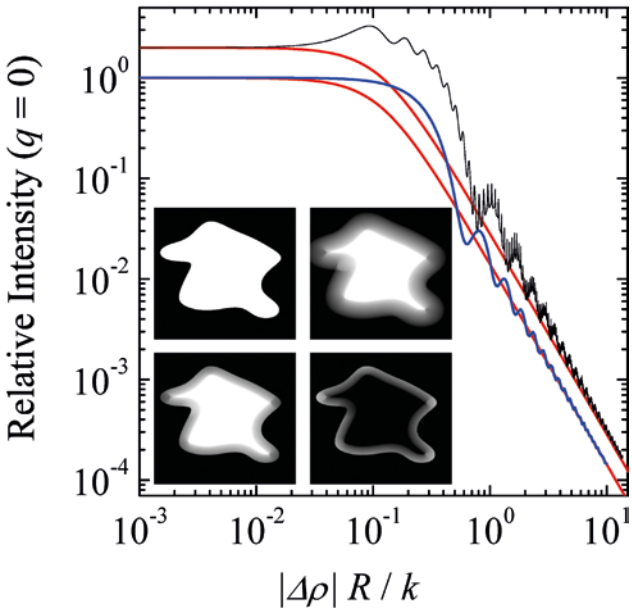

Figure 1: Relative forward scattering as a function of $\kappa = |\Delta\rho|R/k$ (different conditions for blue and shifted black lines). At $\kappa \approx 0.1$, the relative forward scattering leaves the plateau value of unity and displays oscillatory behaviour for the resonances that merge in the asymptotic κ^{-2} behaviour (simplified red line). These surface resonances appear as surface scattering in the experiment (surface terms are derived from the higher order Born expansion terms, see inlay).

Gamma ray detectors for 2D-measurements of the angular correlation of annihilation radiation (2D-ACAR)

K. Brenner[1,2], F. Guatieri[1], C. Hugenschmidt[1]

[1] Heinz Maier-Leibnitz Zentrum (MLZ), Technical University of Munich, Garching, Germany;
[2] Department of Physics, TUM School of Natural Sciences, Technical University of Munich, Garching, Germany

We tested a new detector prototype for 2D-ACAR measurements using two pixelated LYSO scintillation crystals in combination with Hamamatsu silicon photomultipliers. A larger implementation of this prototype will be used to drastically improve resolution and count rate. The prototype achieved a spatial resolution of 1 mm and a detection efficiency five times higher compared to that of NaI(Tl) previously used in our Anger cameras, leading to a 25 times higher coincidence count rate.

2D-ACAR is a measurement method to determine the bulk electronic structure by using positrons. The annihilation of thermalised positrons with electrons leads predominately to the emission of two 511 keV photons. In the laboratory frame, the transverse components of the electron momentum result in a proportional deviation of the emission angle from 180°. For 2D-ACAR measurements, both annihilation quanta are detected simultaneously with two spatially resolved detectors. A single ACAR-spectrum delivers a planar 2D-projection of the electron momentum distribution. The 3D distribution of the electron momenta in the crystal can be reconstructed by combining spectra recorded with different sample orientations.

Structure of the detector

The detector (shown in Fig. 1) comprises a lutetium-yttrium oxyorthosilicate (LYSO) scintillator, a thin glass light guide, a multi-pixel-photon-counter (MPPC) and two adapters (custom designed for this setup to allow for easier testing). The scintillator, the light guide and the MPPC are connected with optical grease. The rightmost adapter connects the detector to the TOFPET2 readout by PETsys electronics. The entire detector stack is housed in a 3D-printed light shield.

Measurements and results

Benchmarks of the detector showed a spatial resolution of 1 mm and an average crystal pixel dependent energy resolution of 14.3% (at 511 keV). The absorption efficiency at 511 keV was simulated to be 65.4% (27.0% photopeak), which is five times better than the previous system. As proof of concept, a 2D-ACAR measurement of copper was conducted. The extracted Fermi-energy of copper matches the literature values; however, the resolution was limited due to the small detector size. Additionally, the ^{22}Na distribution of a previously proton-irradiated aluminium disk was measured, which is in great accordance with a reference measurement.

This prototype showed the feasibility of a full-size detector which will decrease measurement time by a factor of 25. The development of this new detector is already in progress.

[1] K. Brenner et al., High-efficiency position resolved gamma ray detectors for 2D-measurements of the angular correlation of annihilation radiation, Meas. Sci. Technol. 36, 075102 (2025)
DOI: 10.1088/1361-6501/adddd9

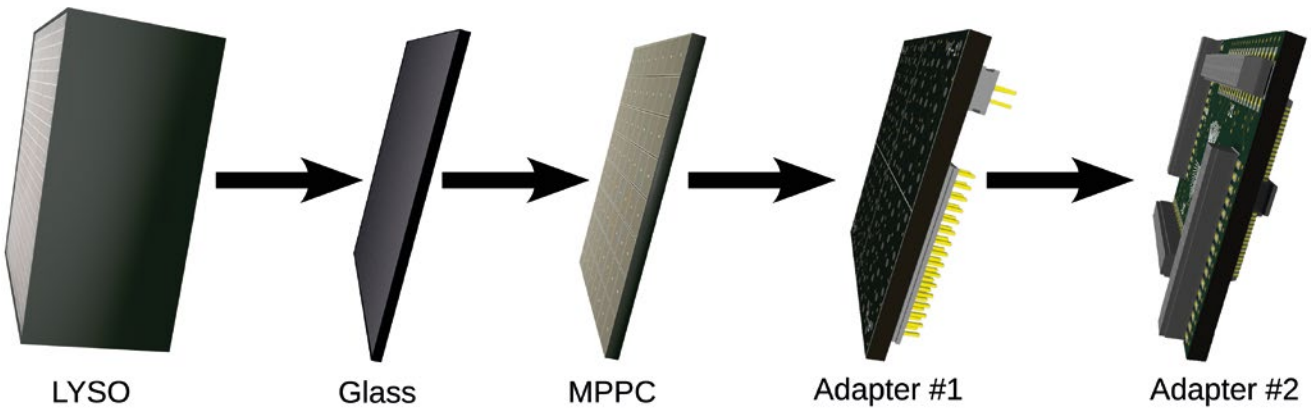

Figure 1: Complete detector stack of a single detector. From left to right: pixelated LYSO scintillator (26.8 mm × 26.8 mm × 20 mm), glass plate (2 mm), energetically and spatially resolved MPPC, two adapters to interface the TOFPET2 readout.

Integrated anti-electronics for positron annihilation spectroscopy

F. Guatieri [1]

[1] Heinz Maier-Leibnitz Zentrum (MLZ), Technical University of Munich, Garching, Germany

In this work, I introduce the design of a microelectronic device employing a 2D array of Zener diodes as an active positron moderator, capable of sculpting positron beams with 6 µm resolution. The re-emitted positrons are accelerated towards the sample through a miniaturised electrostatic lens system and achieve 100 nm resolution. The device also features fast switch-on (90 ps) and switch-off (250 ps) times.

Positron modulating Zeners

Positrons implanted in silicon with a kinetic energy of a few keV thermalise in the material at a depth of a few µm. If electric fields are present inside the silicon crystal, e. g. due to a doping gradient, positrons will also drift in the material. Drift-diffusion phenomena could allow the manipulation of positrons within the silicon bulk of purpose-built microelectronic devices, although no such device has been realised to this day. In this work, the focus is on simulating positron drift-diffusion close to the gradient doping of the p-n junction of a diode, where the intensity of the electric field is capable of inducing a significant positron drift. The change in size of this depletion zone induced by externally polarising the junction allows for a significant modulation of the positron drift (Fig. 1). Through numerical simulation I have designed a device optimised to efficiently modulate the re-emission of positrons implanted into a silicon substrate, which we shall name, for convenience, positron modulating Zener (PMZ). We expect PMZs to achieve a contrast in excess of 70:1, a resurfacing efficiency of 13 % and extremely fast transitions between polarisation states.

Experimental applications

The remainder of the paper presents a case use, supported by robust simulation, for a device consisting of an array of PMZs, namely its use as the last re-moderation stage in a positron annihilation spectroscopy (PAS) apparatus to introduce beam sculpting capabilities. The reduced size of the device eliminates most of the mechanical stability issues experienced by larger microbeam apparatuses. The use of this device would make it possible to alter the imaging resolution during measurement without having to discard previous data. It would allow for faster calibration of the beam optics, and the isolation of non-round features to be measured with high signal-to-noise ratios using PAS techniques. Finally, it opens the possibility of PAS through the use of compressed sensing, which would not otherwise be possible.

[1] F. Guatieri, Integrated anti-electronics for positron annihilation spectroscopy, Sci. Rep. 15, 5934 (2025)
DOI: 10.1038/s41598-025-89630-9

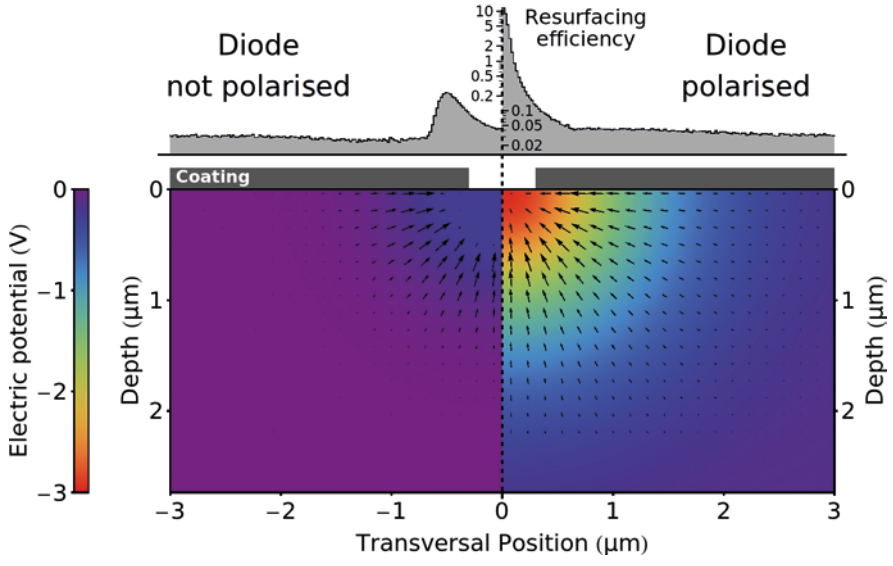

Figure 1: Finite element simulation of the electric potential (colour gradient) and electric field (arrows) inside a PMZ with different states of polarisation. Log-scale histograms (in grey) show the expected re-surfacing of positrons as computed through Monte Carlo simulations. On the left the PMZ is not polarised, on the right the PMZ is reverse-polarised. Positrons re-surfacing on coated areas will not be re-emitted into vacuum.

Sample environment for simultaneous QENS and Raman spectroscopy under controlled humidity and temperature

L. P. Kreuzer[1], M. Wolf[1], F. Ganster[2], C. J. Garvey[1], A. Stephan[1], M. Betker[3], F. Juranyi[4], P. Müller-Buschbaum[2]

[1] Heinz Maier-Leibnitz Zentrum (MLZ), Technical University of Munich, Garching, Germany; [2] Department of Physics, TUM School of Natural Sciences, Technical University of Munich, Garching, Germany; [3] Deutsches Elektronen-Synchrotron DESY, Hamburg, Germany; [4] Paul Scherrer Institute (PSI), Centre for Neutron and Muon Sciences, Villigen, Switzerland

A dedicated sample environment enabling the first simultaneous quasi-elastic neutron scattering and Raman spectroscopy measurements on polymer films under controlled humidity and temperature was developed. The setup allows for stable environmental control and low neutron background. Demonstration experiments on PEDOT:PSS films show how diffusive water dynamics and changes in vibrational modes can be directly correlated in situ.

A multimodal approach to hydration-sensitive soft matter

Understanding hydration-dependent behaviour in soft-matter systems requires simultaneous access to molecular diffusion and local chemical structure. Quasi-elastic neutron scattering probes stochastic diffusive motions on picosecond to nanosecond timescales, while Raman spectroscopy provides complementary insight into vibrational dynamics and functional groups. Combining both techniques under identical environmental conditions enables the direct correlation of diffusion, bonding and structural rearrangements, which is essential for understanding responsive polymer systems.

Design of a dedicated sample environment

A spherical measurement chamber was designed and fabricated by 3D printing from an AlSi10Mg alloy. The chamber integrates thin neutron windows, a Raman window, embedded heating and cooling channels, and a custom gas-flow system (Fig. 1). This facilitates precise control of relative humidity between 3 and 80 % at 25°C and a homogeneous temperature distribution adjustable between 20 and 50°C. The setup provides rapid humidity switching, accommodates large polymer film samples, and exhibits negligible fluctuations in neutron scattering from varying water vapour concentrations.

Demonstration on PEDOT:PSS films

The setup was implemented on the cold-neutron time-of-flight spectrometer FOCUS at PSI. Simultaneous QENS and Raman measurements on 10 µm thick PEDOT:PSS films (poly(3,4-ethylene dioxy-thiophene):poly(styrenesulfonate)) demonstrate the complementary information obtained: QENS resolves hydration-induced water dynamics, while Raman spectroscopy captures corresponding changes in vibrational modes of PEDOT:PSS functional groups. The stable environmental control and low background enable the reliable correlation of diffusive and vibrational processes during humidity and temperature variations.

[1] L. P. Kreuzer et al., Sample environment for simultaneous quasi-elastic neutron scattering and Raman spectroscopy experiments demonstrated on polymer films under changing humidity and temperature, J. Appl. Crystallogr. 58, 2026 (2025)
DOI: 10.1107/S1600576725008519

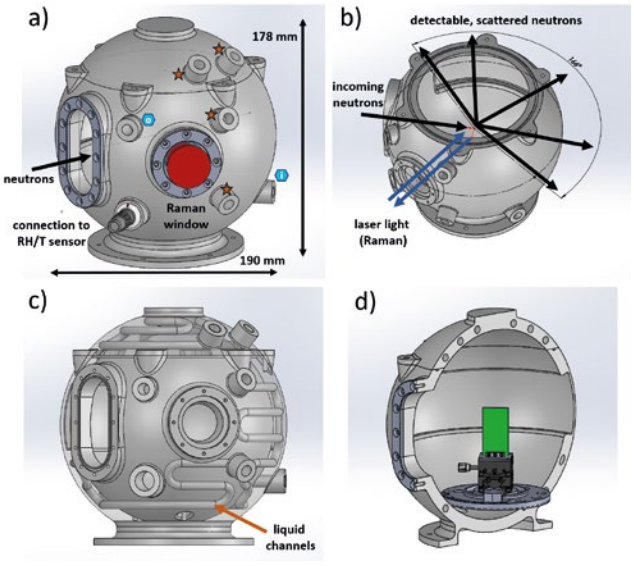

Figure 1: (a – d) Schematic overview of the 3D-printed sample environment. The spherical chamber integrates neutron and Raman windows, embedded heating and cooling channels, and a gas-flow system for precise control of humidity and temperature, allowing correlated in situ studies of diffusion and vibrational dynamics in polymer films.

Depolarisation studies on low-depolarising Cu/Ti and Ni(Mo)/Ti neutron supermirrors

J. M. Gómez-Guzmán[1], K. Bernert[2], A. Devishvili[3], Ch. Klauser[4], B. Märkisch[2], U. Schmidt[5], T. Soldner[3]

[1] Heinz Maier-Leibnitz Zentrum (MLZ), Technical University of Munich, Garching, Germany; [2] Department of Physics, Technical University of Munich, Garching, Germany; [3] Institut Laue-Langevin (ILL), Grenoble, France; [4] Paul Scherrer Institute (PSI), Centre for Neutron and Muon Sciences, Villigen, Switzerland; [5] Physikalisches Institut, Heidelberg University, Heidelberg, Germany

Neutron supermirrors (SMs) are a crucial part of ß-decay experiments, providing important information about the Standard Model of particle physics. Historically, Ni(Mo)/Ti SMs have been used in experiments with polarised neutrons, the accuracy being limited to depolarisation to 10^{-3} per reflection. However, next generation ß-decay experiments, as in the case of the PERC instrument, require SMs that depolarise below 10^{-4} per reflection. Recently, Cu/Ti SMs have been developed.

Neutron mirrors are crucial elements for transporting neutrons from their origin in the neutron source to the experimental site. Due to the neutron optical potential of the composing materials, neutrons that are incident to the surface with an angle smaller than the critical angle θ_{crit} are totally reflected. By stacking multiple layers of neutron reflecting materials with different optical potentials and varying layer thickness, θ_{crit} can be extended. These systems are called supermirrors (SMs) and they are characterised by the so-called *m*-value $m = \theta_{crit,SM} / \theta_{crit,Ni}$, with $\theta_{crit,Ni}$ [°] = 0.099° × λ [Å]. To transport non-polarised neutrons, SMs are usually made of Ni and Ti. However, due to the ferromagnetism of Ni, the reflection of a polarised neutron off a Ni/Ti SM might flip its spin, which depolarises the neutron beam.

Supermirrors for transport of polarised neutrons

The common choice for transporting polarised neutrons is a Ni(Mo) alloy with more than 12 wt% molybdenum. However, a small residual magnetisation remains. To overcome this tiny magnetisation, coatings made of diamagnetic copper have been investigated. Therefore, the depolarisation that a polarised neutron beam suffers after reflection off a Ni(Mo)/Ti and a Cu/Ti SMs was experimentally determined with the Opaque Test Bench (OTB) at the PF1B beamline of the ILL [1].

Depolarisation measurements of Cu/Ti and the Ni(Mo)/Ti SMs

In the OTB setup, two cells filled with polarised ^{3}He are used as polariser (P) and analyser (A). The cells are placed inside so-called magic boxes that provide a homogeneous magnetic field for the polarised ^{3}He and shield from external magnetic fields. Additionally, an adiabatic fast passage spin flipper is installed in each box. The polarisation of the direct beam (AP) and the reflected beam (ASP) off *m* = 2 Cu/Ti and the Ni(Mo)/Ti SMs were measured at a reflection angle θ = 0.73° within a 660 mT magnetic field for 5 Å neutrons wavelength. The depolarisation D of the beam after reflection off either sample was then calculated to be $D_{Cu/Ti} = (1.1 \pm 0.7) \times 10^{-5}$ and $D_{Ni(Mo)/Ti} = (2.0 \pm 0.7) \times 10^{-5}$, confirming that all samples are depolarising well below the target level of 10^{-4}.

[1] J. M. Gomez-Guzman et al., Depolarisation studies on low-depolarising Cu/Ti and Ni(Mo)/Ti neutron supermirrors, Nucl. Instrum. Methods Phys. Res. Sect. A 1080, 170795 (2025)

DOI: 10.1016/j.nima.2025.170795

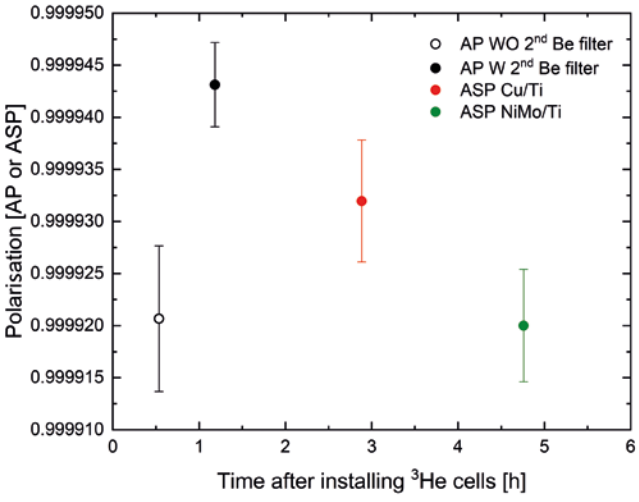

Figure 1: AP at λ = 5 Å with (black dot) and without (open black dot) the Be filter 2 (suppression of neutrons below 4 Å) over time after the installation of the ^{3}He cells. Also shown are ASP of Cu/Ti (red dot) and Ni(Mo)/Ti at θ = 0.73° within a 660 mT magnetic field.

Boron neutron capture enhancement study for radiation therapy with fast fission neutrons

L. Sommer[1], T. Chemnitz[1], A. Alberdi Hidalgo[1,2], J. J. Wilkens[2,3]

[1] Heinz Maier-Leibnitz Zentrum (MLZ), Technical University of Munich, Garching, Germany; [2] Physics Department, TUM School of Natural Sciences, Technical University of Munich, Garching, Germany; [3] Department of Radiation Oncology, TUM School of Medicine and Health and TUM University Hospital, Technical University of Munich, Munich, Germany

While the number of centres offering fast neutron therapy (FNT) for cancer treatment has declined, boron neutron capture therapy (BNCT) is currently experiencing a revival. We investigate the enhancement of dose deposition by boron neutron capture reactions in fission-based fast neutron therapy to explore advanced treatment options in Garching. Two boron-10 concentrations and two neutron spectra are investigated.

The goal in BNCT is targeted irradiation of cancer cells, sparing surrounding healthy tissue. Thereby, the tumour is targeted with B-10 which, upon neutron irradiation, disintegrates into an alpha particle and a lithium nucleus. Both deposit their energy locally in the cell, potentially leading to substantial biological damage. The combination of FNT and BNCT was considered in the past but never became a common approach. This simulation study evaluates the influence of the clinically available B-10 concentration on the physical dose rate in water irradiated with the MEDAPP clinical neutron spectrum.

Potential of boron capture in fast neutron therapy

In contrast to radiotherapy with fast, high-energy neutrons at MEDAPP, BNCT centres commonly utilise thermal/epithermal neutrons due to the high capture cross section of B-10 for low-energy neutrons. As a result of the high hydrogen content in the tissue, fast neutrons are moderated and so a significant thermal component builds up in the irradiated body part. This holds potential for an increased treatment specificity in FNT in case B-10 is present in the tumour. The neutron beam at MEDAPP initially contains a thermal component, and it is filtered out for FNT. In addition to this clinical spectrum, the effect of maintaining the thermal component of the beam was also investigated.

Dose rate enhancement in water and next steps

The calculated physical dose enhancements are shown in Fig. 1. For the combination of the clinical FNT spectrum with the clinically available B-10 concentration of 20 µg per g tissue, a mean dose enhancement of 1 to 2.4 % was calculated. A higher physical dose enhancement was seen for a B-10 concentration of 100 µg/g and the neutron spectrum without the suppression of the thermal component. The results suggest the experimental determination of the biological effect as a next step due to the limitations of our study. Also, higher B-10 concentrations are likely to become available with the development of advanced boron delivery agents.

[1] L. Sommer et al., Boron neutron capture enhancement study for radiation therapy with fast fission neutrons, Appl. Radiat. Isot. 224, 111873 (2025)
DOI: 10.1016/j.apradiso.2025.111873

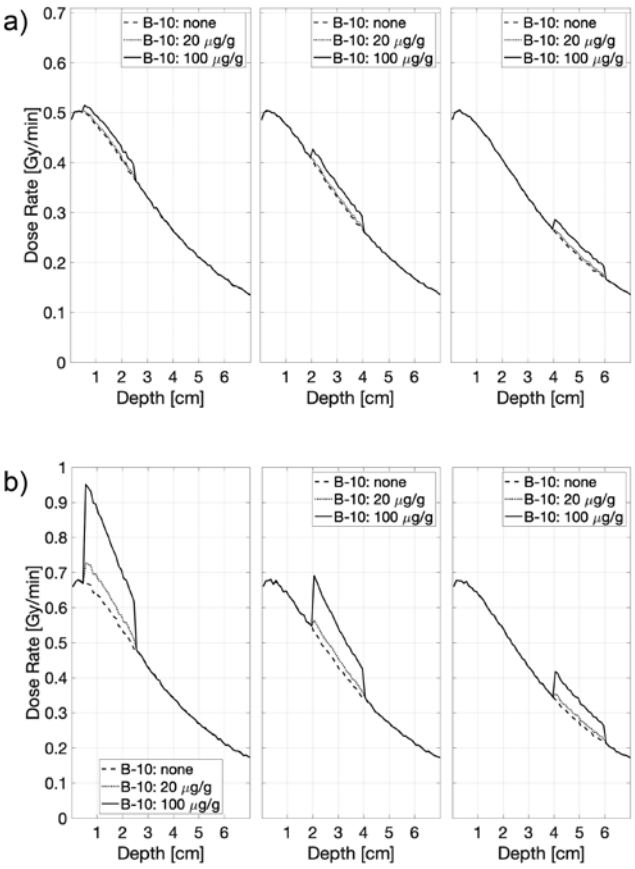

Figure 1: Calculated physical dose rates in water along the beam axis using a cylinder filled with different boron-containing water solutions with a height of 20 mm and diameter of 20 mm located at different depths. Results are given (a) for the clinical fast neutron spectrum at MEDAPP and (b) for the mixed fast-thermal neutron spectrum without the thermal filter.

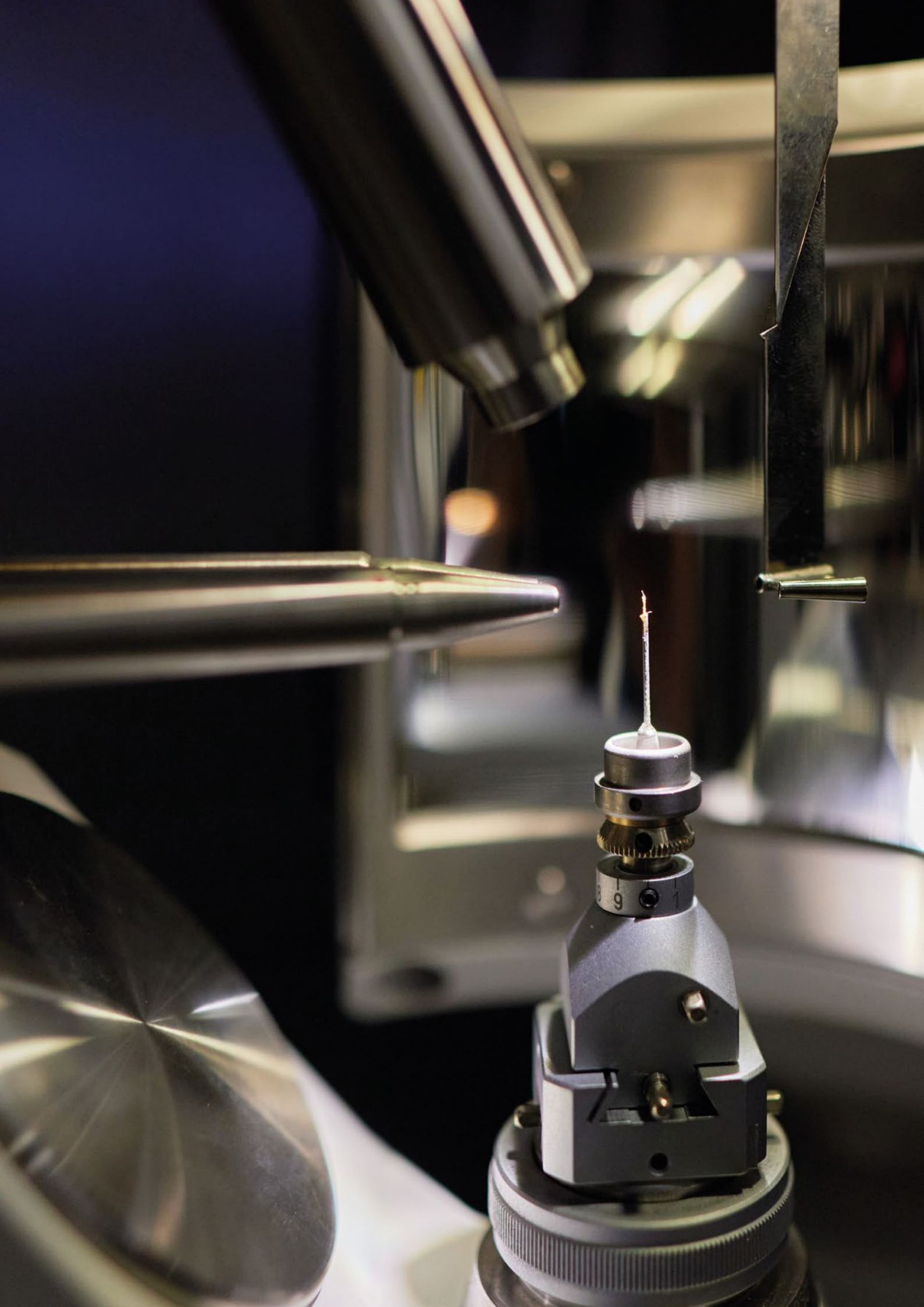

News from the Instruments

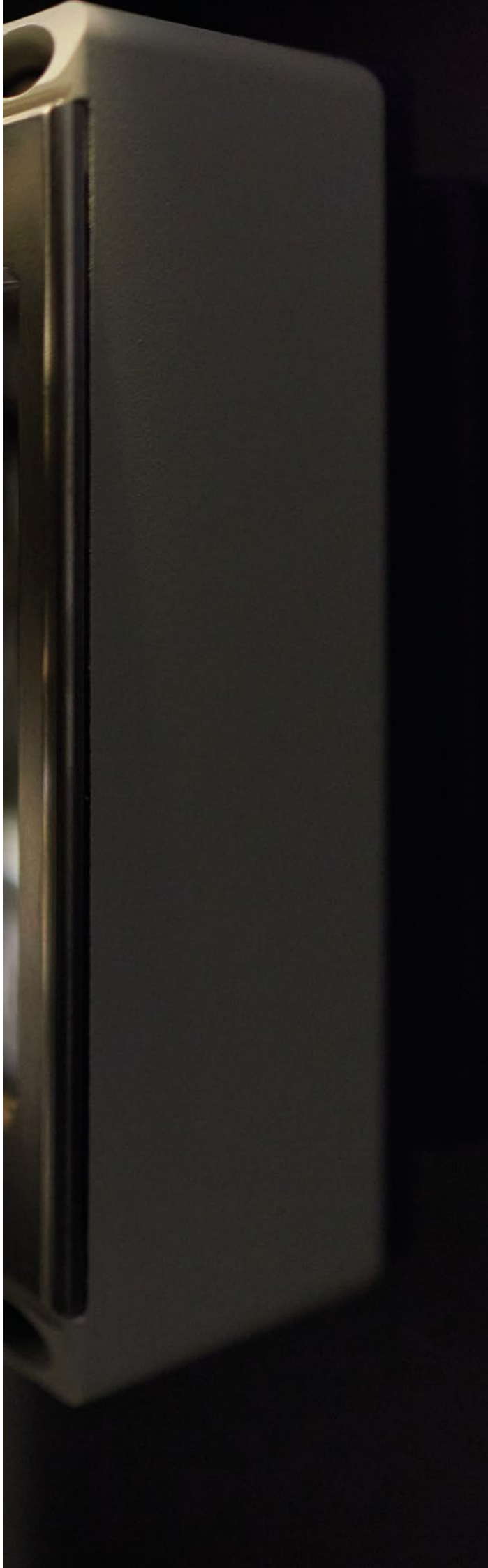

News from the instruments

In 2025, the development of the instrument suite continued with full dedication and great enthusiasm, despite the ongoing reactor outage. Extensive installations were carried out to connect the neutron source with the instruments in the Neutron Guide Hall East. The reinstallation of instruments transferred to the eastern hall, the construction of new ones, as well as the preparations for their commissioning, made good progress. Selected updates on the work carried out on the instruments are presented in this chapter.

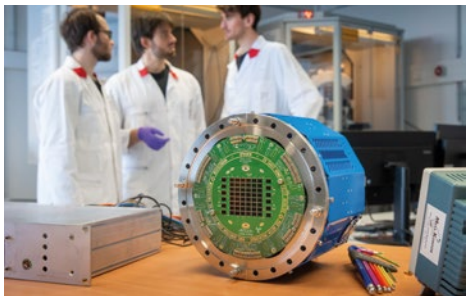

AEgIS@CERN & NEPOMUC

The OPHANIM (Optical PHoton and ANtimatter IMager) detector, developed by the NEPOMUC team, is now operational at the AEgIS experiment at CERN. With 3.85 billion submicron-sized pixels, the detector uses state-of-the-art camera technology to detect antimatter with record spatial resolution. The detector has now collected more than one billion annihilation events, and its sensitivity to visible light has enabled the alignment of the AEgIS deflectometer with nanoradian precision. OPHANIM is now ready for the 2026 measurement campaign at CERN, aimed at detecting the gravitational pull on antihydrogen.

ANTARES

The new polariser and analyser (top) significantly enhance the spatial resolution and polarisation performance of polarised neutron imaging at ANTARES. The polariser, optimised for wavelengths ≥ 2 Å, provides high polarisation with good beam homogeneity. The solid-state bender analyser, with a length of less than 5 cm, reduces the sample-detector distance, thereby improving the spatial resolution. The completed X-ray setup (bottom) featuring a 150 kV source and flat-panel detector, enables simultaneous X-ray and neutron imaging at the instrument.

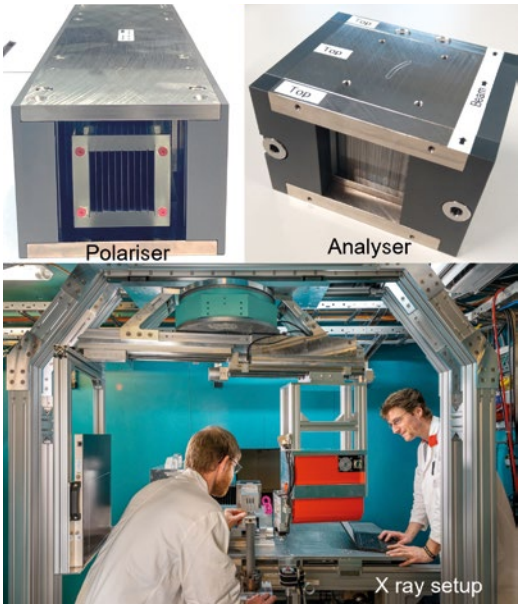

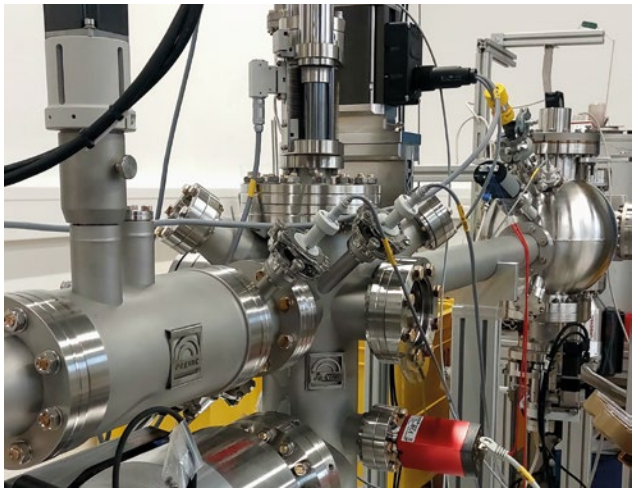

CDBS@NEPOMUC

The coincidence Doppler broadening spectrometer (CDBS) provides the only positron microbeam for the 3D mapping of defects and analysing their chemical composition. We upgraded the CDBS with a spherical sample chamber to eliminate unwanted signals from backscattered positrons. A load-lock system housing twelve samples under UHV conditions enables sample exchange without breaking the vacuum, thereby increasing the effective beam time. Up to now, CDBS was in operation in the Experimental Hall for bulk defect spectroscopy using a β^+ source. At its new position in the Guide Hall East, it will feature the new chamber.

ERWIN

The components of the new diffractometer ERWIN have been further developed. For instance, the accessible scattering angle range of the movable 135° CHARM detector has been increased. More axes have now been fully integrated into the instrument control system, including the base axes of the monochromators and the XY translation table. Progress has also been made in detector readout and data acquisition.

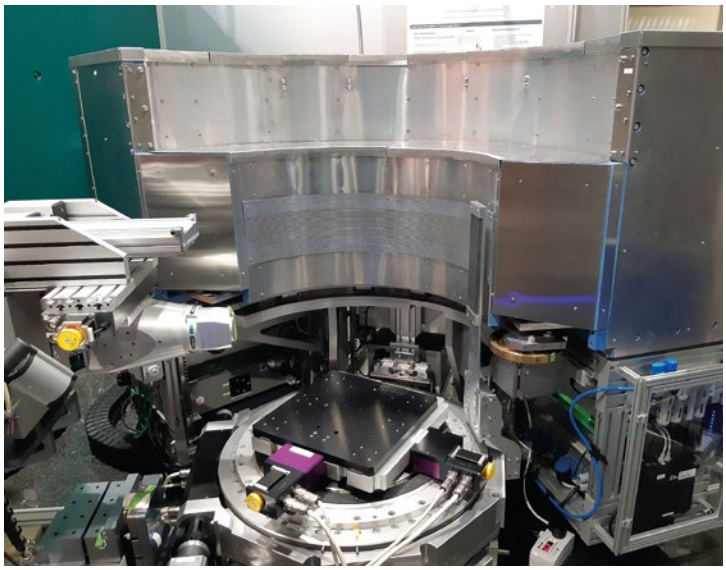

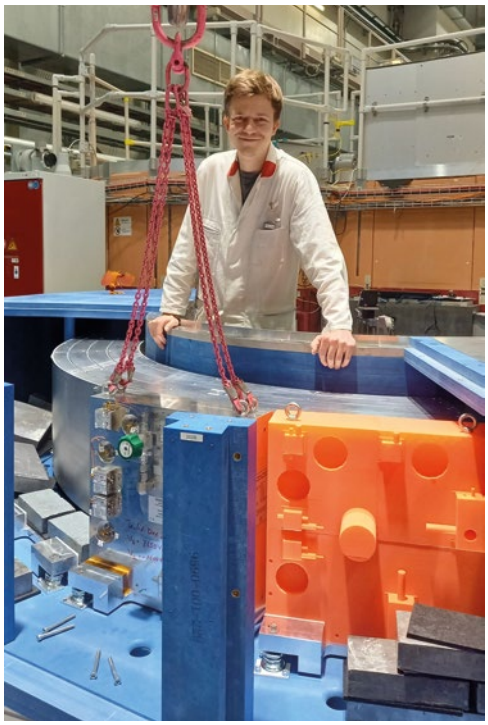

FIREPOD

In 2025, the detector housing of FIREPOD was successfully completed on the experimental field at SR8a. Extensive tests of the major mechanical components working together were carried out in collaboration with the instrument control group to ensure proper operation of the entire setup. Since then, the instrument team and the central FRM II detector group have begun the installation and detailed checks of the array of eight large 2D area detectors – the heart of the instrument.

HEiDi

Preparations for the hot commissioning of the new ^{6}Li scintillator-based area detector with sensitive area of 250 × 150 mm^2 (BMFTR grant 05K19PA2) at the hot single-crystal diffractometer HEiDi continued at full speed, focusing on minor mechanical adaptations and software development (a). In order to ensure access to the most crucial HEiDi sample environment for user operation right after the planned relaunch of FRM II, all HEiDi low-temperature components were maintained, repaired and successfully tested down to 2.5 K (b, c).

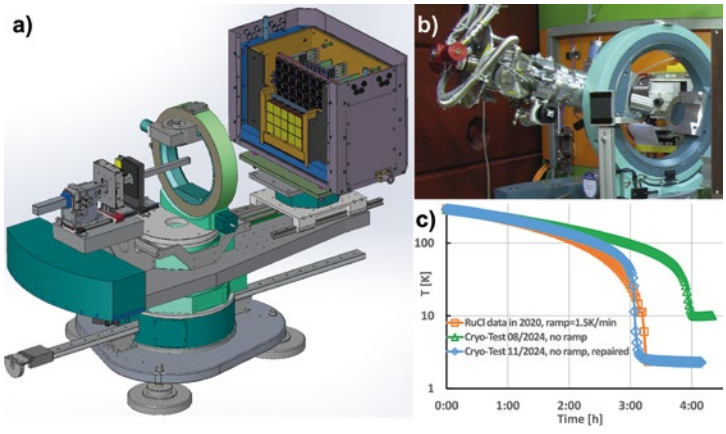

KOMPASS

KOMPASS is preparing for the commissioning and operation of the instrument, now with its full polariser / analyser capabilities. In 2025, the refilling system for the CryoPAD was put into operation, and further improvements on the available Helmholtz coils were implemented. The primary beam path now also features the option of a virtual source (in lieu of the selector) as well as a new collimating superunit directly after the polariser and improved lead shielding after the monochromator.

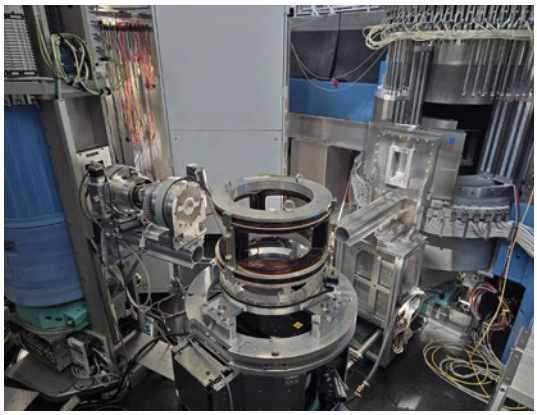

KWS-1

KWS-1 is upgrading its neutron velocity selector and beam stop system to enable user operation without the cold source. The selector will feature a tilting mechanism for shorter-wavelength neutrons at almost the flux maximum the guide delivers without the cold source. In addition, the beam stop system will be equipped with a larger beam stop, allowing for a wider sample slit and thus increasing the neutron flux available on the sample. Both measures will mitigate the loss of cold flux during operation without the cold source.

KWS-2

A new detector, consisting of an array of ^{3}He tubes (6 mm) and fast readout electronics, has been optimised at JCNS for the WANS option at the KWS-2 small-angle diffractometer. By adapting the first segment of the vacuum chamber to a conical nose, the WANS detector will be installed in a fixed, inclined position above the transmitted beam axis at a distance of L_D = 1.25 m after the sample. The detection of scattered neutrons up to an angle of θ_s = 53°, for a Q_{max} = 2.0 Å^{-1}, will be possible both in continuous and TOF mode, in order to bridge atomic to mesoscale structures at KWS-2.

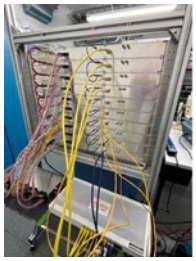

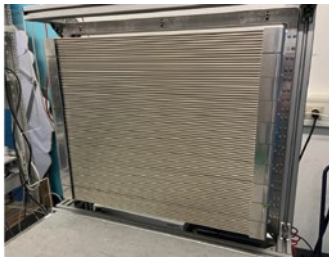

LaDiff

After a prolonged preparation period, the installation of the “dance floor” for LaDiff was finally completed in 2025. This structure provides access to an area of 10 × 7 m^2 equipped with air pads and thus significantly expands the accessible energy and momentum space of LaDiff compared to the former MIRA instrument. Subsequently, the neutron guide NL6 was rebuilt in a modified configuration so that the new LaDiff monochromator is symmetrically aligned with the edges of the aforementioned “dance floor”. The installation of the monochromator shielding, together with the shielding for the NL6 neutron guide, was completed thereafter. In addition, openings for securing the anchor plates of the future steel shielding of LaDiff were prepared in the building’s concrete structure by saw-cutting.

MEDAPP

In 2025, alongside continuous improvements to the multi-leaf collimator, the installation of a detector system consisting of two flat-panel detectors greatly increased the imaging capabilities. Due to the use of different scintillators, the two detectors have complementary sensitivity to photons and neutrons, allowing for multi-modal imaging. The installation is accompanied by the development of an anthropomorphic phantom with sensitivity to neutron interactions similar to that of different tissue types.

MEPHISTO / PERC

The cold beam line MEPHISTO is under construction and will initially provide the neutron decay experiment PERC with ~5×10^{11} neutrons/s. In 2025, the MEPHISTO beam line reached an important milestone with the installation and alignment of the rear section of the neutron guide, including the section through the reactor wall. The picture shows the lower part of the shielding system and the vacuum tube containing the guide. At the PERC instrument, the magnetic field-return was completed, the service platform installed, and its detector systems are being tested. We showed that PERC's internal Cu/Ti guide preserves neutron polarisation at a level below 10^{-4} per bounce (see p. 58), which verifies the required precision.

NECTAR

In the past two years, NECTAR has been rebuilt from the ground up with many upgrades for thermal neutrons. Continuing in these footsteps, NECTAR will further enhance its capabilities for H-quantification and phase mapping via energy-resolved neutron imaging. This will be achieved using a unique and compact chopper design. At its core, the chopper consists of a 120 mm diameter 3D printed boron-containing PLA insert that rotates around its cylindrical axis and contains an array of 684 channels, each measuring $1 \times 1\,mm^2$.

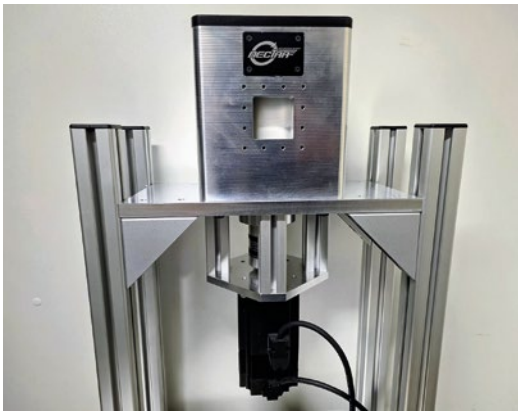

NREX

At NREX, a polarisation analyser with an active area of 200 mm × 200 mm will cover the entire 2D detector. The simultaneous analysis of the specular and diffuse reflectivity reduces measurement time by a factor of 40 compared to the current analyser. The analyser is optimised for operation without a cold source at a wavelength of 2.8 Å. A compact yoke with permanent magnets was optimised using finite-element analysis to provide a uniform field of 700 G. The polarisation efficiency will exceed 99%.

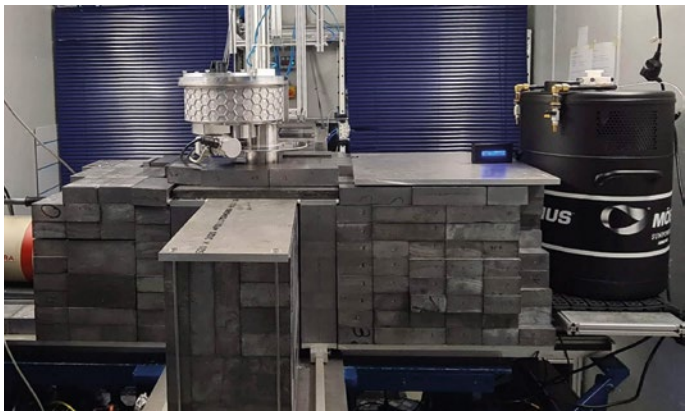

PGAA

After upgrading the detectors at the prompt gamma activation analysis instrument with modern cooling solutions, and equipping the spectrometers with high-resolution capability to acquire Compton-suppressed and normal spectra simultaneously, the instrument shielding was rebuilt so that a new, shorter elliptical guide focuses the neutrons onto the sample position. In addition, a new digitiser was installed to support neutron depth profiling.

POLI

On the hot-neutron single-crystal diffractometer POLI, the spherical neutron polarimetry setup using the new SEOP polariser and analyser is nearing completion for commissioning. In 2025, the construction of two dedicated nutators began, which can rotate the spin polarisation direction away from the initial vertical orientation. Based on magnetic field simulations, a nutator design consisting of rotatable Halbach rings made of permanent magnets was developed. This results in compact and modular nutators that can be combined with the CryoPAD of POLI.

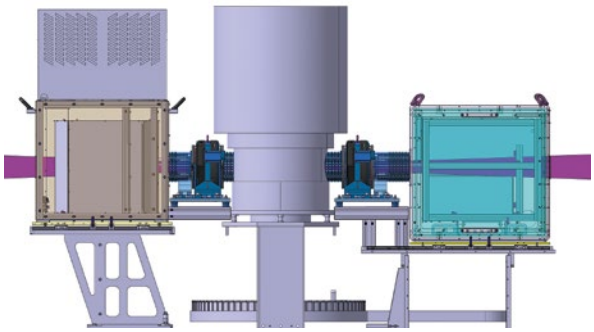

POWTEX

POWTEX's detector chamber in the Guide Hall East was successfully connected to the beam tube of the reactor by installing and precisely aligning neutron guides, choppers and shielding. Detailed planning and cabling work – from the high-voltage power supply to the instrument control – represented a major part of the installations at the secondary instrument. In the context of DAPHNE4NFDI, work was carried out on various aspects of the data workflow for time-of-flight powder diffractometers.

PUMA

The PUMA Virtual Instrument is scheduled to be released as an open-source project next year, prior to the reactor restart. A user-friendly McStas utility enables rapid and convenient simulation of measurements on PUMA, even for new users. It has been successfully featured in TUM student practical courses to provide hands-on experience with simulated neutron scattering experiments, as well as for further planning of PUMA's instrument development, e. g. a velocity selector, shown removing spurious features.

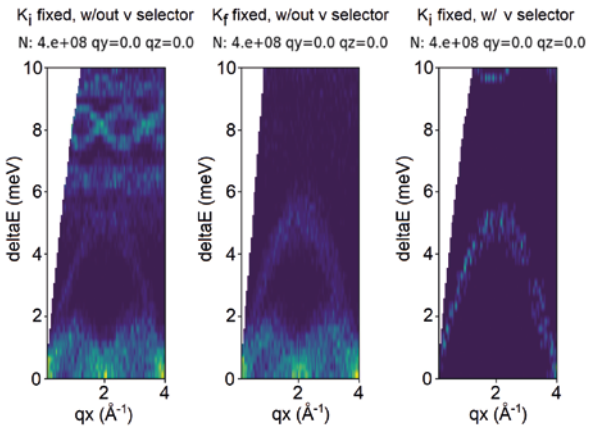

REFSANS

In preparation for the upcoming user operations, upgrades have been completed or are currently underway at REFSANS. The detector has been refurbished with new ^{3}He detection gas and a full set of new wires to enhance its detection efficiency and homogeneity. Attenuators have been installed along the beamline to improve the dynamic range when measuring the primary beam intensity. Finally, and most importantly, work has begun on replacing the primary optics, which will double the usable neutron flux.

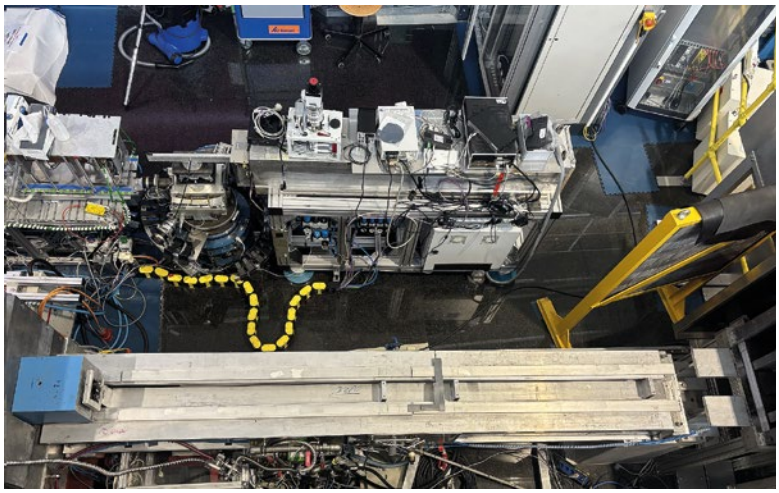

RESEDA

As part of the TIGER upgrade programme, the resonant neutron spin-echo spectrometer RESEDA is being prepared for operation with thermal neutrons. In December 2025, a polarising double-V cavity for thermal neutrons was delivered. The image shows the instrument section that previously housed the polarising cavity for cold neutrons. This space will be used to install a translation system that enables automated and smooth switching between polarising cavities for cold and thermal neutron measurements, thereby ensuring flexible operation across the different experimental configurations supported by RESEDA.

SAPHiR

In 2025, the remaining major components of SAPHiR, such as the chopper and the neutron guide, were installed in the Neutron Guide Hall East. In the picture, two employees of the company S-DH are inserting and micro-adjusting the SAPHiR neutron guide into the vacuum housing, which bridges the 10 m distance from the upstream instrument POWTEX. The guide is composed of glass elements with a supermirror coating with m = 1.5 – 4. These elements are arranged as a double ellipse with focal points at the sample positions of POWTEX and SAPHiR. This configuration creates a narrow beam of thermal neutrons that can enter the sample through the anvil gaps during high-pressure experiments.

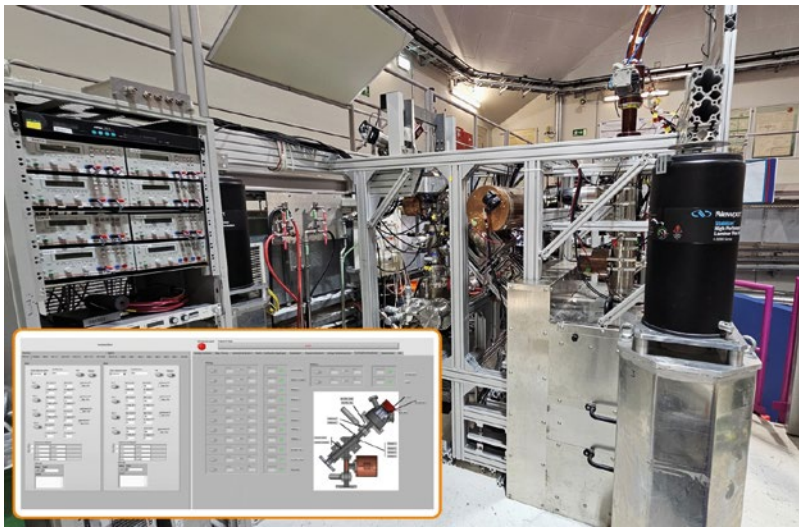

SPM@NEPOMUC

To operate the scanning positron microscope (SPM), current and high-voltage sources are required to deflect, accelerate and focus the positron beam. Operating the instrument involves setting up and controlling more than 100 channels from different devices. The SPM's newly developed control software includes a downhill simplex algorithm that automatically fine-tunes the parameters to optimise the count rate. This reduces both setup and measurement time, increasing the amount of time available for scientific use of the instrument.

SPODI

The high-resolution powder diffractometer SPODI is ready for operation: the relevant instrument components and standard sample environment have been maintained and brought online, and are prepared for user operation. A series of maintenance tasks on the pneumatics and shutter control, as well as adjustments and alignments of instrumental components, has been carried out.

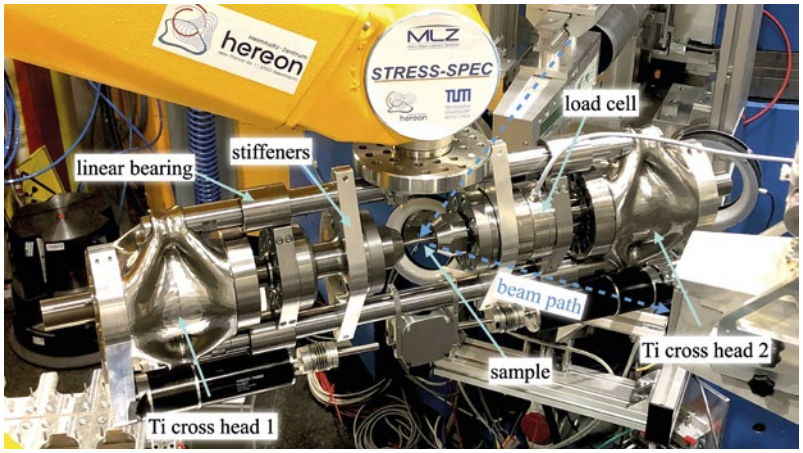

STRESS-SPEC

A compact tension / compression rig with a force capacity of up to 50 kN has been developed to complement the robotic sample handler of STRESS-SPEC. Unlike our existing test rigs, which apply displacement from one side, this rig features two crossheads moving symmetrically from both sides, thus keeping the measurement volume stationary without the need for external position compensation. The compact design, with a total mass of around 30 kg, facilitates mounting on the robot flange without exceeding its payload capacity. This work was funded via the BMFTR project 05K22WO1.

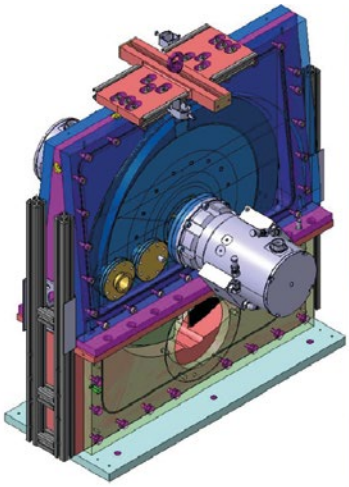

TOFTOF

When the actual chopper system had reached the end of its lifetime, a design study for a new system started last year. This design study was successfully completed this year. Together with new neutron guides, a gain in flux across all wavelengths will be achieved while maintaining the same resolution as the current instrument. For our new humidity chamber, the design of an improved gas flow system has started, while the chamber itself has already been successfully used by users at the PSI.

TOPAS

In 2025, TOPAS saw the installation of its final components. At the heart of the instrument is the chopper cascade (left), with choppers housed in a vacuum, allowing them to spin hundreds of times per second. The first tests were successful, as the choppers were spun up to their nominal resolutions. Thus, the heart of TOPAS was beating for the first time! TOPAS is also slowly opening its eyes: commissioning of the helium tubes has delivered the first real detector image (right). So far, we are only detecting cosmic background radiation and electronic noise, but neutrons will follow soon.

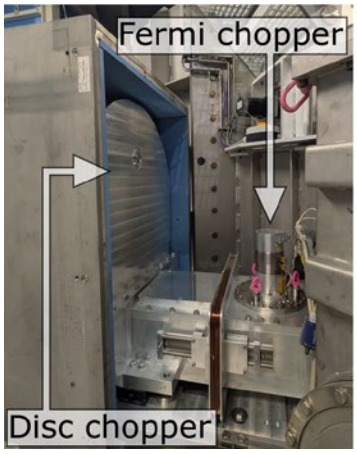

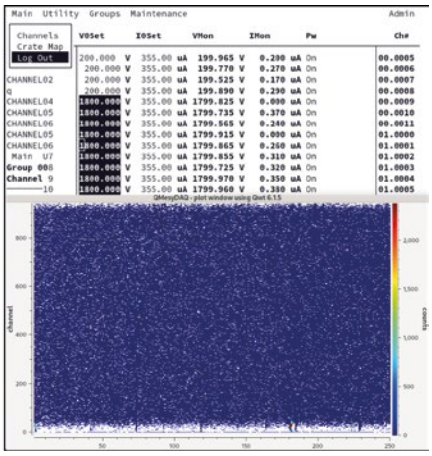

TRISP

The reconstruction of TRISP after its transfer to the Neutron Guide Hall East is almost complete. The installation of the new neutron guide will be finished early in 2026, after which TRISP will become operational. The guide's transmission is optimised by reducing the number of neutron reflections through a geometry that first increases and then compresses the beam width. A cavity polariser in the guide provides a polarised beam in the wavelength range of 1 – 4 Å. Before the reactor start-up, improved spin-flip coils delivering twice the previous resolution will be installed.

News from the Service Groups and Labs

News from the service groups and labs

The advances in the instrument suite described above rely heavily on – and go hand in hand with – the work carried out by the MLZ service groups. Their contributions span a broad range of tasks, from setting up the necessary infrastructure and developing as well as installing brand-new neutron optics components, detectors, and sample environments, to developing and refining software solutions for instrument control, data acquisition, and data processing.

During the shutdown period, it is especially important to maintain a close connection to the user community by offering continuous and versatile support – and this is where the Data Evaluation service group plays a key role. In addition, the MLZ supporting laboratories are preparing for the eagerly awaited return to user operation by expanding their methodological and instrumental capabilities in response to the increasing demands of modern research fields.

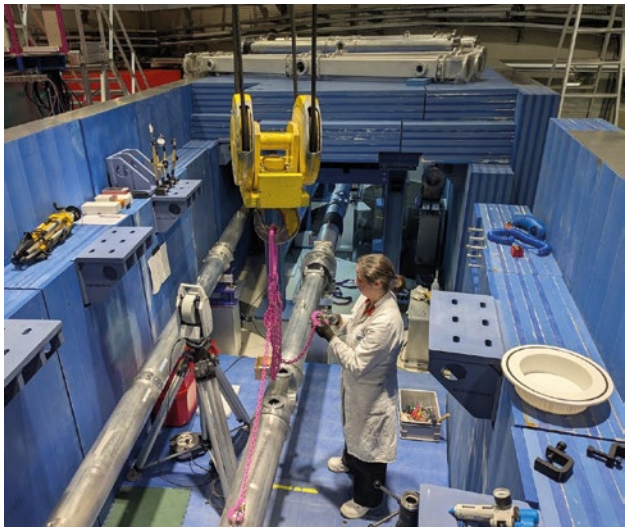

Closing the gap

In the course of 2025, the service groups **Infrastructure Instrumentation, Neutron Optics** and related instrument teams focused their efforts on completing the neutron guide system for the Neutron Guide Hall East, including the vast amount of radiological shielding required for it. The installation of roughly 150 m of neutron guides culminated with closing the last gap in early 2026. Now, neutron beamlines reach the instruments in the Guide Hall East, namely NL-SR4b for MEPHISTO and subsequently PERC, NL-SR5a for the thermal powder diffractometer POWTEX and the extreme environment instrument SAPHiR. NL-SR5m serves the thermal time-of-flight spectrometer TOPAS and NL-SR5b delivers thermal neutrons to the relocated high energy resolution thermal three axis instrument TRISP. The picture shows a colleague installing one of the last vacuum housings of NL-SR5m in the common shielding of the SR5 beamlines in the Experimental Hall.

Neutron supermirror development

Thanks to mechanical stress minimisation, whereby the reflectivity in the coated supermirrors (SMs) is increased, the DC sputtering process has been optimised. That way, the **Neutron Optics group** is now able to provide Ni/Ti SMs up to a coating of $m = 4$. For experiments where polarised neutrons are needed, the group has developed low-depolarising $m = 2$ Cu/Ti SMs. Recent depolarisation measurements excluded depolarisation of a fully polarised neutron beam after a reflection on the Cu/Ti SM in the range of 10^{-4}.

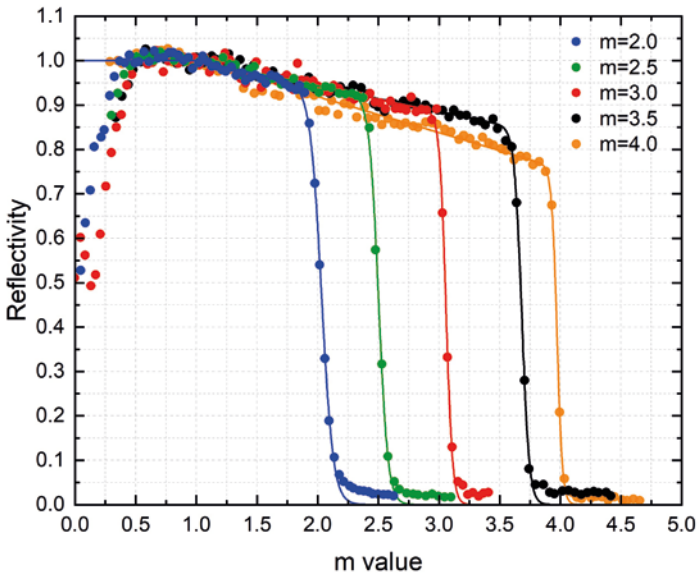

HELIOS: Production of polarised ^{3}He for neutron instrumentation

HELIOS is a MEOP station for the production of polarised ^{3}He gas with a production rate of 1 bar-litre per hour and about 72% polarisation. The improvement in spin-flipper electronics resulted in the building of a unique portable device that integrates an AFP spin-flipper circuit, which serves to flip ^{3}He polarisation, and a power supply for the current generating the static holding magnetic field for the polarised ^{3}He cell. The efficiency of such a device was measured to be larger than F = 0.9999.

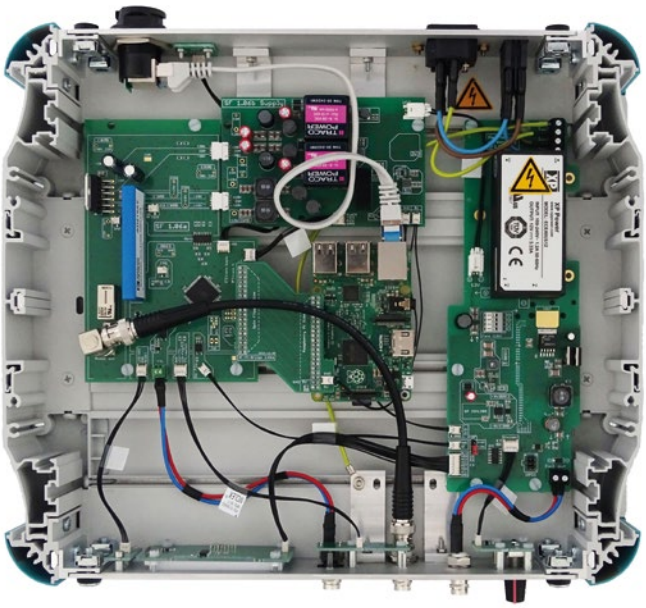

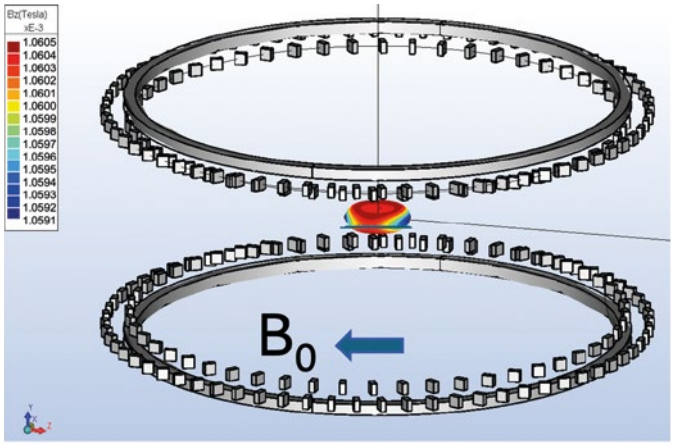

Polariser systems for POLI and TOPAS

The **JCNS ^{3}He group** has been working on polarisation systems for several instruments. In preparation for the restart of the reactor, new systems will be installed for commissioning on POLI and on TOPAS. The POLI polariser system has been designed to be used with the 8 T magnet, and the polariser and analyser are designed for use with the Cryopad option for which new nutators are in production to match the field direction of the new SEOP ^{3}He systems.

For TOPAS a “polariser-cabin” is being prepared in the Neutron Guide Hall East. This cabin is a mini-^{3}He laser lab that will be used to polarise the wide-angle ^{3}He PASTIS analyser cells. Being near the TOPAS instrument, it will allow for optimal transfer of the cells from the polariser cabin to TOPAS for measurements and back for repolarisation.

Finally, we are prototyping ideas for a permanent magnet Halbach-array based PASTIS magnetic environment for TOPAS. We expect first results from the completed prototype system in 2026. As shown in the diagram, “open PASTIS” has two counter-rotating Halbach rings for arbitrary horizonal fields and a Helmholtz coil to obtain the X, Y and Z field directions needed for PASTIS on TOPAS.

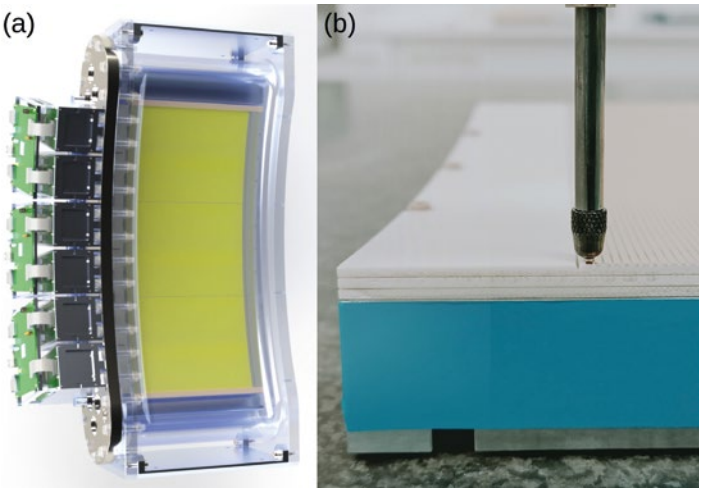

Building NESSI

The construction of a banana detector for STRESS-SPEC has commenced inside the cleanroom of the **Detector group**. (a) The NESSI design comprises curved, multi-wire proportional counter (MWPC) segments mounted seamlessly in a pressure vessel to create a large, homogenous, parallax-free active area. Each MWPC segment is monitored during production, for example using an xyz stage to measure the surface profile with an accuracy of a few µm (b). Segment production will continue through the first half of 2026.

Detector testing at TREFF

The detector test arm at TREFF is an essential tool for the development and characterisation of detector systems and associated readout electronics. During 2025, the test arm underwent a major upgrade, enabling measurements to be performed fully automatically, maximising the efficiency and reproducibility of beam-time usage. Typical tests include absolute efficiency, spatial homogeneity, position resolution, linearity of position response, and localised and global count-rate capability.

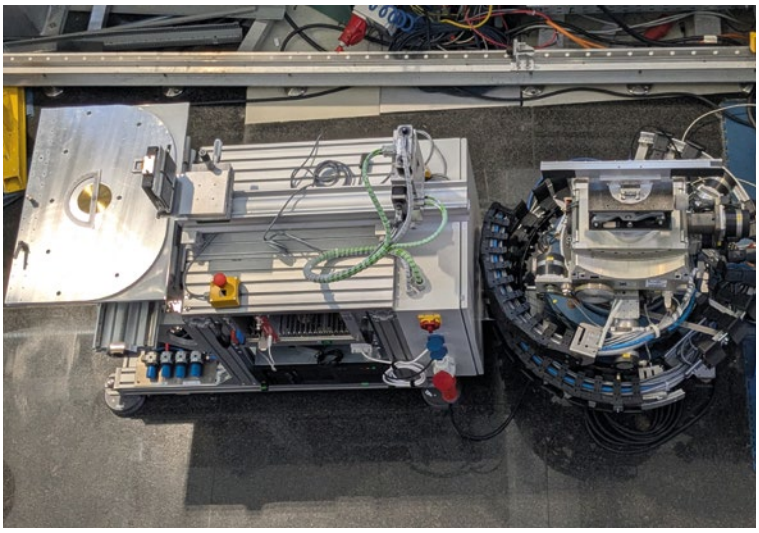

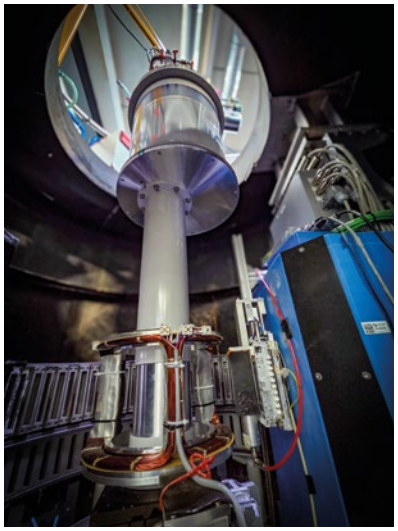

New cryostat for DNS

To deal with the numerous requests for temperatures below 4 K and 200 mK at the instrument DNS, the **Sample Environment group** has installed a dry cryostat with a third stage. This third stage provides liquid helium. Thus, the otherwise dry running cryostat is operated like a classical wet cryostat, and by pumping on the liquid He reservoir, temperatures down to 1.3 K can be achieved. Moreover, a dedicated dilution insert enables the users to measure at temperatures as low as to 20 mK.

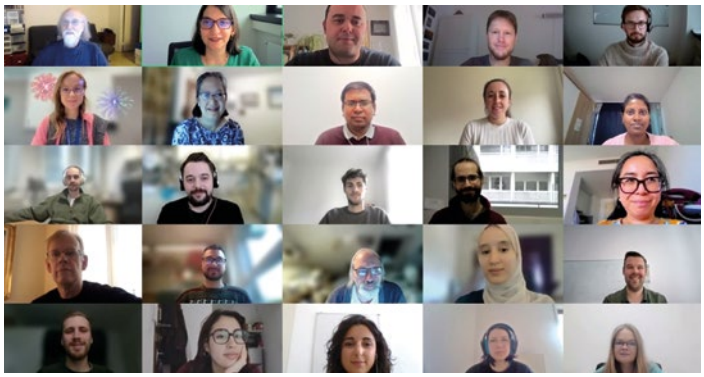

Data analysis & networking

Of the 41 manuscripts supported by **DEVA group** since 2022, 12 were published in 2025. In addition, 4 of the 16 software workshops held by DEVA so far took place this year. The 2-day Machine Learning workshop, co-organised with the **Data Driven Discovery group**, was quickly overbooked, indicating high interest in this field within MLZ. For the first time, DEVA and **Neutron Methods group** co-organised a 2-day online software workshop with SASView developers as well as a week-long contributor camp, where researchers from all over the world participated.

External collaborations in DEVA group

One of DEVA's members has a new role as deputy chair of the Big Data Analytics topic group, which enhances cooperation on digital transformation in the ErUM Data community. The collaboration with ILL progressed, this time as part of a joint PhD project supported by the European Next-Step programme, NS25-ILL17. Progress within the Neutron Quality Label (NQL) also continued – see below for more details. In the picture, PhD student Laura Thackray co-supervised by Dr. Joana Rebelo Kornmeier from the DEVA group presents her poster at the MLZ User Meeting 2025.

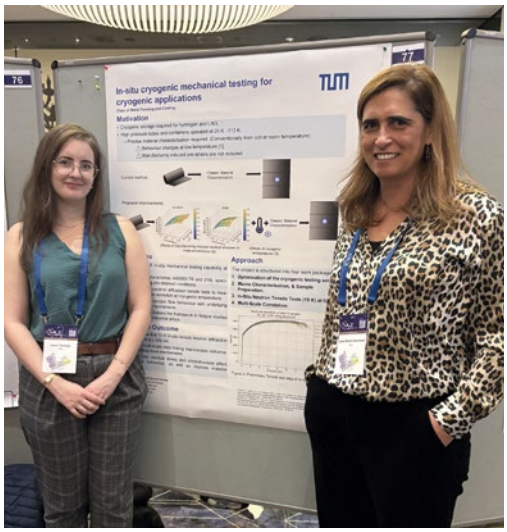

A label for neutron quality

The NQL trademark agreement between ILL and FRM II, which aims to promote neutrons for industry, continues to attract new members. In the previous year, the agreement was signed by ISIS and NECSA. In 2025, two further large research facilities, namely PSI-Paul Scherrer Institute in Switzerland and CSNS-China Spallation Neutron Source in Dongguan, China, showed interest in joining the NQL agreement. The NQL trademark assures the quality process of measurements for strain and stress determination by neutron diffraction. Currently, four strain scanners, STRESS-SPEC at MLZ, SALSA at ILL, ENGIN-X at ISIS and MPISI at NECSA contribute to the NQL trademark by developing a common calibration protocol and a reporting template. The Engineering Material Diffractometer (EMD) at CSNS begins measurements toward joining the framework. **DEVA group** was also involved in these efforts and will play an important role in supporting non-experienced industry users with data analysis.

Scientific software development

AI-supported data analysis pipeline for MARIA

In the **Data Driven Discovery group**, an AI-supported analysis pipeline has been implemented for the neutron reflectometer MARIA within the BMFTR project VIPR. The software allows physical sample parameters to be extracted directly from reflectivity data using state-of-the-art machine learning methods developed together with the University of Tübingen and Helm & Walter IT-Solutions GmbH. In close collaboration with the instrument scientist Dr. Alexandros Koutsioumpas, this tool is being deployed for user operation via both GUI and the command line, providing uncertainty estimates and near real-time parameter inference.

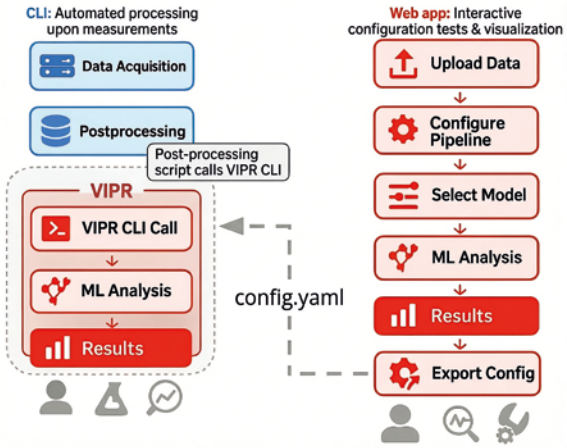

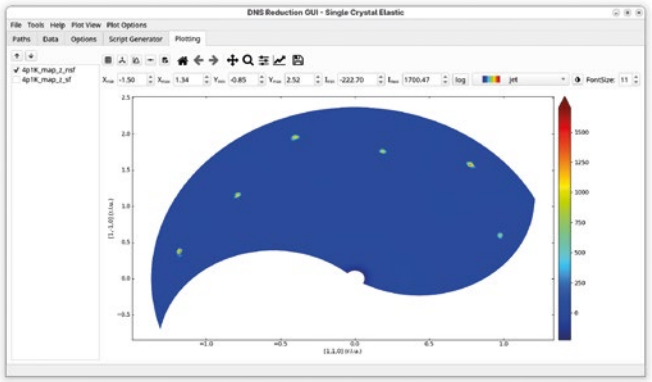

EasyApp and Mantid

In collaboration between the **Data Driven Discovery group** and ESS, an advanced implementation of EasyApp has been integrated into EasyTexture, the data-reduction software for texture measurements at POWTEX, improving the architecture, performance, and flexibility. The Scipp Python library is now a core component of the corresponding workflow prototype. In addition, the migration of the DNS reduction workflow for single-crystal elastic mode into Mantid is largely complete, and users can access the new functionality through a dedicated GUI within Mantid.

BornAgain

Developed by the **Scientific Computing group**, BornAgain is now firmly established as the leading software for simulating and fitting grazing-incidence neutron and X-ray small-angle scattering (GISAS). According to the latest releases, a great deal of effort was invested in internal consolidation and simplification. The software achieved improved stability and functionality with 40% fewer lines of source code. Data structures and plot capabilities were generalised to support off-specular scattering on time-of-flight reflectometers and laid the ground for future support of time-of-flight GISANS. Loaders for various reflectometry formats were added. Extended options for handling the interface roughness have also been added. The figure shows polarised off-specular neutron scattering by magnetic domains in an ion-beam imprinted stripe pattern. (a) Experimental data obtained on D17 at the ILL by Saerbeck et al. (*DOI: 10.3390/nano10040752*), with kind permission. (b) BornAgain simulation.

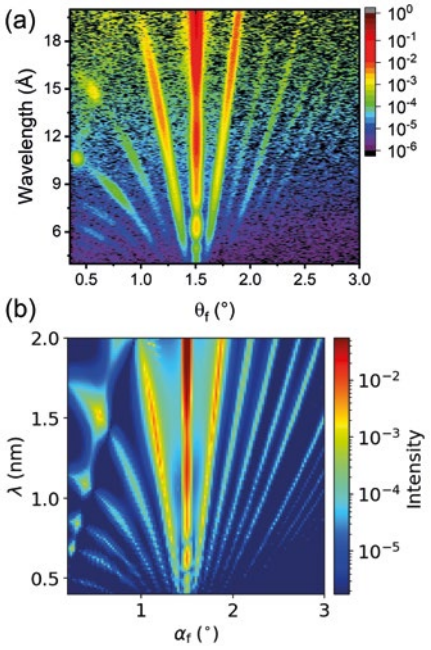

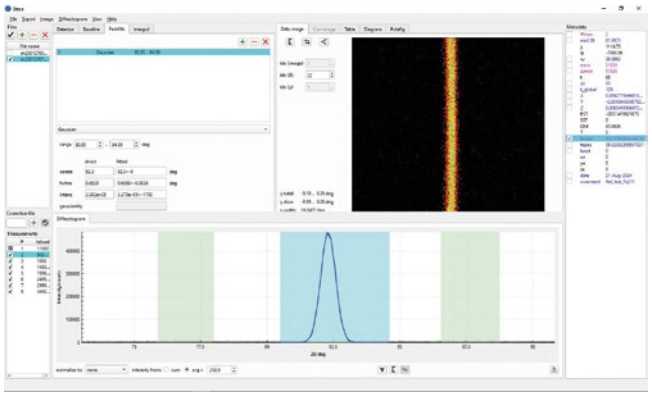

Steca

The stress and texture analyser program Steca is routinely used at the MLZ materials diffractometer STRESS-SPEC. At the request of the STRESS-SPEC team, a number of corrections and functional improvements were implemented by the **Scientific Computing group**. These include: faster and more versatile import of TIFF data; corrected fit error estimates; additional export options; ability to copy plots to clipboard; improved zoom; improved and user-configurable representation of pole figures; improved preservation of software state across sessions.

ReflExplorer

ReflExplorer is the new data reduction program developed by the **Scientific Computing group** for the neutron reflectometer MARIA. It merges functionality from different Fortran and Python programs written by present and former instrument scientists. It was developed in close cooperation with the instrument responsible Alexandros Koutsioumpas (JCNS). A first version was tested against extant data, and is ready to be used routinely following the reactor restart. Practical experience from user operation will then inform the next development cycles. Ultimately, the software will be equipped with a light graphical user interface.

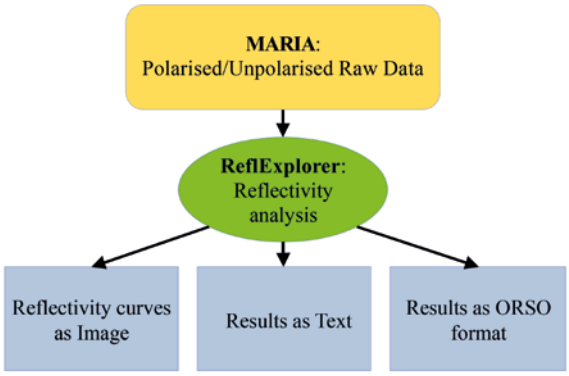

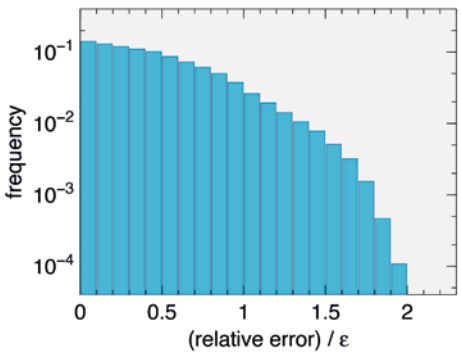

Gaussian membrane model and libcerf

A Gaussian membrane model, developed by Cedric Gommes, has been used successfully in SANS and NSE data analysis. The **Scientific Computing group** re-implemented Gommes' original Matlab code in Python, so that it can be integrated into standard data analysis workflows. Additionally, we are maintainers of the numerical library libcerf, which provides fast and accurate implementation of the complex error function and a number of related functions, among them the Voigt function that is used in both Steca and BornAgain. Occasional numerical instabilities in parameter conversions in Steca induced us to add a special function hwhm_voigt that computes the half width of the Voigt profile using asymptotic series expansions and Chebyshev interpolation. The figure shows the histogram of relative deviations between polynomial approximations (as provided by libcerf) and high-precision computation of the half width of the Voigt function.

Development in the supporting laboratories

Ulbricht sphere accounts for light scattered by the sample

It is difficult to determine the concentration of strongly scattering samples using a distinct absorption coefficient of the sample. Light that is scattered by the sample does not reach the detector and is therefore interpreted as being absorbed by the sample. To remedy this, an Ulbricht sphere is now available for users in the **Biology Laboratory**, which fits as an insert into the JASCO V770 UV-visible spectrophotometer. The sample cuvette is placed at the entrance of the sphere, and light scattered by the sample is collected through multiple scattering events inside the sphere. A small detector positioned inside the sphere measures the light. This allows for accurate determination of the fraction of scattered light.

Synthesis of deuterated N-isopropylacrylamide

To enable contrast-matching neutron experiments, the **Deuteration Laboratory** has established an efficient procedure for the synthesis of partially and fully deuterated N-isopropylacrylamide, which is the monomer of a widely used thermoresponsive polymer. Gels and films formed from this polymer undergo a conformational change when heated above the lower critical solution temperature of 32°C, which impacts their macroscopic properties such as solubility in water, making them excellent candidates for drug delivery systems.

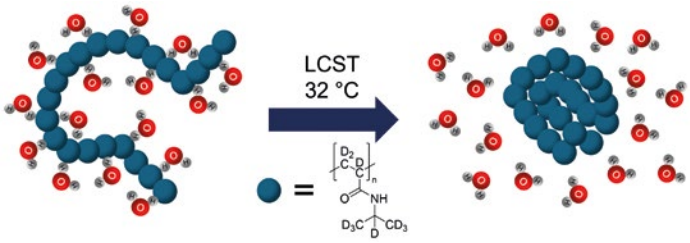

Spin coating option for users

A small SPS Polos 150x™ spin coater has been available in the **Materials Science Laboratory** since 2025. The instrument is suitable for cleaning, drying, coating, developing and etching samples with substrate sizes ranging from a few millimetres to a maximum diameter of 150 mm. The programmable controller allows for complex coating processes with varying speeds and accelerations. The maximum speed is 12,000 rpm (depending on sample size and properties). A special syringe attachment allows up to three different solutions to be added in measured doses. Mechanical sample chucks can be fabricated for samples that are not suitable for vacuum processing.

Developments in the Physics Laboratory and in the Sample Preparation Laboratory

Over the past year, significant progress has been made in both our Physics Lab and our Sample Preparation Lab. In the **Physics Laboratory**, we have successfully implemented the dilution refrigerator option in our Physical Property Measurement System (PPMS) DynaCool 14. This upgrade enables advanced measurements of heat capacity, magnetisation, and electrical resistivity under dilution conditions, significantly expanding our low-temperature experimental capabilities.

In the **Sample Preparation Laboratory**, we have completed a new laboratory space in the Neutron Guide Hall West (see the picture). The facility is now ready for equipping and occupancy, which will begin in the near future.

New options in the X-Ray Laboratory

From 2025 onwards, **KWS-X** has undergone continuous upgrades and optimisation, with the aim of offering an expanding range of sample environments and experimental conditions. As illustrated in the figure, advanced sample environments such as Rheo-SAXS and SEC-SAXS have been successfully implemented. These high-level capabilities are expected to significantly strengthen neutron scattering experiments by providing complementary structural information, and to help future users optimise experimental design prior to neutron beamtime, thereby maximising scientific output.

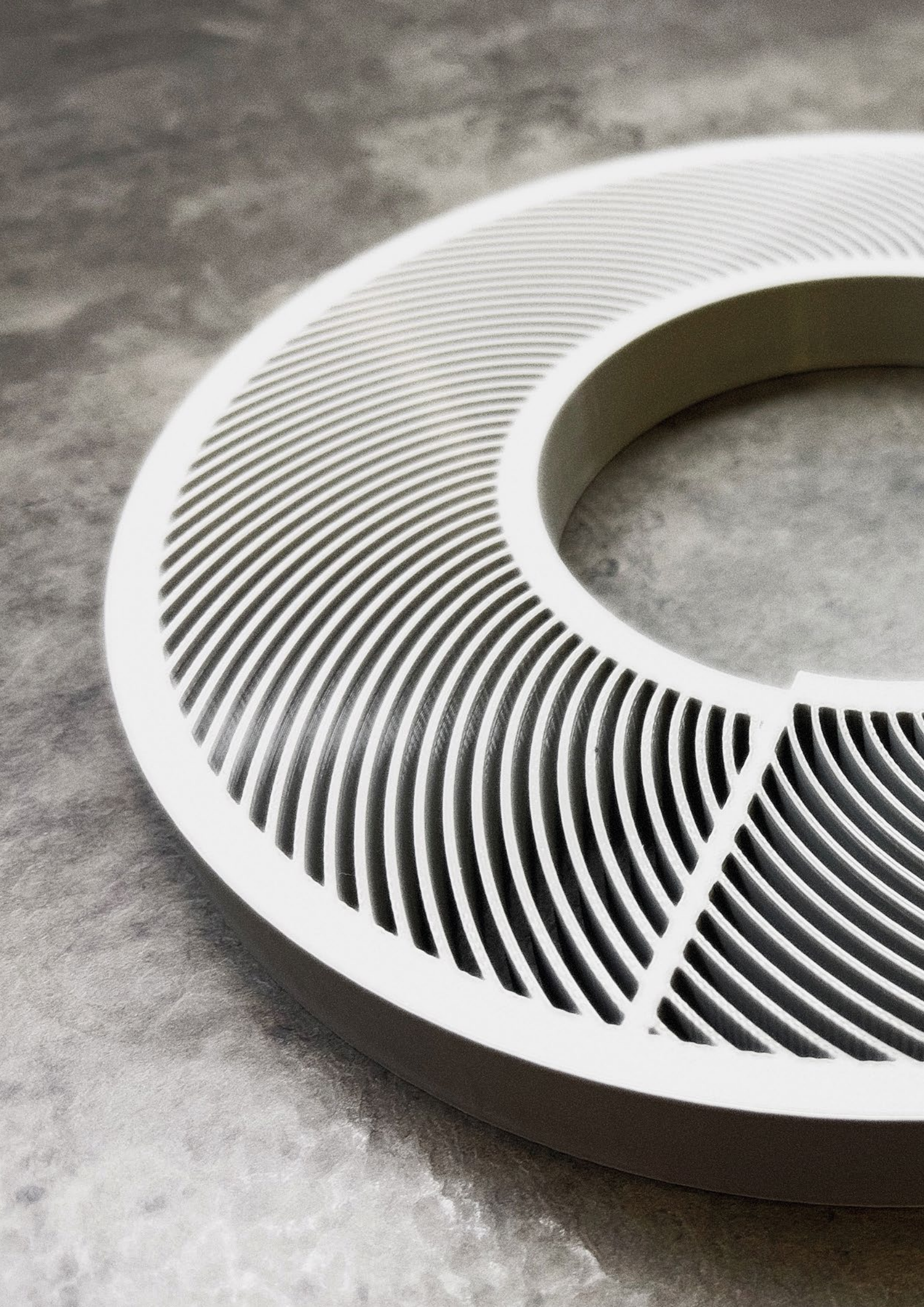

Reactor & Development

Progress towards user operation

A. Pichlmaier, Technical Director

Forschungs-Neutronenquelle Heinz Maier-Leibnitz (FRM II), Technical University of Munich, Garching

Figure 1: First four of the compensators for the central channel close to completion. The picture shows the crew of the manufacturer Witzenmann, second on the right is the FRM II QA responsible B. Pollom. A. Pichlmaier (author of this article) is on the far left.

In 2025, the FRM II remains in the same state – “shut-down operations, fuel unloaded”. However, the hard work of the operational groups towards the restart bears fruit and significant progress has been made. All shut-down operations, inspections and tests were carried out as required by the operating license with only minor deviations.

Despite the lack of reactor power operation, the workload for the operational groups remained high. Their main task continued to be fully compliant with the licensing requirements and safe operation of all systems.

In April, the second Periodic Safety Review – required after 20 years of routine operation – was submitted. Regulatory feedback is still pending.

Progress was made toward fulfilling the conditions of the technical support organisation (TÜV SÜD), particularly regarding the replacement of the UPS and rectifier systems. Seismic qualification remains a demanding aspect. Major components of the tertiary cooling system, including pumps, cooling towers, and water conditioning systems, were refurbished. As for the primary cooling system, several valves were overhauled and the cleaning system was improved.

A key milestone was the successful modernisation of the IC systems of the crane in the reactor hall, followed by approval for moving criticality-relevant loads in November. Modernisation of the three additional safety-relevant cranes also progressed, with the one in the Experimental Hall nearing completion.

Daily operation consisted largely of correcting minor malfunctions typical of complex technical systems. All regulatory reporting was completed on time.

In August, a reportable incident, concerning the temporary unavailability of a tritium measuring station, was reported to the regulator. The event concerned an incomplete switch-over from the main tritium monitoring chain to a spare device, resulting in partial monitoring. There were no consequences for personnel, the facility, or the environment. Reportability was based solely on criteria for safety-relevant components. The technical support organisation’s (TSO’s) preliminary assessment confirmed the FRM II’s evaluation.

The central channel: Progress towards the construction of a vital component

In order to be allowed to build the central channel[1], a number of requirements needs to be met. For example, a double-walled bellows is required to compensate for unavoidable forces like thermal movements, vibrations and others exerted upon the central channel. In July 2025, their manufacture was finally completed (see Fig. 1) and they were shipped to FRM II. This marks a very important milestone towards the construction of the new central channel. In that sense, however, the best news of the year came in December: All the qualification tests were successfully accomplished and all the technical requirements to start production were met. The chances that FRM II will be back into neutron production and fulfilling its mission soon are increasing. However, the central channel has not yet been built. It is not currently on FRM II premises and not yet mounted. Still, we have every reason to be optimistic. Thanks are due to all who contributed to this success and all who stayed, and still stay, faithful to us and supportive of us.

Transport of fresh and spent fuel

On August 25, the federal authority BASE granted the transport and storage licenses for spent FRM II fuel. The license holders are the Bundesgesellschaft für Zwischenlagerung (storage) and Orano NCS (transport). Several objections were filed, as expected, but all were rejected. Legal procedures concerning immediate enforceability are ongoing.

The FRM II intends to ship fuel as soon as both technical and legal conditions allow. The strong commitment of all partners remains crucial for progress.

Manufacturing of the in-pile part of the Cold Neutron Source (CNS)

Many FRM II instruments rely on cold neutrons. Since the CNS failure in 2021, cold neutrons have been unavailable. A new CNS is under construction, and 2025 saw substantial progress: Key documentation was completed and positively evaluated by the TSO, enabling the start of welding qualification tests. These will continue well into 2026 and form the foundation for manufacturing the new in-pile component.

Personnel

Overall, recruitment in the present climate remains challenging. It is hard to attract and to keep qualified personnel, especially where blue-collar positions are concerned. Nevertheless, FRM II was quite successful in some areas: In total five new reactor operators are being trained at the moment with two having their final exam scheduled for early 2026, the others likely in 2027. Overall, more than ten new colleagues have been recruited. A warm welcome to all of them!

Figure 2: FRM II staff are making preparations for the future transport of spent fuel elements. (Picture: A. Eckert)

Conversion of FRM II to low enrichment fuel (from HEU to LEU)

Significant progress was achieved in this strategically essential project. In August, the first irradiation under FRM II conditions of full-size fuel plates – manufactured entirely in Europe by TUM and Framatome / Cerca – was successfully conducted at the BR2 reactor in Mol, Belgium.

On December 22, 2025, the application for the LEU conversion license was submitted to the Bavarian Ministry of the Environment (StMUV), marking a highly visible step forward.

More details can be found in the “conversion” chapter of this report.

Outlook

We are pooling all resources for the planned reactor restart after a long shutdown period and the first shipment of spent fuel to Ahaus (see Fig. 2). The path ahead remains challenging and in some respects unprecedented. Yet, the FRM II team is highly skilled, committed, and optimistic. With joint effort, these ambitious goals are within reach.

[1] For more details on the central channel, see e.g. the 2024 issue of this report.

Updates on conversion: Reaching a milestone

C. Reiter, D. Bonete Wiese, K. Shehu, R. Schönecker, N. Lomp, J. Mercz, T. Schlitt, J. Shi, C. Schwarz, K. Buducan, T. Chemnitz

Forschungs-Neutronenquelle Heinz Maier-Leibnitz (FRM II), Technical University of Munich, Garching, Germany

In 2025, significant progress was achieved in the proposed conversion of the FRM II neutron source to low-enriched uranium (LEU) fuel, combining experimental validation, fuel qualification, and regulatory advancement. Thermal-hydraulic investigations using the "Lucky Loop" experiment at McMaster University provided high-quality benchmark data for the validation of advanced reactor simulation tools. The results demonstrate excellent agreement between experiment and simulation, reducing design uncertainties and strengthening the safety case for the converted reactor.

A major milestone was reached with the successful irradiation of two monolithic uranium-molybdenum (UMo) fuel plates in the BR2 reactor at SCK CEN in Mol, Belgium. The experiments confirm that the high-density fuel concept can withstand the demanding operating conditions of FRM II, providing strong experimental support for the conversion strategy.

Building on these results, the licensing application for the use of LEU fuel was submitted to the Bavarian regulatory authority. This marks the transition into the formal approval process, in which the submitted reports represent the first step of a comprehensive regulatory review. Together, these achievements establish a robust foundation for the safe, efficient, and sustainable long-term operation of FRM II under international non-proliferation standards.

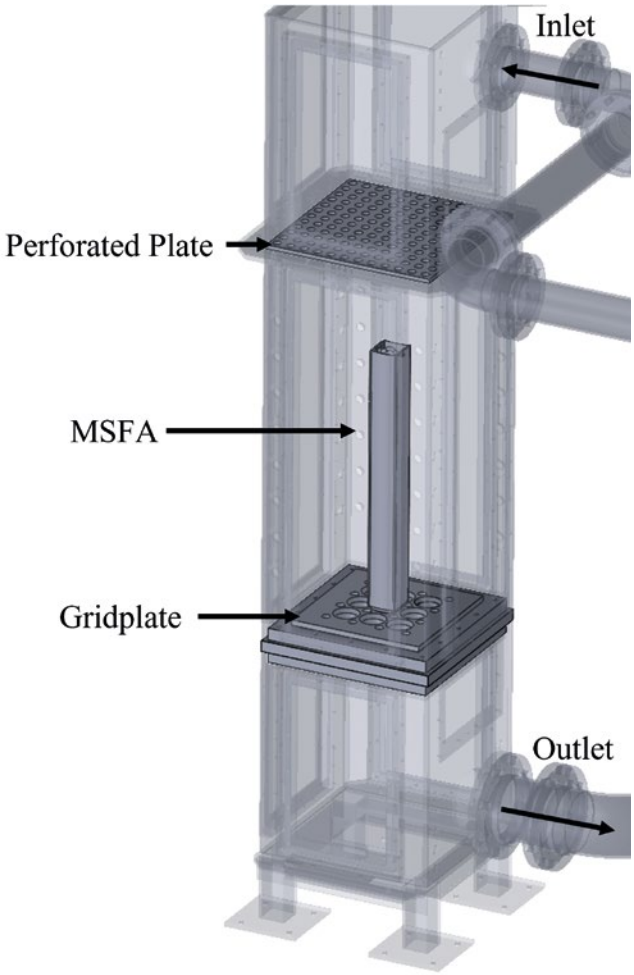

Figure 1: Test section of the TUM flow test experiment at the McMaster University. The sketch shows the gridplate holding a standard MNR fuel element with a perforated plate serving as a flow straightener above.

Validation experiments

The long-term conversion of the FRM II neutron source to LEU fuel is a central strategic objective to ensure both continued high-performance operation and compliance with international non-proliferation standards. A key element of this effort is the rigorous validation of the thermal-hydraulic behaviour of the new fuel design under representative operating conditions. In this context, the "Lucky Loop" experiment at McMaster University in Canada provides high-quality benchmark data for the validation of the modern reactor simulation tools used in the FRM II conversion design.

The dedicated test facility, designed, built, and commissioned by TUM, reproduces the relevant coolant flow conditions expected in future monolithic UMo fuel elements, with particular focus on the flow restrictor. This enables a detailed investigation of key parameters such as pressure drop and flow behaviour. Experiments performed in collaboration with McMaster University show excellent agreement between the measured data and advanced computational fluid dynamics simulations, confirming the reliability of the predictive models used for safety analyses.

By reducing key design uncertainties and strengthening the experimental basis for licensing, these results play a crucial role in defining a robust and conservative safety case for the converted reactor. At the same time, the improved understanding of thermal-hydraulic performance supports the optimisation of the fuel element design for conversion. Together, these endeavors form the foundation for a safe, reliable, and sustainable conversion of FRM II to LEU fuel.

Successful irradiation of test plates

In 2025, a major milestone was achieved in the development of advanced nuclear fuels for research reactors through the long-standing collaboration between TUM and Framatome. For the first time, two UMo fuel plates – fabricated using European manufacturing processes – were successfully irradiated in the BR2 research reactor operated by SCK CEN in Belgium.

The irradiation campaign demonstrated that the high-density fuel system developed can reliably withstand the demanding operating conditions in the FRM II reactor. These results provide strong experimental validation of the ongoing conversion strategy from highly enriched uranium (HEU) to LEU fuel. This achievement represents an important step toward securing the long-term operation of high-performance neutron sources such as FRM II and underlines the critical role of European collaboration in advancing next-generation nuclear fuel technologies.

Submission of licensing documents

Following several years of coordinated effort involving TUM, industrial partners, and European collaborators, the official licensing application for the use of monolithic UMo fuel with an enrichment below 20 % U-235 was submitted to the Bavarian regulatory authority. This submission represents the culmination of an extensive qualification programme combining advanced reactor physics simulations, thermal-hydraulic analyses, and fuel performance modeling with targeted experimental validation, in particular through irradiation testing.

As early as 2022, comprehensive simulation studies identified a feasible fuel element design based on high-density UMo fuel that can maintain the outstanding neutron performance of FRM II while simultaneously meeting stringent safety requirements. Building on this foundation, the conversion scenario has been continuously refined, and with the successful irradiation of the FUTURE-MONO-1 test, the European manufacturing processes have now also been demonstrated under representative operating conditions.

The successful completion of the fuel irradiation tests and the submission of the licensing application represent a decisive step toward ensuring the long-term, sustainable operation of FRM II under internationally accepted non-proliferation standards. At the same time, this marks the beginning of the full regulatory approval process, whereby the three submitted reports constitute only the initial step of a comprehensive and multi-stage review procedure.

Figure 2: Visual inspection of one FUTURE-MONO-1 fuel plate in the BR2 reactor.

Beyond its immediate impact on FRM II, this development contributes to the broader international effort to convert high-performance research reactors to LEU fuels without compromising their scientific output. It highlights the importance of close collaboration between academia, industry, and regulatory bodies, and underscores Europe's leading role in advancing next-generation nuclear fuel technologies for research infrastructures.

Acknowledgement

This work was supported by a combined grant (FRM2427) from the German Federal Ministry of Research, Technology and Space (BMFTR) and the Bavarian State Ministry of Science and the Arts (StMWK).

[1] T. Schlitt, M. Wilson, C. Reiter, Lucky Loop – A Thermal Hydraulic Experiment to Create Data for Validation of Modern Codes; NURETH-21, 31.08.2025 – 05.09.2025, Busan, Korea

Facts & Figures

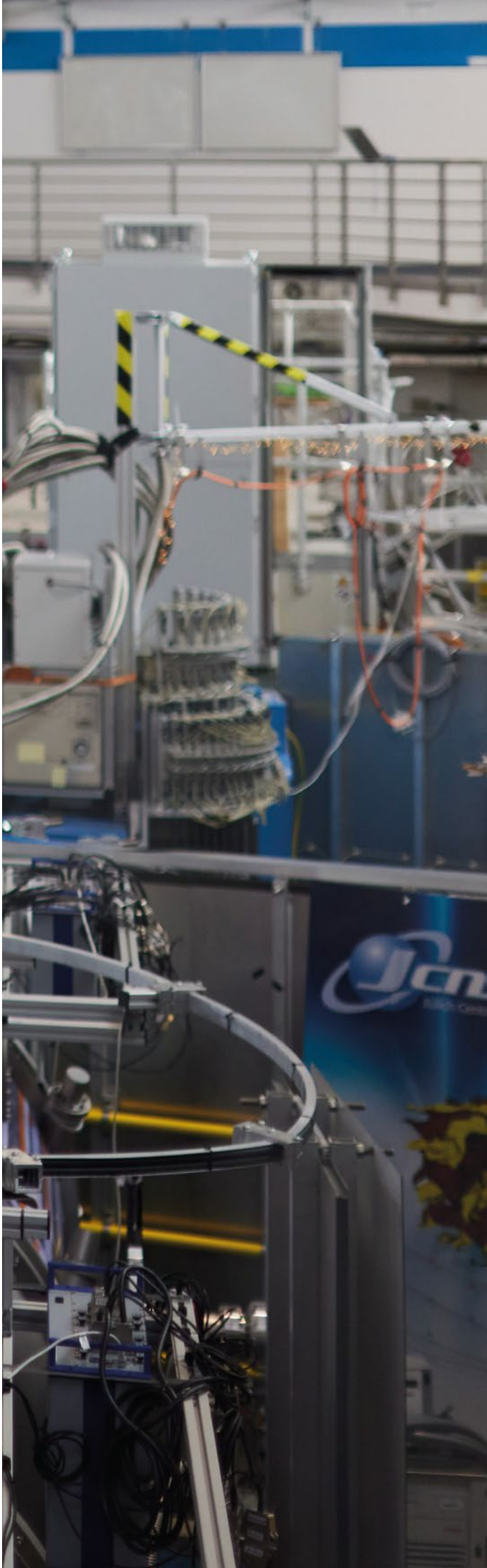

The year in pictures

JANUARY 14th

Kick off meeting EU-Conversion in Brussels: Together with their European colleagues from the EU-CONVERSION and PreP-HALEU projects, Prof. Dr. Pfleiderer and Prof. Dr. Petry from FRM II discuss the upcoming challenges for the conversion and long-term operation of the European high-performance research reactors at the political kick-off event of these projects.

FEBRUARY 19th

Annual winter sports trip: Perfect conditions, fresh snow and great company: around 50 MLZ colleagues gathered in Bayrischzell/Sudelfeld for the annual winter sports trip, enjoying skiing, snowboarding and cross-country skiing while exchanging ideas and connecting across science, operations and administration.

FEBRUARY 26th

Science for everyone: At Deutsches Museum, Dr. Michael Hofmann addressed an audience of around 300, demonstrating how neutron research enables the development of lighter, stronger and more heat-resistant materials, i. e. for automotive applications and gas turbines.

MARCH 13th and OCTOBER 1st

FRM II Welcome Day: New colleagues were warmly welcomed by the directors, before exploring the neutron source on a guided tour. The event offered an up-close look at key instruments and an opportunity to connect, marking the beginning of their journey at FRM II.

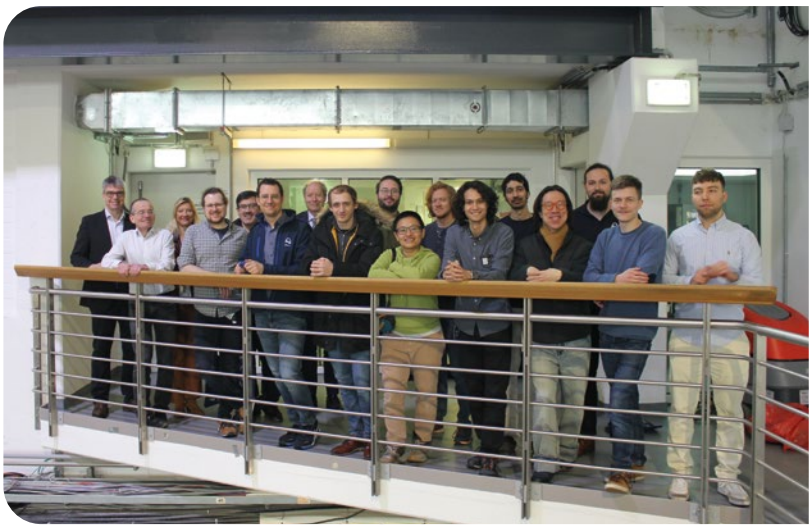

MARCH 16th–21st

DPG Spring Meeting of the Condensed Matter Section: Regensburg University hosted Europe's largest physics congress, drawing 5,000+ scientists and 4,000 contributions. The MLZ User Office featured a booth, engaging students, PhDs, and researchers in discussions.

APRIL 3rd

Girls' Day: On nationwide Girls' Day, 24 girls aged 14–18 visited the MLZ in Garching, where they spent a day as scientists and gained firsthand experience from researchers into the possibilities of neutron research – a hands-on experience shaping future career choices.

APRIL 30th

Long Night of Munich Universities: During the Long Night of Munich Universities, Prof. Dr. Christian Pfleiderer gave his lecture to around 700 attendees, sharing fascinating insights into how neutron research in Garching advances science and benefits society.

MAY 28th and OCTOBER 15th

HOKO Xplore: As part of HOKO Xplore, the hands-on programme of the HOKO – Hochschulkontaktmesse®, students got an exciting behind-the-scenes look. Two FRM II tours gave 29 participants fascinating insights into current research.

JUNE 13th

Visit of TUM benefactors: TUM benefactor Ernst Leinauer visited FRM II with distinguished guests. The programme included a presentation by Prof. Dr. Christian Pfleiderer and Dr. Richard Henkelmann (ITM), followed by a guided tour showcasing research and applications, focusing on cancer treatment with radioisotopes.

JUNE 26th

IKOM: FRM II took part in IKOM, Germany's largest student career fair. Over 200 visitors at the booth explored internships, jobs, and thesis projects, gaining an insightful look into working and collaborating at the institute.

JULY 10th

Little researchers in action! A preschool class from Garching became scientists for a day, guided by Dr. Sebastian Busch, using marker colours to catch a “thief” and solving a 3D-printed atom puzzle. Teamwork and curiosity showed that tomorrow’s researchers are already on their way.

JULY 6th–10th

International Conference on Neutron Scattering (ICNS): A lot of MLZ participants attended the ICNS, hosted jointly in Denmark and Sweden, with 785 participants from around the globe. Each of the four conference days began with thrilling keynotes showcasing the full breadth of neutron scattering.

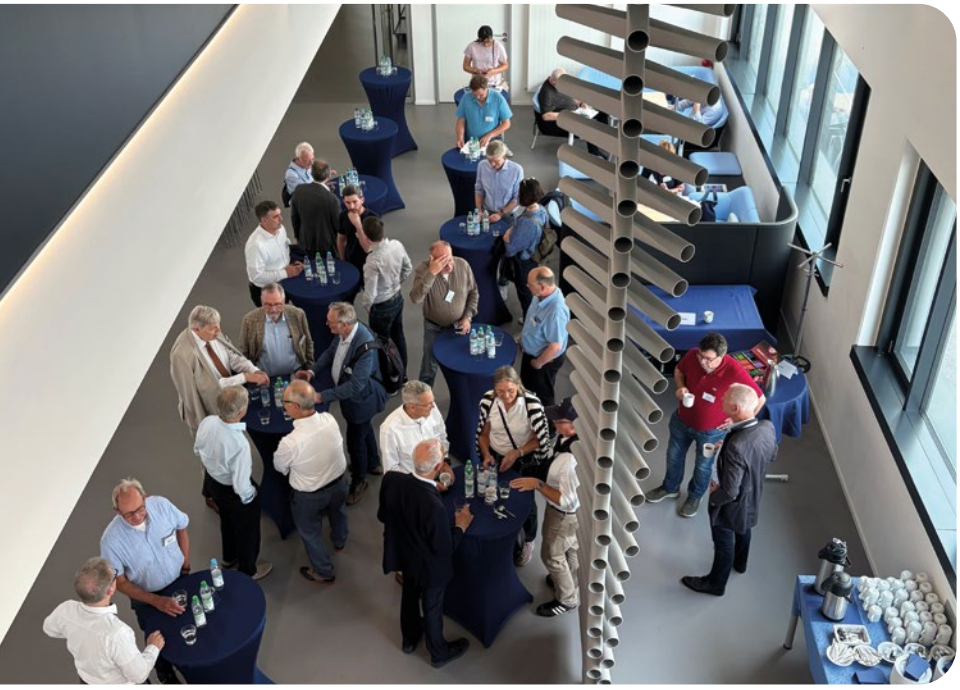

JULY 18th

Freunde der TUM: Fifty guests from the TUM Association of Alumni and Friends visited FRM II. The programme began with a welcome by Prof. Dr. Gerhard Kramer and FRM II directors, followed by guided reactor tours and a small get-together.

AUGUST 6th

TUM Entdeckerinnen: A colourful insight at FRM II, when nine young women joined the “Entdeckerinnen” holiday programme at TUM. From exploring molecules with marshmallows and toothpicks to visiting the control room, they gained hands-on insights into neutron experiments and research.

AUGUST 28th

Little explorers as visitors: A day of science and amazement at FRM II. Visitors from “Nachbarschaftshilfe Garching e. V.” learned about radioactivity and neutrons through a guided reactor tour, Geiger counter measurements, gummy bear molecules, and liquid nitrogen experiments.

SEPTEMBER 19th

Meeting of university research group leaders: MLZ’s scientific and instrumentation projects continue to benefit from close collaboration with universities and Max Planck Institutes. At the annual exchange in Garching, partners discussed key developments, including the new MLZ digital policy and laboratory upgrades.

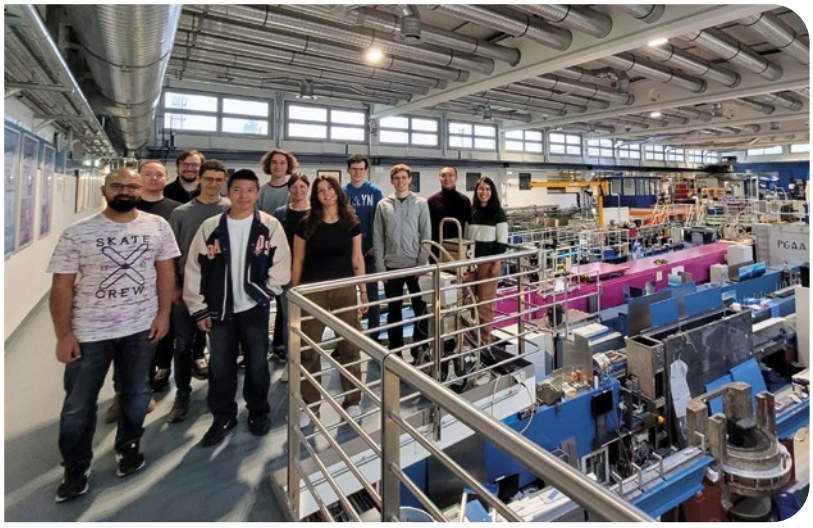

SEPTEMBER 24th

Visit of the Attoworld scientists: Twelve doctoral candidates from the Max Planck Institute of Quantum Optics “Attoworld” visited FRM II, exploring the Reactor and Experimental Halls. They learned how neutrons are produced and applied, from generating positrons for materials research to analyses for the automotive industry.

OCTOBER 3rd

Mouse Day: FRM II opened its doors to around 1,000 visitors, offering guided reactor tours, interactive stands, and conversations with scientists. Tours gave 270 adults and 88 children exciting behind-the-scenes insights into the world of neutron research.

NOVEMBER 4th

Job fair: FRM II took part in HOKO, one of Germany's largest student career fairs with around 15,000 visitors. We met future talents, showcased opportunities from internships to PhDs, and our LEGO model of the reactor captured everyone's attention.

DECEMBER 5th

Political visit: Fifty-seven guests from the "Mittelstandsunion", a CSU working group with entrepreneurs, business owners, homeowners, freelancers, and leading figures in business and government, visited FRM II, featured in a local TV report. Guided tours and insights from Prof. Dr. Christian Reiter and Prof. Dr. Christian Pfleiderer highlighted research and the production of radioisotopes for cancer therapy and diagnostics.

Awards

JANUARY 21st–23rd

Poster Prize at Batterieforum Deutschland: At Batterieforum Deutschland in Berlin, Dr. Neelima Paul won second prize for her poster on understanding ageing in Li-ion batteries with neutrons. The awards were nominated by the Competence Network Lithium-Ion Batteries and the BMFTR Advisory Board for Battery Research Germany.

MARCH 16th–21st

DPG poster prize: Master student Maximilian Suhr from TUM won the Fachverband KFM Poster Prize at the DPG Spring Meeting 2025 for his poster on surface and near-surface positron annihilation with the new SLOPE instrument, recognised for clarity, innovation, and scientific impact.

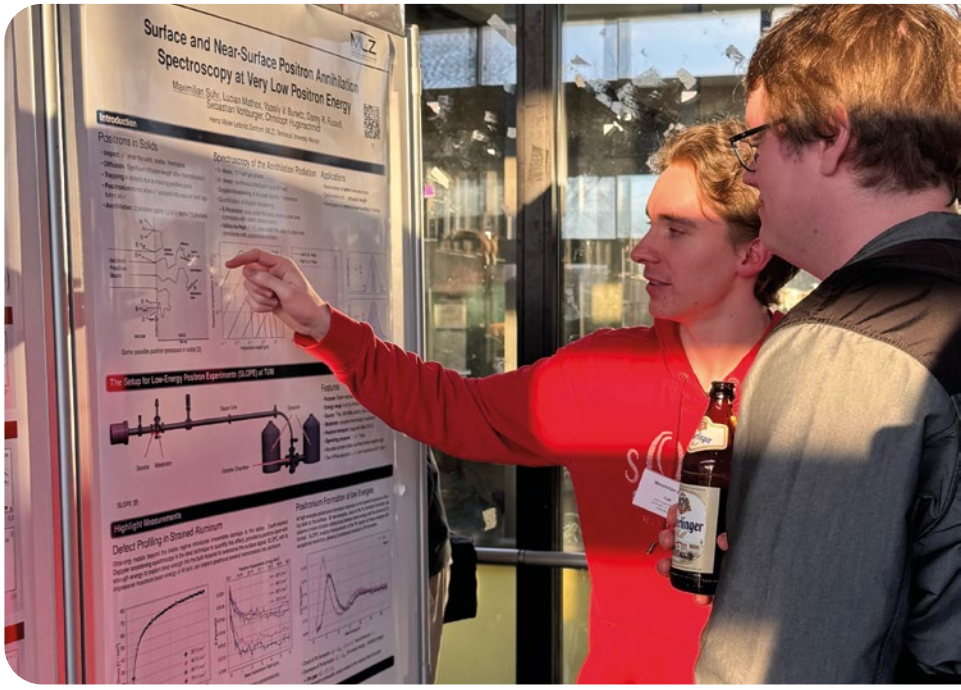

JULY 6th–10th

Poster Prize at the ICNS: Maren Müller, a PhD student at Forschungszentrum Jülich, won the Poster Prize in Soft Matter, Life Sciences and Health at ICNS. She studies leaf proteins as stabilisers in emulsions, using SANS and SAXS to explore plant-based alternatives to animal proteins in food.

SEPTEMBER 11th

Edward Steers Memorial Award: Dr. Ivana Pivarníková received the Edward Steers Memorial Award for her study on lithium distribution in silicon/graphite anodes using GD-OES and Neutron Depth Profiling. The work improves battery analysis, paving the way for safer, more efficient next-generation Li-ion batteries.

NOVEMBER 4th

Heinrich-Büssing Prize: Dr. Leonie Heinze from MLZ was awarded the Heinrich-Büssing Prize for her outstanding doctoral thesis on frustrated magnetic materials. She continues her research at POLI, studying complex magnetic states in naturally occurring minerals.

DECEMBER 5th

MLZ Award 2025: Prof. Dr. Stephan Paul from TUM (m.), with MLZ directors Prof. Dr. Christian Pfleiderer (l.) and Prof. Dr. Martin Müller, received the MLZ Award at the User Meeting. In his talk, he took participants on a journey back to the moments immediately following the Big Bang.

Workshops, Conferences and Schools

January 13th – 17th and May 19th – 23rd:
Advanced Lab Course: Neutron scattering

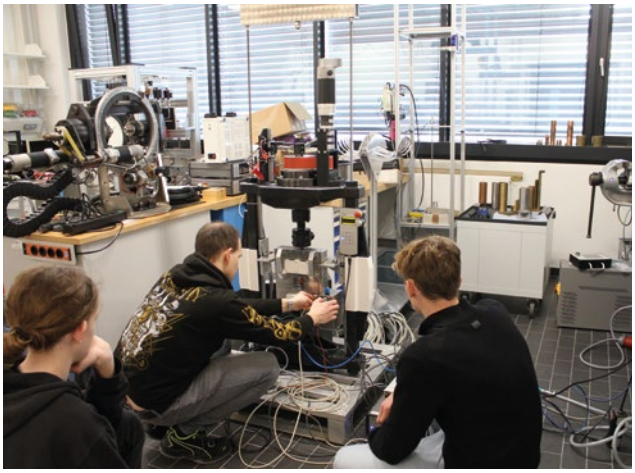

February 24th – 28th: **Student internship**

April 4th: **Training course "Convolutional Multiple Whole Profile Fitting (CMWP)"**

April 24th – 25th: **The annual DGM-SF2M Texture and Anisotropy symposium**

May 21st – 22nd **Machine Learning – Basics workshop**

June 23rd – 26th: **MLZ internal workshop in Grainau 2025**

July 14th – 15th: **Mag2Pol workshop**

July 28th – 31st: **MLZ Conference 2025: Neutrons for Fusion and Nuclear Applications**

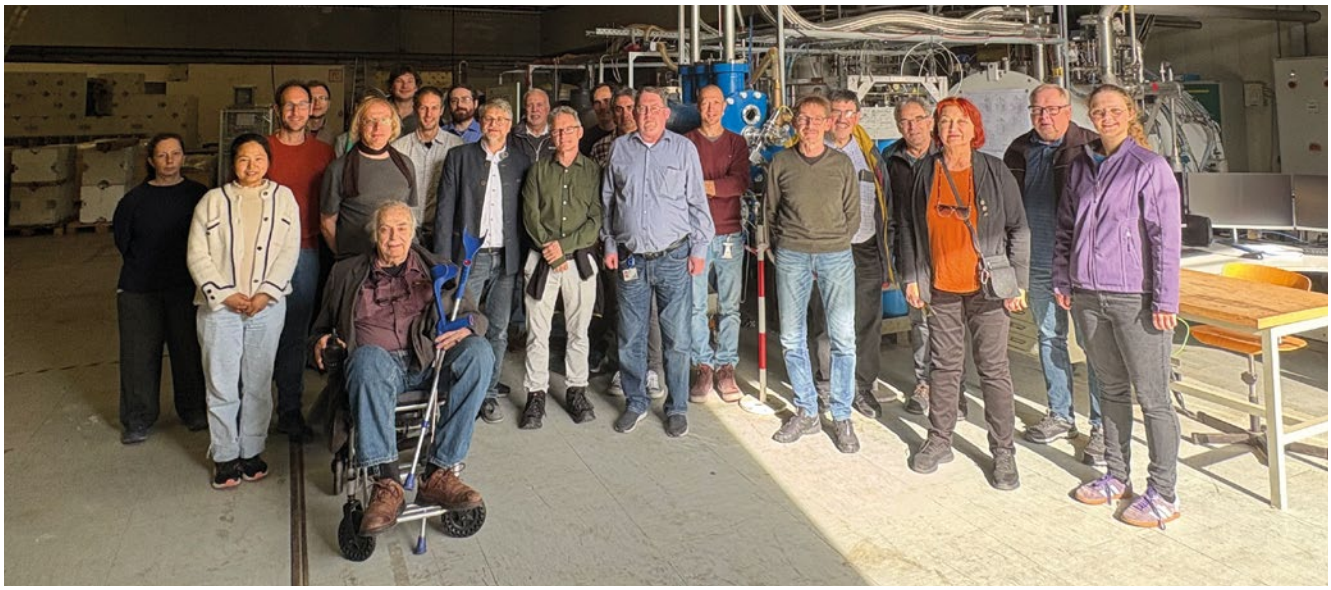

October 8th – 9th: **Workshops: Science with Ultracold Neutrons at the MLZ**

October 6th: **Symposium "A Life Dedicated to Neutron Research" in honour of Prof. Dr. Peter Böni (3rd from r.)**

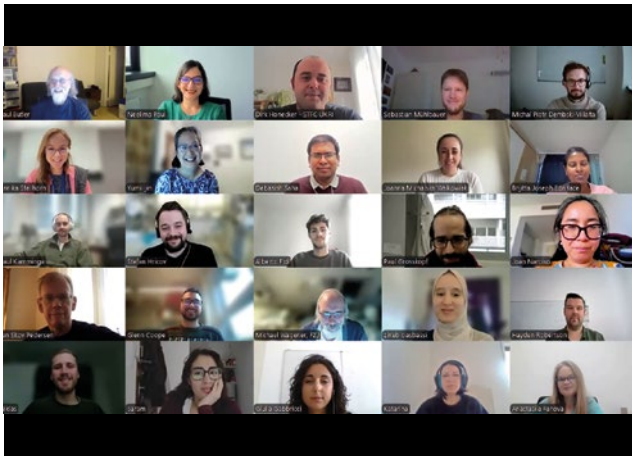

October 23rd–24th: **SASView workshop**

October 20th–22nd: **JANA2020 workshop**

October 27th–31st: **Munich Quantum Matter Days conference**

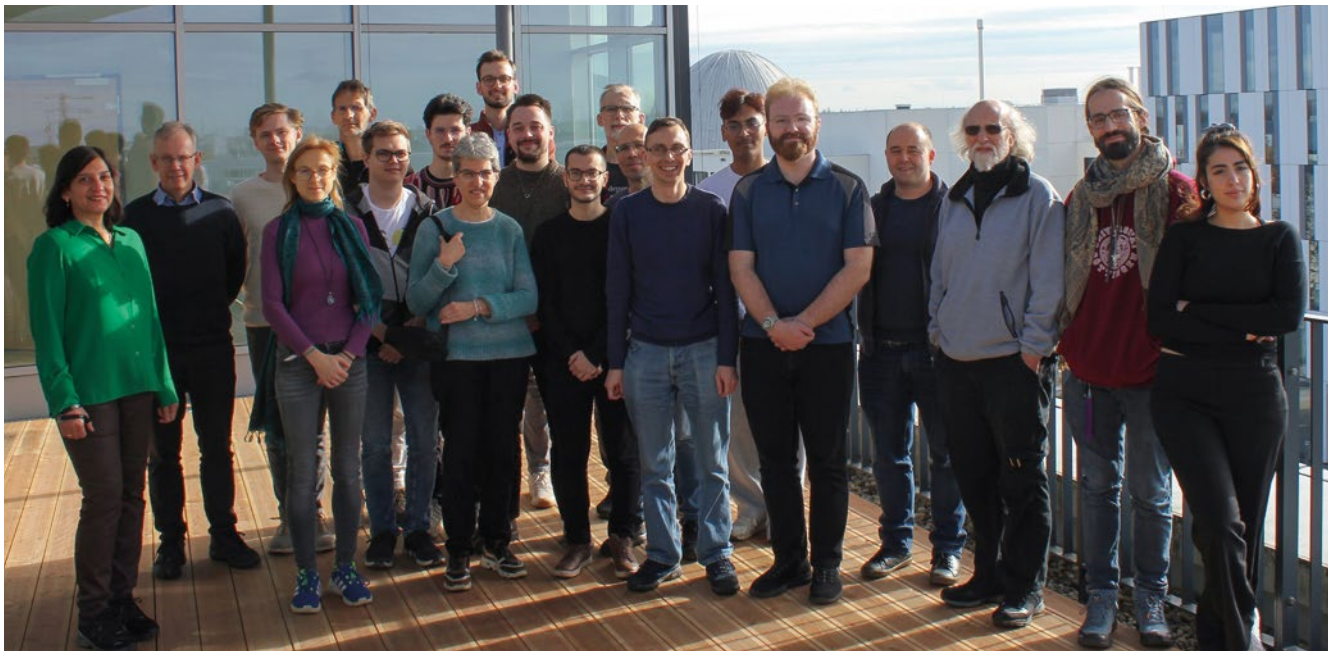

November 11th – 17th: **SasView ContributorCampXIV**

November 25th – 27th: **MLZ/LLB Workshop 2025**

December 2nd: **DEVA-QENS workshop**

December 3rd – 4th: **MLZ User Meeting 2025**

Press & Public Relations

A. Voit, A. Görg, K. Kleinstück, S. Habold, L. Richter

Heinz Maier-Leibnitz Zentrum (MLZ), Technical University of Munich, Garching, Germany

Press and public relations activities at FRM II and MLZ remained resilient and effective in 2025 despite challenging conditions. A temporary understaffing of the press office required careful prioritisation, yet core objectives were achieved: communicating the relevance of neutron research, maintaining strong relationships with media and the scientific community, and ensuring transparency on key developments. Activities spanned press work, digital communication, and a broad portfolio of events and outreach initiatives.

Key achievements in media and press work

Media visibility increased in 2025 to 615 published articles on FRM II and MLZ, marking the highest level in four years. Coverage was strongly shaped by the topic of spent fuel disposal, which accounted for nearly half of all articles. This included public developments such as the protest in front of FRM II on 9 October, where the press office was on site as a contact point for journalists and distributed fact sheets on the planned CASTOR transports.

Press engagement also intensified, with 28 media enquiries and two on-site journalist visits to FRM II.

The press office issued ten press releases in collaboration with partners and published 44 news items across the FRM II and MLZ websites. These results underline the team's ability to maintain a consistent and visible media presence under constrained conditions.

Figure 1: Protest on the planned CASTOR transports in front of FRM II on 9 October.

Media contributions in 2025 by topic area

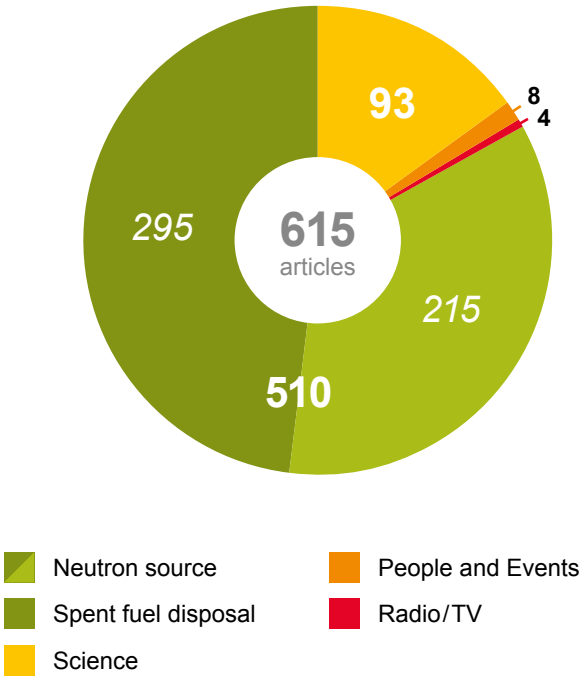

Figure 2: Press articles on FRM II/MLZ 2025 by topic areas.

Growth and new launches

Digital communication in 2025 was characterised by both strong growth and the successful launch of new formats.

LinkedIn consolidated its role as the primary outreach platform. A major milestone was the introduction of the *MLZ at FRM II Insights* newsletter, which gained almost 1,000 subscribers within its first year. In addition, the new LinkedIn channel *Neutronsources* was launched, strengthening international outreach and attracting 622 followers shortly after its introduction. Overall, LinkedIn followers increased by 75 %, supported by active staff participation and multiplier effects.

Instagram further expanded the FRM II's reach among younger audiences through short-form video content, interactive formats, and targeted campaigns such as *Meet our PhDs & Postdocs* and *We need neutrons*. The platform recorded a 57 % increase in followers alongside a significant rise in engagement and content views.

YouTube grew by around 25 % and was increasingly used for livestreams. At the same time, activities on X (formerly Twitter) were strategically discontinued in favour of more effective channels.

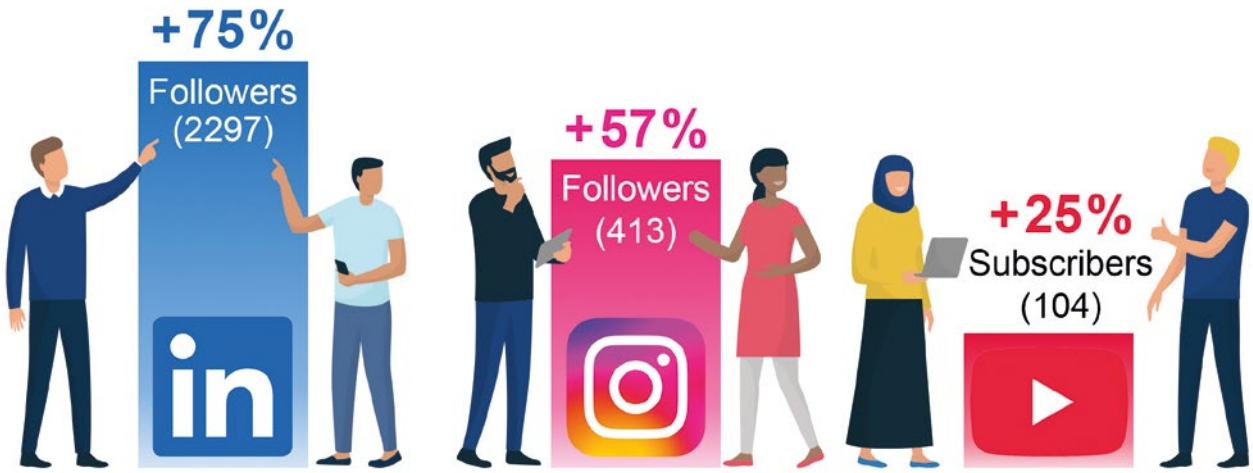

Figure 3: Increasing social media presence

Engagement with the public

Public engagement remained a cornerstone of communication activities. The *Mouse Day* attracted around 1,000 visitors and offered guided tours to 270 adults and 88 children. Interactive exhibits, virtual reality applications, and expert talks enabled direct dialogue and hands-on experiences.

Participation in the Science for Everyone lecture series at the Deutsches Museum was another highlight, reaching around 300 attendees on site and online. The recorded livestream of the lecture “Lighter, stronger, hotter” by Dr. Michael Hofmann meanwhile extended the reach to approximately 7,700 views.

The activities of 2025 demonstrate the continued importance of strategic, targeted communication in strengthening the visibility of FRM II and MLZ. Despite limited resources, the combination of strong media presence, growing digital reach, and impactful public engagement ensured sustained awareness across the scientific community, media landscape, and wider public.

Figure 5: In front of around 180 guests at the Deutsches Museum and a large livestream audience, Dr. Michael Hofmann spoke at “Science for Everyone”.

Figure 4: Mouse Day for all ages on 3 October attracted around 1,000 visitors to the information stands at the Department of Mechanical Engineering at TUM in Garching.

A year of promoting science

T. Burmann[1], I. Köhler[2], I. Lommatzsch[2], R. Schurek[2]

[1] Heinz Maier-Leibnitz Zentrum (MLZ), Technical University of Munich, Garching, Germany;
[2] Jülich Centre for Neutron Science (JCNS-4) at MLZ, Forschungszentrum Jülich GmbH, Garching, Germany

This year, the User Office attended two major events: the International Conference on Neutron Scattering (ICNS) in Copenhagen in July and the redesigned MLZ User Meeting in December. As we still don't have any users, for the most part we helped other groups with their work.

In addition to the annual trip to the DPG Spring Meeting in Regensburg, this year also offered the opportunity to visit Denmark and Sweden. The University of Copenhagen and the European Spallation Source (ESS) invited the community to attend the ICNS. A total of 785 registrants from all over the world gathered at the Bella Center in Copenhagen for three days, before heading to Lund to visit the ESS site.

Figure 1: Booth is constructed at Copenhagen – waiting for visitors.

The MLZ was very well represented, not only by its scientists, who gave many excellent presentations and produced attractive posters, but also as a platinum sponsor. During the breaks, participants gathered at the large MLZ stand in the conference hall. Two special stations were dedicated to

Figure 2: MLZ staff at the ICNS 2025.

Figure 3: So many people!

the supporting labs and the digital twins. Thus, interested visitors were able to gain an insight into each lab by watching the film we produced for this event and meeting lab staff to discuss ideas. Furthermore, there was a hands-on session with two instruments' digital twins during each break. There was also a lot of interest in updates on the FRM II and the ongoing challenges. The MLZ directors gave two talks on this topic, both of which were very well attended – it was quite difficult to find a free seat, and many people had to queue outside the room!

Figure 4: Everybody is interested in the news from MLZ.

On day four, several buses packed with scientists headed across the bridge to the ESS in Lund. Here, the Walter Hälg Prize, the AONSA Prize, and the NSSA Anne Mayes Neutron Scattering Prize were presented. We were delighted to cheer on our colleague Maren Müller (JCNS@MLZ), who received one of five poster awards!

Figure 5: Some details from the MLZ User Meeting.

MLZ Users reloaded

232 MLZ users took up the invitation to the User Meeting in December. Not only did they have to travel to a new venue, they also found themselves in a new setup. Instead of the usual hotel, we moved to a colourful conference centre with a ping pong table! We also said goodbye to the seven parallel workshops on the first day, which meant that we were able to start with a warm welcome from the MLZ directors. They updated the participants on the current status of FRM II in relation to the planned restart, after which they presented the 2025 MLZ award to Prof. Dr. Stephan Paul of TUM. In his awardee talk, he took the participants back to the moments immediately following the Big Bang. In the afternoon, three parallel sessions covered topics such as structural chemistry, hydrogen-metal interactions, and polymers and proteins. In the evening, a traditional Bavarian dinner ensured a good atmosphere and plenty of conversation.

The second day began with two scientific plenary talks. Dr. Hanna Barriga (KTH Stockholm) discussed lipid nanoparticles and their characterisation. The aim is to help design these complex little helpers for drug delivery. Dr. Jasper Landman (University of Wageningen) captivated the audience with his work on the superstructures of pulse proteins.

The second part of the morning session was dedicated to preparations for the restart. Here, different groups presented their approaches. Dr. Manuel Suárez Anzorena (MLZ), head of the Sample Environment group, presented the ongoing equipment tests to ensure the instruments are ready for use. Dr. Anatoliy Senyshyn (MLZ) talked about the diffractometer group and their different approach. While SPODI is a well-known workhorse, ERWIN and FIREPOD will need to be commissioned. Dr. Henrich Frielinghaus (JCNS@MLZ) then described the situation with the SANS machines, which will indeed be affected by the absence of the cold source, and presented ideas on how to manage this situation. Dr. Christian Felder (JCNS@MLZ) concluded the session with a live demonstration of the new data management workflow. This involves automated data acquisition via the NICOS instrument control system, an Electronic Lab Notebook, and the option to download all data. The login and access to this workflow is realised via GhOST, which makes things much more convenient for users!

The User Meeting ended with the traditional poster session. There, it was great to finally have beer again, as the last few didn't offer any. It created a relaxed atmosphere to talk to people and plan future collaborations.

Figure 6: Happy participants at the MLZ Users 2025!

Organisation

FRM II and MLZ

The Research Neutron Source Heinz Maier-Leibnitz (FRM II) provides neutrons for research, industry and medicine and is operated as a Corporate Research Center by the Technical University of Munich (TUM). Scientific use of the FRM II, with around 1,200 user visits in a typical year of operation, is organised within the Heinz Maier-Leibnitz Zentrum (MLZ).

The chart below shows the overall network comprising the Neutron Source FRM II and the MLZ, as well as the funding bodies and the scientific users that perform experiments at the MLZ, addressing the major challenges facing present-day society.

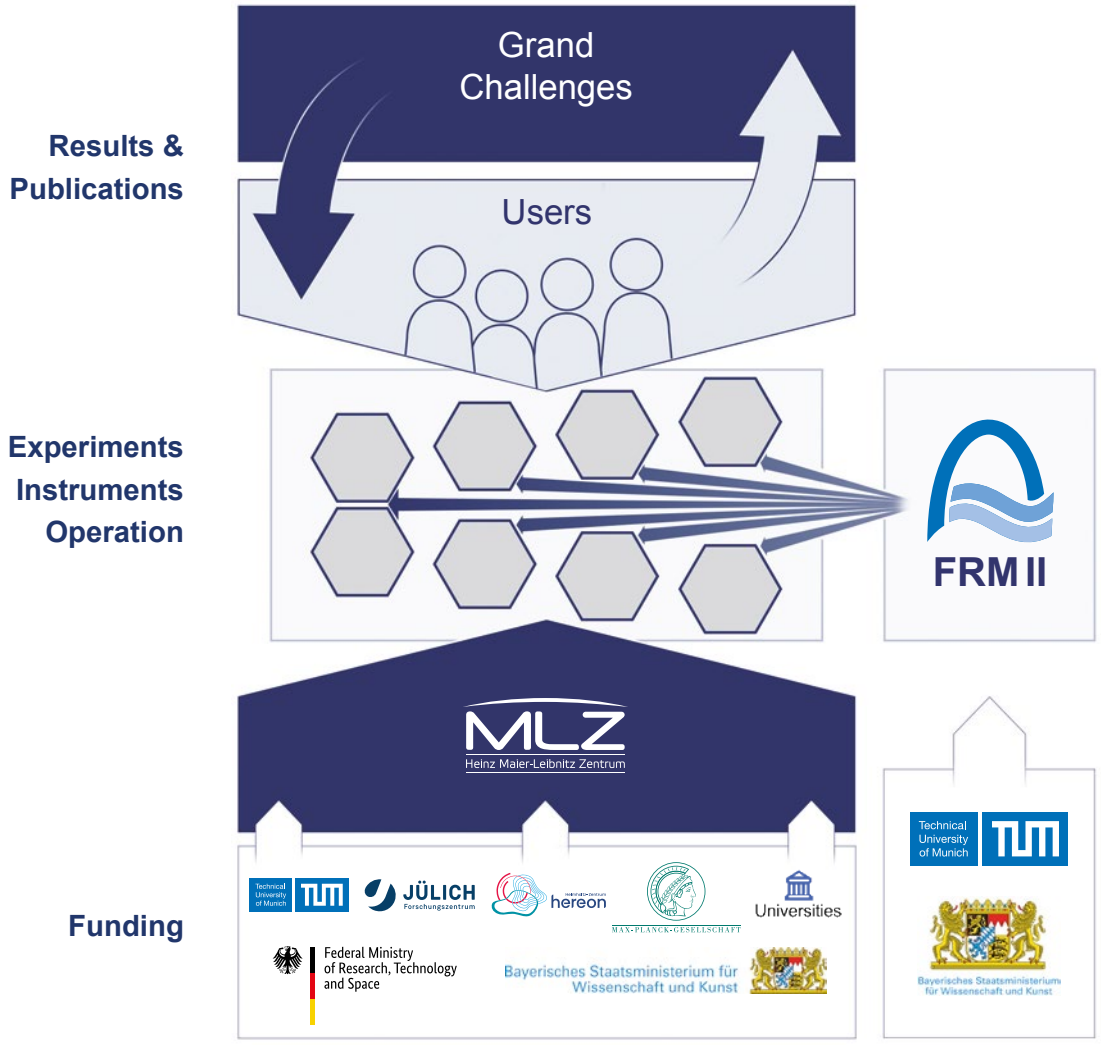

Figure 1: The neutron source FRM II and the user facility MLZ.

Scientific Director MLZ, HGF
Prof. Dr. Stephan Förster (since January 1st, 2026)
Prof. Dr. Martin Müller (until December 31st, 2025)

Scientific Director MLZ, FRM II
Prof. Dr. Christian Pfleiderer

Technical Director FRM II
Dr. Axel Pichlmaier

Administrative Director FRM II
Dr. Jürgen Neuhaus

Scientific cooperation at the Heinz Maier-Leibnitz Zentrum (MLZ)

The Heinz Maier-Leibnitz Zentrum with its cooperating partners, the Technical University of Munich (TUM), Forschungszentrum Jülich GmbH (FZJ) and Helmholtz-Zentrum hereon GmbH is rooted in a network of strong partners including the Max Planck Society (MPG) and numerous university groups that benefit from scientific use of the Research Neutron Source Heinz Maier-Leibnitz. The organisational chart of the MLZ is shown below.

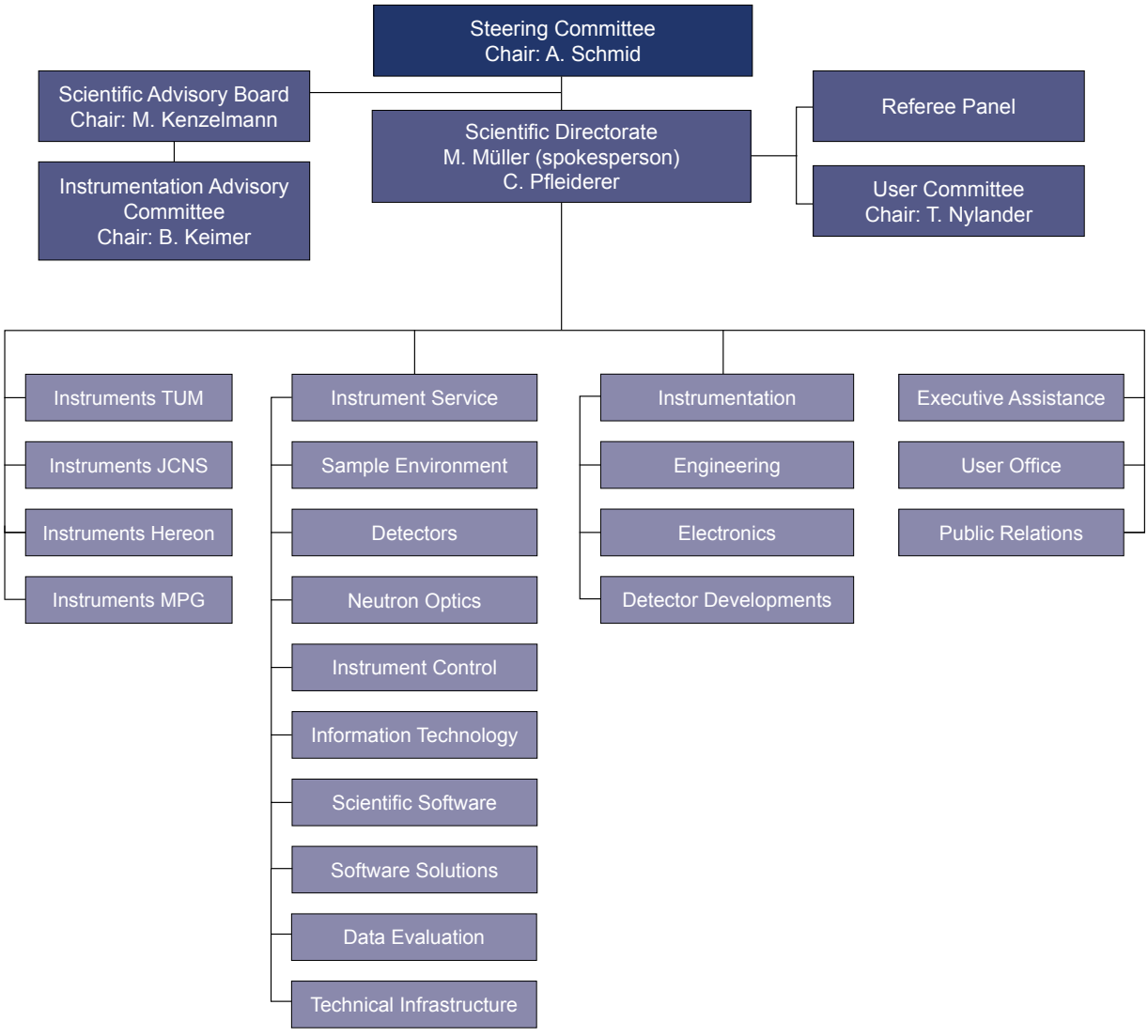

Figure 2: Organisational chart MLZ (2025).

Staff

The charts below show the staff of MLZ and FRM II. The staff of MLZ, as per their share among the partners with a detailed break-down of their function within the MLZ is also depicted.

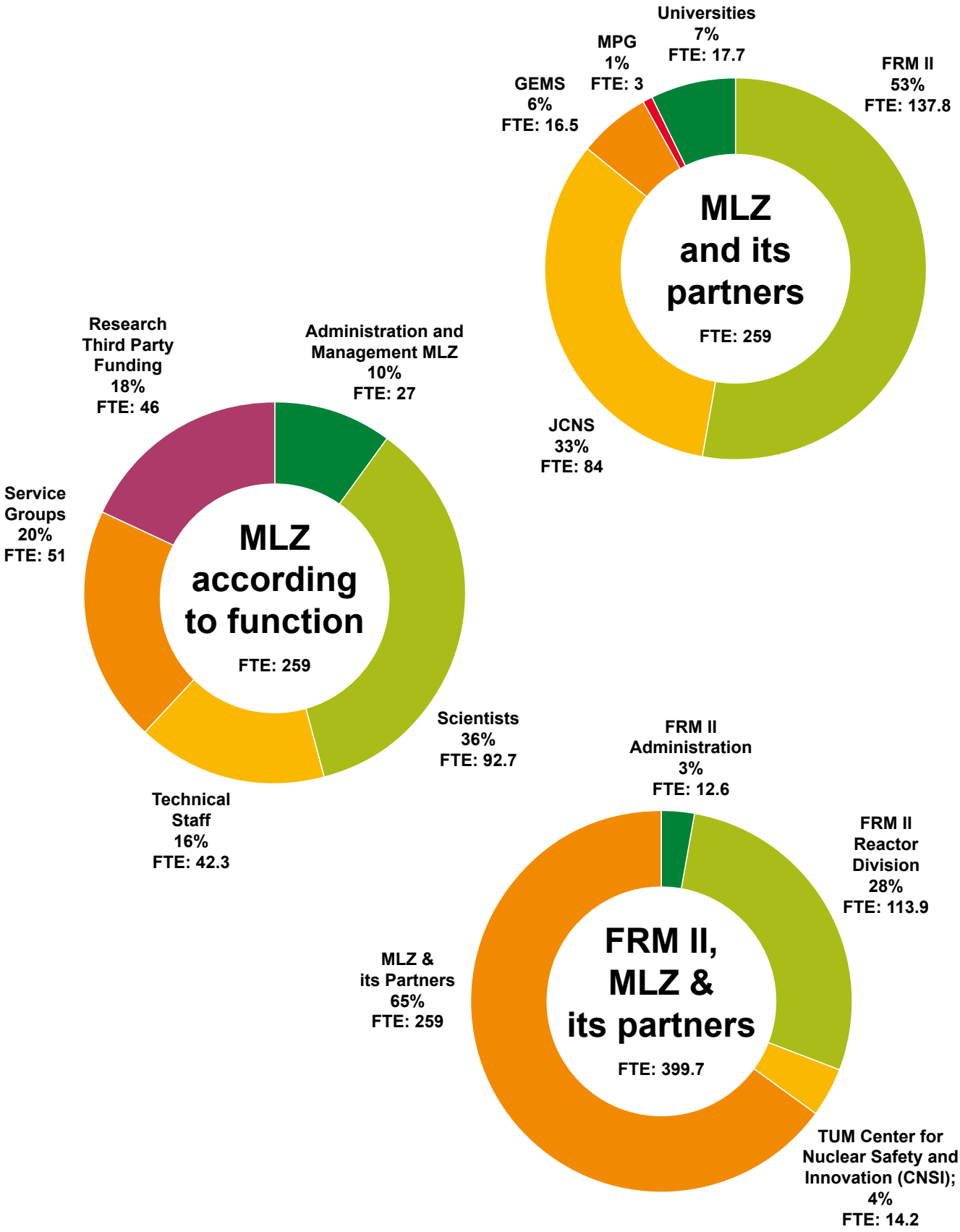

FTE = Full Time Equivalent

Budget

The tables and charts below show the revenue and expenses for 2025.

Revenue 2025

Federal Funding	16.700.000 €
Bavarian Funding	36.638.500 €
Contribution TUM (Planstellen)	10.243.536 €
Contribution FZJ	10.751.000 €
Contribution Hereon	1.320.000 €
Total	**75.653.036 €**

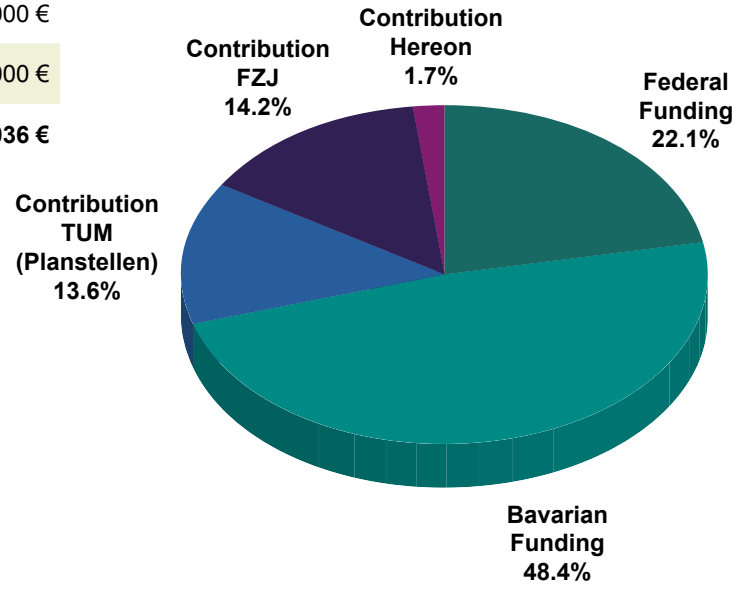

Expenses 2025

	TUM	FZJ	Hereon	**Total**
Personnel costs	22.083.661 €	9.050.000 €	1.661.161 €	**32.794.822 €**
Consumables	35.952.030 €	3.810.000 €	404.487 €	**40.166.517 €**
Investment	431.664 €	1.760.000 €	627.492 €	**2.819.156 €**
Total	**58.467.355 €**	**14.620.000 €**	**2.693.140 €**	**75.780.495 €**

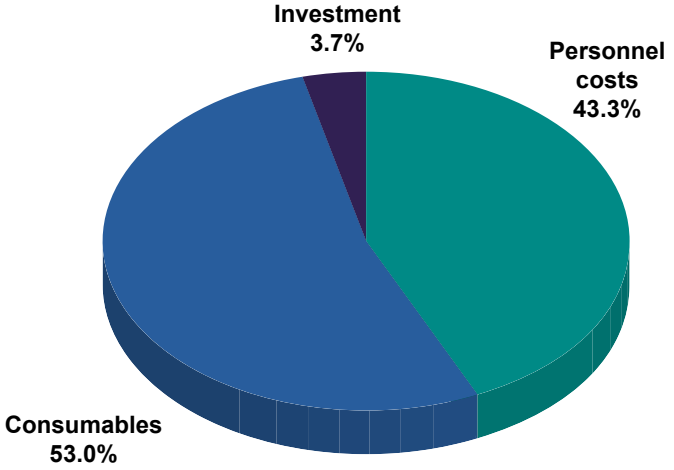

Publications & Theses

In 2025, we received notice of a total of 224 scientific publications, including journal articles, contributions to books and conference proceedings (https://impulse.mlz-garching.de/ and figure below). Furthermore, in total 57 theses, related to MLZ, were completed in 2025.

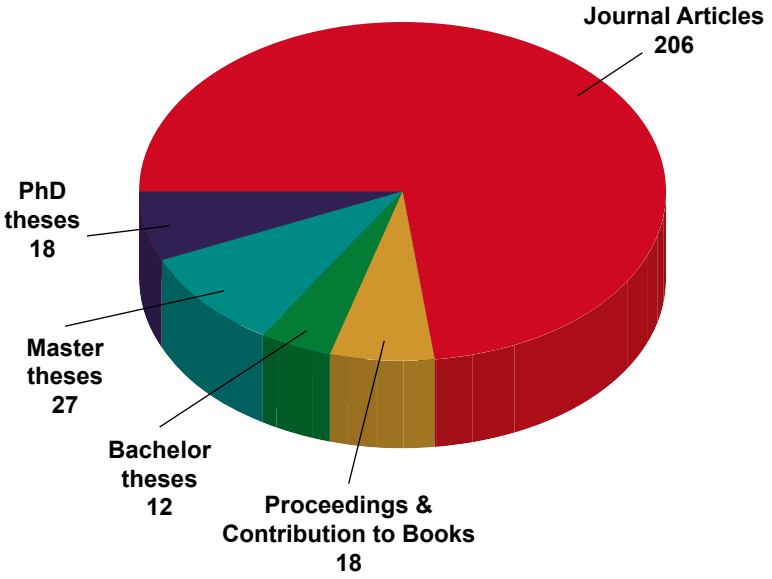

In 2025, 86 PhD theses, based on experiments at the MLZ or method and instrument developments for the MLZ, were either ongoing or completed. Of these, 75 are under the direct supervision of staff at the MLZ and its partner institutions, while the others were externally supervised. In total, 18 of the 85 PhD theses have been completed in 2025.

The next figure shows the classification of the journal articles by Scientific Area (several tags per journal article are possible):

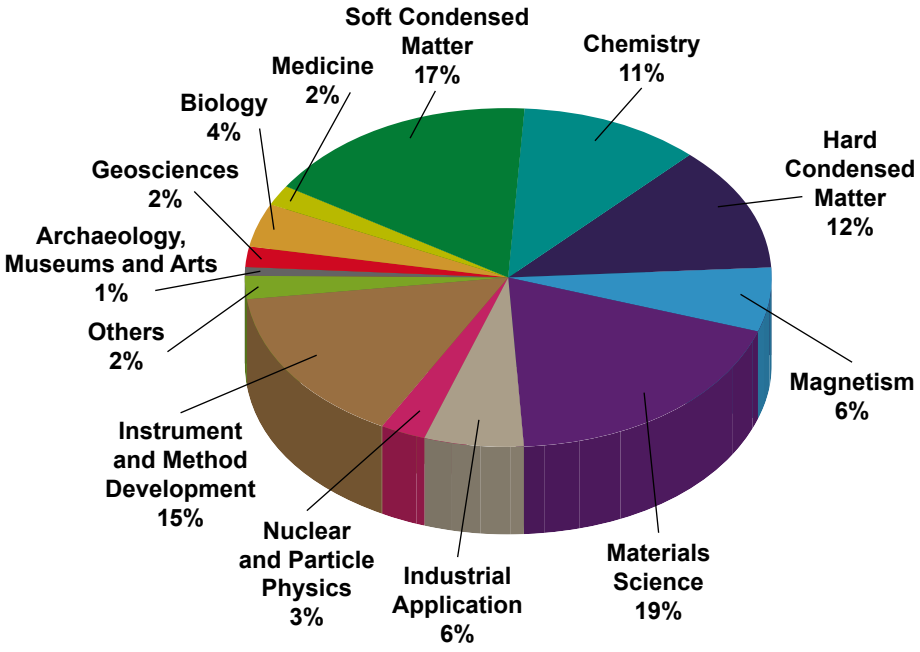

The journal articles at the MLZ can be pictured as a pyramid: Basic Research & Methods (24%) required to tackle the Key Technologies (42%) and articles that directly address the Grand Challenges of our society today (34%). The circular charts represent the individual subjects being dealt with within these three categories.

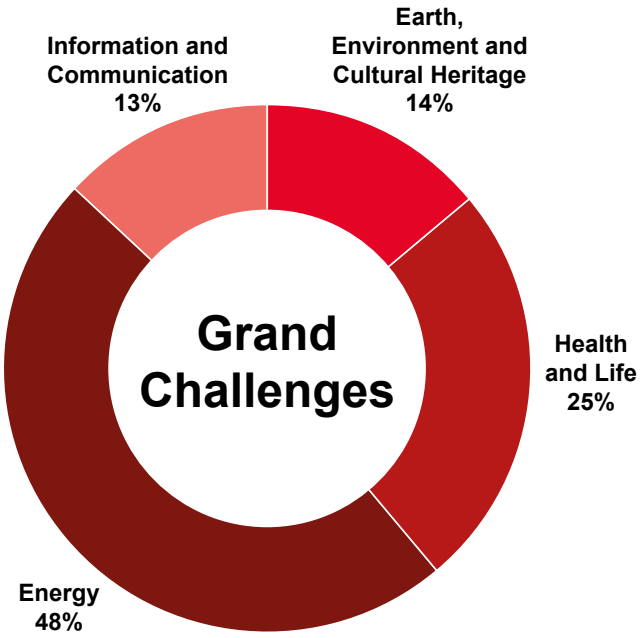

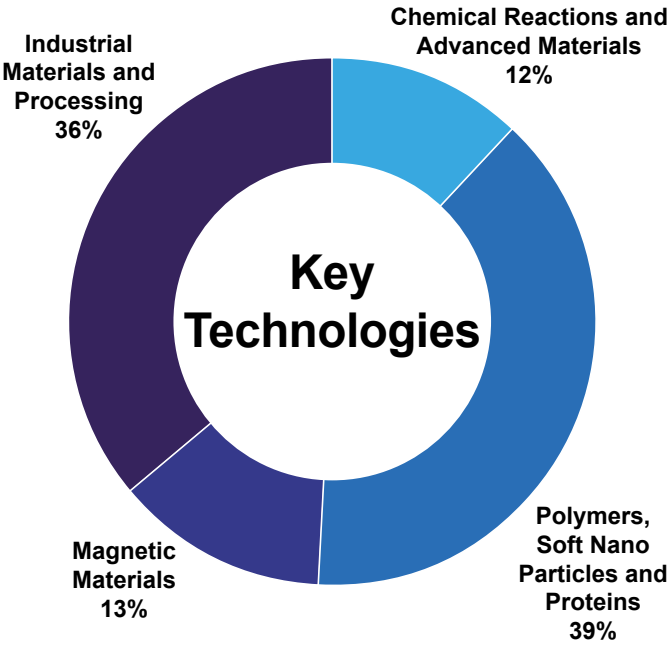

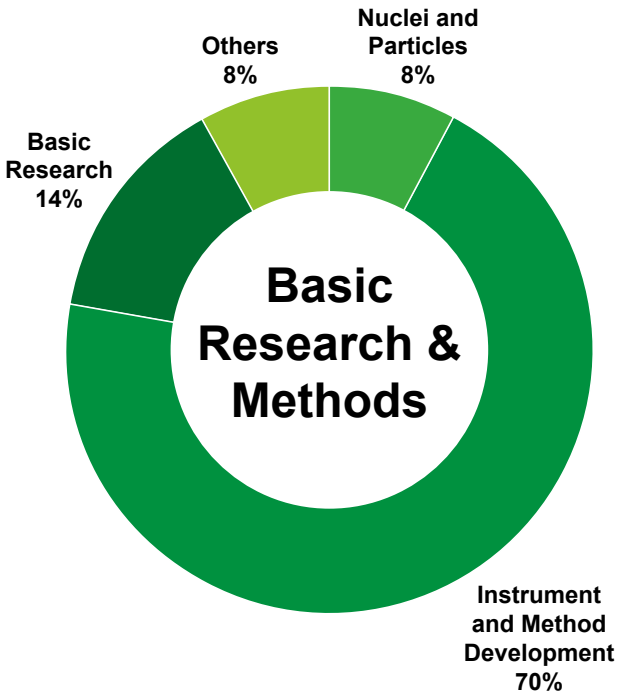

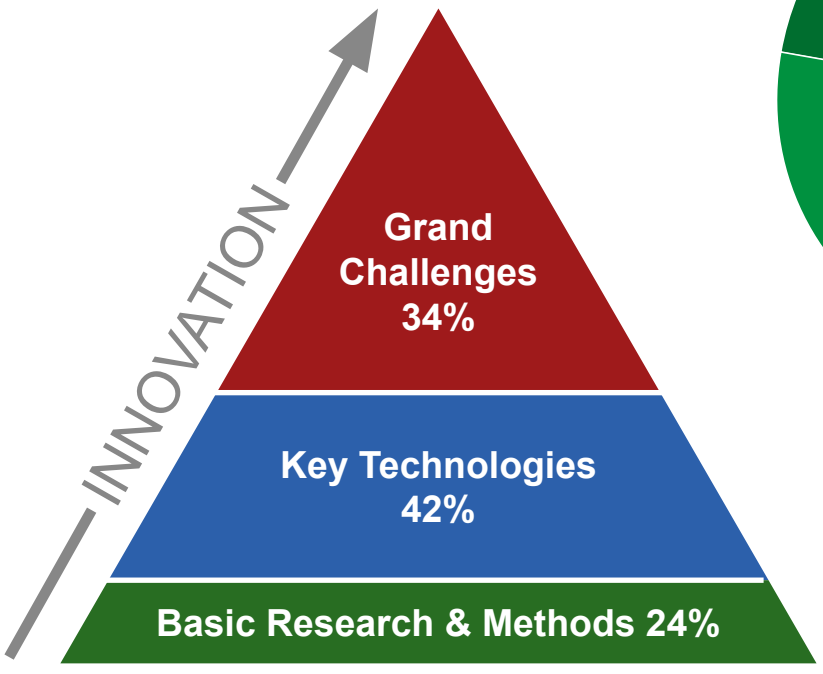

Cover pages

Research by MLZ scientists and at the FRM II made it to the cover pages of several journals in 2025 (see selection below).

G. Brandl et al.,
Robotics for Neutron Scattering Instruments at JCNS, Neutron News 36(1), 13 (2025)
DOI: 10.1080/10448632.2025.2493407

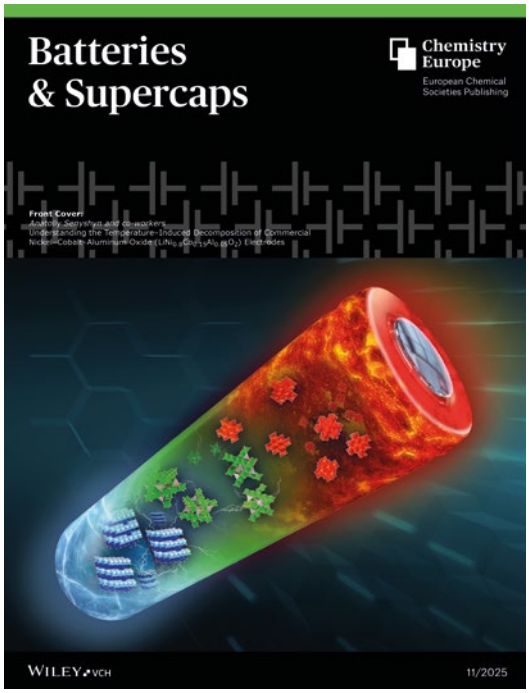

T. Hölderle et al.,
Understanding the Temperature-Induced Decomposition of Commercial Nickel-Cobalt-Aluminum Oxide ($LiNi_{0.8}Co_{0.15}Al_{0.05}O_2$) Electrodes,
Batter. & Supercaps. 8(11), e70165 (2025)
DOI: 10.1002/batt.70165

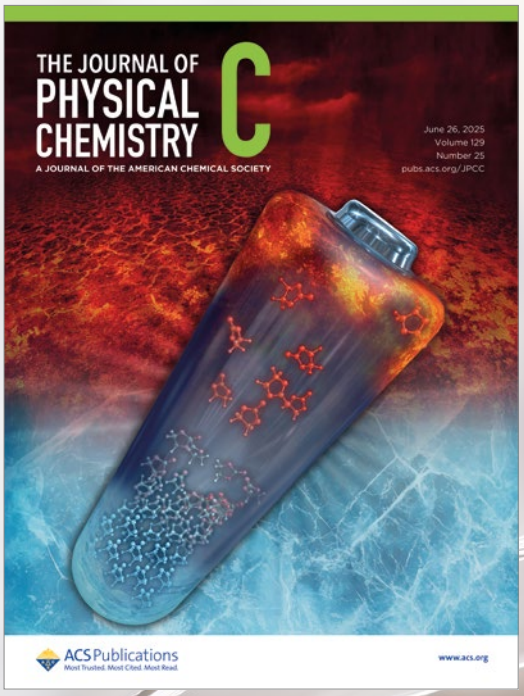

L. Westphal et al.,
Temperature-Resolved Crystal Structure of Ethylene Carbonate, J. Phys. Chem. C. 129(25), 11546 (2025)
DOI: 10.1021/acs.jpcc.4c08421

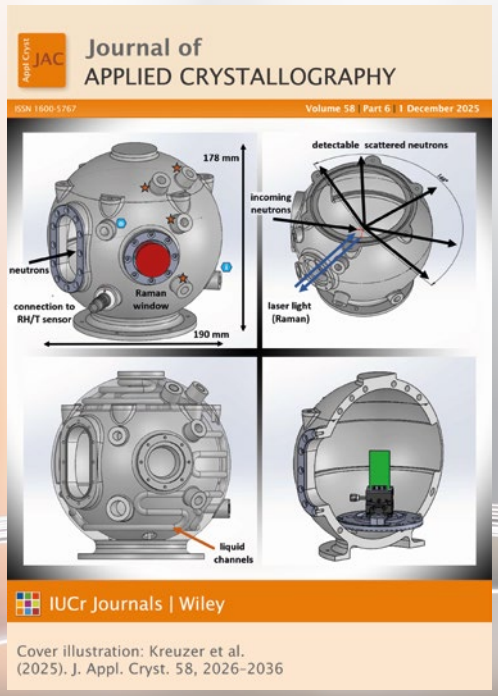

L. P. Kreuzer et al.,
Sample environment for simultaneous quasi-elastic neutron scattering and Raman spectroscopy experiments demonstrated on polymer films under changing humidity and temperature, J. Appl. Crystallogr. 58(6), 2026 (2025)
DOI: 10.1107/S1600576725008519

Committees

Steering Committee

Chair
Dr. Albert Schmid
Bavarian State Ministry of Science and the Arts

Members
Albert Berger
Technical University of Munich

Dr. Harald Haakh
Federal Ministry for Research, Technology and Space

Prof. Dr. sc. techn. Gerhard Kramer
Technical University of Munich

Prof. Dr. Laurens Kuipers
Forschungszentrum Jülich GmbH

Prof. Dr. Regine Willumeit-Römer
Helmholtz-Zentrum hereon GmbH

Guests
Prof. Dr. Christian Pfleiderer
FRM II, Technical University of Munich

Prof. Dr. Martin Müller
Helmholtz-Zentrum hereon GmbH

Prof. Dr. Stephan Förster
Forschungszentrum Jülich GmbH

Dr. Axel Pichlmaier
FRM II, Technical University of Munich

Dr. Jürgen Neuhaus
FRM II, Technical University of Munich

Dirk Schlotmann
Forschungszentrum Jülich GmbH

Figure 1: Steering Committee meeting in December 2025 with J. Neuhaus, C. Pfleiderer, A. Schmid, A. Berger, S. Förster, L. Kuipers, A. Rerich, R. Willumeit-Römer, A. Pichlmaier, H. Haakh, D. Schlotmann, G. Kramer, and M. Müller (from left to right).

Scientific Advisory Board

Chair
Prof. Dr. Michel Kenzelmann
Paul Scherrer Institute, Villigen

Members
Dr. Ken Andersen
Institut Laue-Langevin, Grenoble

Prof. Dr. Lise Arleth
University of Copenhagen

Prof. Dr. Giovanni Bruno
Physikalisch-Technische Bundesanstalt (PTB)
(since October 2025)
Bundesanstalt für Materialforschung und -prüfung (BAM)
(until October 2025)

Prof. Dr. Martin Fertl
Johannes Gutenberg University, Mainz

Dr. Jens Gibmeier
Karlsruhe Institute of Technology (KIT)

Prof. Dr. Thomas Hellweg
Bielefeld University

Prof. Dr. Bernhard Keimer
Max Planck Institute for Solid State Research, Stuttgart

Prof. Dr. Rainer Niewa
University of Stuttgart

Prof. Dr. Julian Oberdisse
Université de Montpellier

Dr. Victoria Garcia Sakai
ISIS Neutron and Muon Source, Didcot

Prof. Dr. Regine v. Klitzing
Technical University of Darmstadt

Figure 2: Scientific Advisory Board meeting in March 2025 with R. Niewa, M. Müller, M. Kenzelmann, L. Arleth, K. Andersen, G. Bruno, M. Fertl, V. Garcia Sakai, C. Pfleiderer, R. v. Klitzing, B. Keimer, and J. Oberdisse (from left to right).

Figure 3: Instrumentation Advisory Committee meeting in February 2025 with C. Niedermayer, W. Lohstroh, H. Rønnow, S. Mattauch, R. Woracek, U. Köster, B. Keimer, M. Müller, C. Pfleiderer, M. T. Fernández-Díaz, I. Hoffmann, F. Ott, C. Pappas, M. Schulz, and J.-F. Moulin (from left to right).

Instrumentation Advisory Committee

Chair
Prof. Dr. Bernhard Keimer
Max Planck Institute for Solid State Research, Stuttgart

Members
Dr. Maria Teresa Fernández-Díaz
Institut Laue-Langevin, Grenoble

Dr. Ingo Hoffmann (Observer on behalf of the KFN)
Institut Laue-Langevin, Grenoble

Prof. Dr. Ulli Köster
Institut Laue-Langevin, Grenoble

Prof. Dr. Christof Niedermayer
Paul Scherrer Institute, Villigen

Dr. Frédéric Ott
Laboratoire Léon Brillouin, Saclay

Prof. Dr. Catherine Pappas
Delft University of Technology

Prof. Dr. Henrik Rønnow
Ecole Polytechnique Fédérale de Lausanne

Dr. Robin Woracek
European Spallation Source, Lund

MLZ User Committee

Chair
Prof. Dr. Tommy Nylander
Lund University

Members
Dr. Andrea Scotti
RWTH Aachen University

Dr. Jens Gibmeier
Karlsruhe Institute of Technology

Dr. Ana Brás Würschig
University of Cologne

Dr. Sandra Cabeza
Institut Laue-Langevin, Grenoble

Prof. Dr. Holger Kohlmann (Observer on behalf of the KFN)
Leipzig University

Evaluation of beam time proposals: Members of the Review Panels

Dr. Markus Appel
Institut Laue-Langevin, Grenoble

Prof. Dr. Lise Arleth
Niels Bohr Institute
University of Copenhagen

Dr. Mikhail Avdeev
Frank Laboratory of Neutron Physics
Joint Institute for Nuclear Research, Dubna

Prof. Dr. Piero Baglioni
University of Florence

Dr. Luis Fernández Barquín
University of Cantabria, Santander

Prof. Dr. Peter Battle
University of Oxford

Dr. Matthew Blakeley
Institut Laue-Langevin, Grenoble

Dr. Johann Bouchet
Commissariat à l'énergie atomique et
aux énergies alternatives, Arpajon

Dr. Philippe Bourges
Laboratoire Léon Brillouin, Saclay

Prof. Dr. William Brant
Uppsala University

Prof. Dr. Richard Campell
University of Manchester

Dr. Petr Čermák
Charles University, Prague

Dr. Robert Cubitt
Institut Laue-Langevin, Grenoble

Dr. Sabrina Disch
University of Cologne

Dr. Stephan Eijt
Delft University of Technology

Prof. Dr. Ulli Englert
RWTH Aachen University

Prof. Dr. Björn Fåk
Institut Laue-Langevin, Grenoble

Dr. Bela Farago
Institut Laue-Langevin, Grenoble

Prof. Dr. Rafael Omar Ferragut
L-NESS, Como

Dr. Anne-Caroline Genix
Laboratoire Charles Coulomb
Université Montpellier

Dr. Francesco Grazzi
National Research Council of Italy,
Florence Research Area

Dr. Christian Grünzweig
Paul Scherrer Institute, Villigen

Dr. Klaus Habicht
Helmholtz-Zentrum Berlin für
Materialien und Energie

Prof. Dr. Thomas Hellweg
Bielefeld University

Prof. Dr. Paul Henry
ISIS Neutron and Muon Source, Didcot

Dr. Ingo Hoffmann
Institut Laue-Langevin, Grenoble

Dr. Dirk Honecker
ISIS Neutron and Muon Source, Didcot

Dr. Christy Kinane
ISIS Neutron and Muon Source, Didcot

Dr. Joachim Kohlbrecher
Paul Scherrer Institute, Villigen

Dr. Reinhard Kremer
Max Planck Institute for
Solid State Research, Stuttgart

Prof. Dr. Christian Krempaszky
Technical University of Munich, Garching

Prof. Dr. Jeremy Lakey
University of Newcastle

Dr. Reidar Lund
Oslo University

Dr. Sandrine Lyonnard
Commissariat à l'énergie atomique et
aux énergies alternatives, Grenoble

Dr. Nicolas Martin
Laboratoire Léon Brillouin, Saclay

Dr. Gwilherm Nénert
PANalytical B.V., Almelo

Dr. Thomas Nitschke-Pagel
TU Braunschweig

Dr. Esko Oksanen
European Spallation Source, Lund

Prof. Dr. Andrea Orecchini
Università degli Studi di Perugia

Dr. Alessandro Paciaroni
Università degli Studi di Perugia

Prof. Dr. Christine Papadakis
Technical University of Munich, Garching

Dr. Oleg Petrenko
University of Warwick

Dr. Thilo Pirling
Institut Laue-Langevin, Grenoble

Prof. Dr. Radosław Przeniosło
University of Warsaw

Prof. Dr. Diana Lucia Quintero Castro
University of Stavanger

Dr. Navid Qureshi
Institut Laue-Langevin, Grenoble

Dr. Florin Radu
Helmholtz-Zentrum Berlin für
Materialien und Energie

Dr. Sarah Rogers
ISIS Neutron and Muon Source, Didcot

Dr. Emmanuel Schneck
Max Planck Institute of
Colloids and Interfaces, Potsdam

Prof. Dr. Roland Schwab
University of Tübingen

Dr. Romain Sibille
Paul Scherrer Institute, Villigen

Dr. Thorsten Soldner
Institut Laue-Langevin, Grenoble

Prof. Dr. Thomas Sottmann
University of Stuttgart

Dr. Andreas Stark
Helmholtz-Zentrum hereon GmbH

Dr. Johannes Sterba
Atominstitut Wien, TU Wien

Dr. Christopher Stock
University of Edinburgh

Dr. Pavel Strunz
Nuclear Physics Institute, Réz near Prague

Dr. Anne Stunault
Institut Laue-Langevin, Grenoble

Dr. László Szentmiklósi
Hungarian Academy of Sciences, Budapest

Dr. Kristiaan Temst
KU Leuven

Dr. Alexander Tsirlin
Augsburg University

Prof. Dr. Regine von Klitzing
Technical University of Darmstadt

Dr. Oksana Zaharko
Paul Scherer Institut, Villigen

Prof. Dr. Hongbin Zhang
Technical University of Darmstadt

Partner institutions

Bavarian Research Institute of
Experimental Geochemistry and Geophysics
University of Bayreuth
www.bgi.uni-bayreuth.de

Georg-August-Universität Göttingen

- Geoscience Center
  www.uni-goettingen.de/de/125309.html

German Engineering Materials Science Centre GEMS
Helmholtz-Zentrum hereon GmbH
www.hereon.de/central_units/gems/index.php.de

Jülich Centre for Neutron Science JCNS
Forschungszentrum Jülich GmbH
www.fz-juelich.de/de/jcns

Karlsruhe Institute of Technology

- Institute for Applied Materials – Energy Storage Systems (IAM-ESS)
  www.iam.kit.edu/ess/
- KIT Institute for Quantum Materials and Technologies (IQMT)
  www.iqmt.kit.edu/index.php

Ludwig-Maximilians-University

- Faculty of Physics
  www.physik.lmu.de

Max Planck Institute for Solid State Research Stuttgart
www.fkf.mpg.de

RWTH Aachen University

- Institute of Crystallography
  www.ifk.rwth-aachen.de
- Institute of Inorganic Chemistry
  www.iac.rwth-aachen.de

Technische Universität Dresden

- Institute of Solid State and Materials Physics
  www.tu-dresden.de/mn/physik/ifp

Technical University of Munich

TUM School of Natural Sciences

- Chair for Functional Materials
  www.ph.nat.tum.de/functmat/ueber-uns/
- Institute for Hadronic Structure and Fundamental Symmetries
  www.ph.nat.tum.de/e18/home
- Chair of Experimental Physics on the Topology of Correlated Systems
  www.ph.nat.tum.de/en/tcs/home/
- Chair of Precision Measurements at Extreme Conditions
  www.ph.nat.tum.de/e66/home
- Particle Physics at Low Energies
  www.ph.nat.tum.de/ene/home
- Chair of Biomedical Physics
  www.ph.nat.tum.de/en/e17/home

Central Scientific Institution

- RCM – Radiochemie München
  www.rcm.tum.de

Technical University of Munich

- Klinikum rechts der Isar
  www.mri.tum.de

Vienna University of Technology

- Neutron- and Quantum Physics
  Research area at the Atominstitut Vienna
  Abele Group
  www.tuwien.at/en/phy/ati/neutron-and-quantum-physics

Universität der Bundeswehr München

- Institute of Applied Physics and Measurement Technology
  www.unibw.de/lrt2

University of Cologne
Faculty of Mathematics and Natural Sciences

- Institute for Nuclear Physics
  https://ikp.uni-koeln.de/
- Institute of Physics II
  https://ph2.uni-koeln.de/

Universität Heidelberg

- Physikalisches Institut
  www.physi.uni-heidelberg.de/

Imprint

Publisher

Technische Universität München
Forschungs-Neutronenquelle
Heinz Maier-Leibnitz (FRM II)
Lichtenbergstr. 1
85747 Garching
Germany

Phone: +49.89.289.14965
Fax: +49.89.289.14995
Internet: www.mlz-garching.de
www.frm2.tum.de
E-Mail: jahresbericht@frm2.tum.de

Editorial Office, Design and typesetting

Anke Görg
Connie Hesse
Michael Hörmannsdorfer
Christoph Kreileder
Reiner Müller
Björn Pedersen
Laura Richter
Robert Schulze (getyourdesign, Berlin)
Serguei Vaguine
Andrea Voit

Editors

Henrich Frielinghaus
Robert Georgii
Francesco Guatieri
Markus Hölzel
Michael Hofmann
Olaf Holderer
Johanna Jochum
Vladislav Kochetov
Lucas Kreuzer
Martin Meven
Andreas Ostermann
Björn Pedersen
Zsolt Revay
Nicolas Walte
Marcell Wolf

Photographic credits

p. 6 bottom left:	Astrid Eckert (TUM)
bottom 2nd left:	Ralf-Uwe Limbach
bottom 2nd right:	Alessandra Schellnegger
bottom right:	Andreas Heddergott (TUM)
p. 8/9	Bernhard Ludewig
p. 10	Francesco Guatieri & AI-generated by Nano Banana (Google), edited and modified by Reiner Müller (FRM II),
p. 11, 12, 13, 14, 15, 16, 18 and 19	AI-generated by Nano Banana (Google), edited and modified by Reiner Müller (FRM II),
p. 17	Márcio L. Castro & AI-generated by Nano Banana (Google), edited and modified by Reiner Müller (FRM II),
p. 20/21	Astrid Eckert (TUM)
p. 60/61	Bernhard Ludewig
p. 62 top left	Andreas Heddergott (TUM)
p. 70/71	Bernhard Ludewig
p. 83	Astrid Eckert (TUM)
p. 86/87	Bernhard Ludewig
p. 95, bottom:	Andreas Heddergott (TUM)
p. 96, top:	Markus Braumann
back cover:	Bernhard Ludewig

Editors, authors or FRM II/TUM: other images

MLZ Instrument Suite

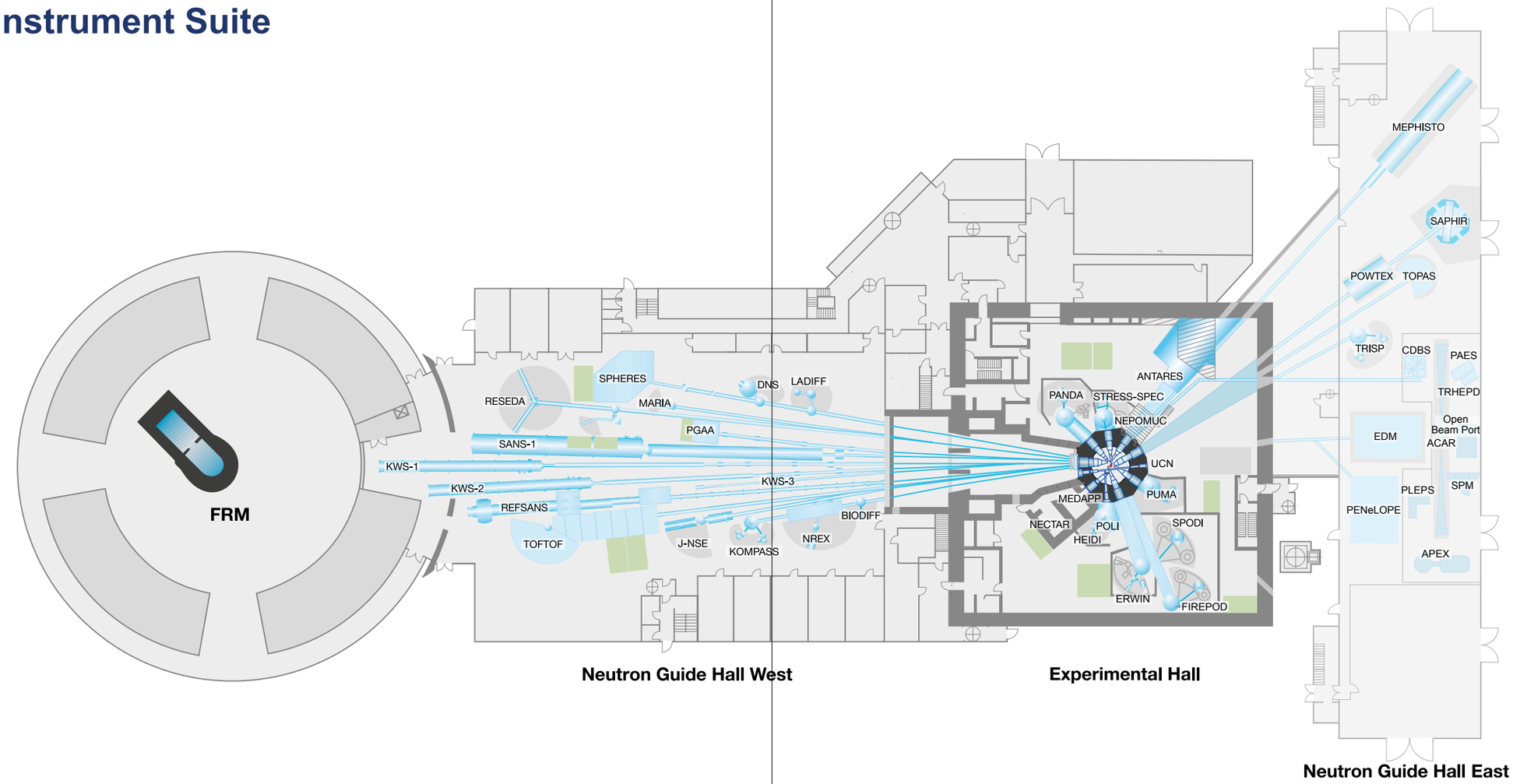

Instrument	Description	Neutrons	Operated by	Funding	Instrument group at MLZ
ANTARES	Radiography and tomography	cold	TUM, GEMS	TUM, Hereon	FRM II, GEMS
BIODIFF	Diffractometer for large unit cells	cold	TUM, JCNS	TUM, FZJ	FRM II, JCNS
DNS	Diffuse scattering spectrometer	cold	JCNS	FZJ	JCNS
ERWIN	Powder diffractometer	thermal	TUM	TUM	FRM II
FIREPOD	Powder diffractometer	thermal	TUM	TUM	FRM II
HEIDI	Single crystal diffractometer	hot	RWTH Aachen	FZJ	JCNS
J-NSE	Spin-echo spectrometer	cold	JCNS	FZJ	JCNS
KOMPASS	Three axes spectrometer	cold	Uni Köln, TUM	TUM	FRM II
KWS-1	Small angle scattering	cold	JCNS	FZJ	JCNS
KWS-2	Small angle scattering	cold	JCNS	FZJ	JCNS
KWS-3	Very small angle scattering	cold	JCNS	FZJ	JCNS
LADIFF	High resolution larmor diffraction and inelastic scattering	cold	TUM	TUM	FRM II
MARIA	Magnetic reflectometer	cold	JCNS	FZJ	JCNS
MEPHISTO	Instrument for particle physics, PERC	cold	TUM	TUM, DFG	FRM II
MEDAPP	Medical irradiation treatment	fast	TUM	TUM	FRM II
NECTAR	Radiography and tomography	fast	TUM, GEMS	TUM, Hereon	FRM II, GEMS
NEPOMUC	Positron source, CDBS, PAES, PLEPS, SPM, TRHEPD, ACAR, APEX, Open Beam Port	-	TUM, UniBw München	TUM	FRM II

*construction
ErUM: instrument construction funded by ErUM-Pro (BMFTR)

Instrument	Description	Neutrons	Operated by	Funding	Instrument group at MLZ
NREX	Reflectometer with X-ray option	cold	MPI Stuttgart	MPG	MPI Stuttgart
PANDA	Three axes spectrometer	cold	JCNS, TU Dresden	FZJ	JCNS
PGAA	Prompt gamma activation analysis, Neutron activation analysis (NAA), Neutron depth profiling (NDP)	cold	Uni Köln	TUM	FRM II
PUMA	Three axes spectrometer	thermal	KIT	TUM	FRM II
POLI	Single-crystal diffractometer polarised neutrons	hot	RWTH Aachen	FZJ	JCNS
POWTEX	Time-of-flight diffractometer	thermal	RWTH Aachen, Uni Göttingen, JCNS	ErUM, FZJ	JCNS
REFSANS	Reflectometer	cold	GEMS	Hereon	GEMS
RESEDA	Resonance spin-echo spectrometer	cold	TUM	TUM	FRM II
SANS-1	Small angle scattering	cold	TUM, GEMS	TUM, Hereon	FRM II, GEMS
SAPHIR	Six anvil press for radiography and diffraction	thermal	Uni Bayreuth	TUM	FRM II
SPHERES	Backscattering spectrometer	cold	JCNS	FZJ	JCNS
SPODI	Powder diffractometer	thermal	KIT	TUM	FRM II
STRESS-SPEC	Materials science diffractometer	thermal	TUM, GEMS	TUM, Hereon	FRM II, GEMS
TOFTOF	Time-of-flight spectrometer	cold	TUM	TUM	FRM II
TOPAS	Time-of-flight spectrometer	thermal	JCNS	FZJ	JCNS
TRISP	Three axes spin-echo spectrometer	thermal	MPI Stuttgart	MPG	MPI Stuttgart
UCN*	Ultra cold neutron source, EDM, PENeLOPE	ultra-cold	TUM	TUM, DFG	FRM II

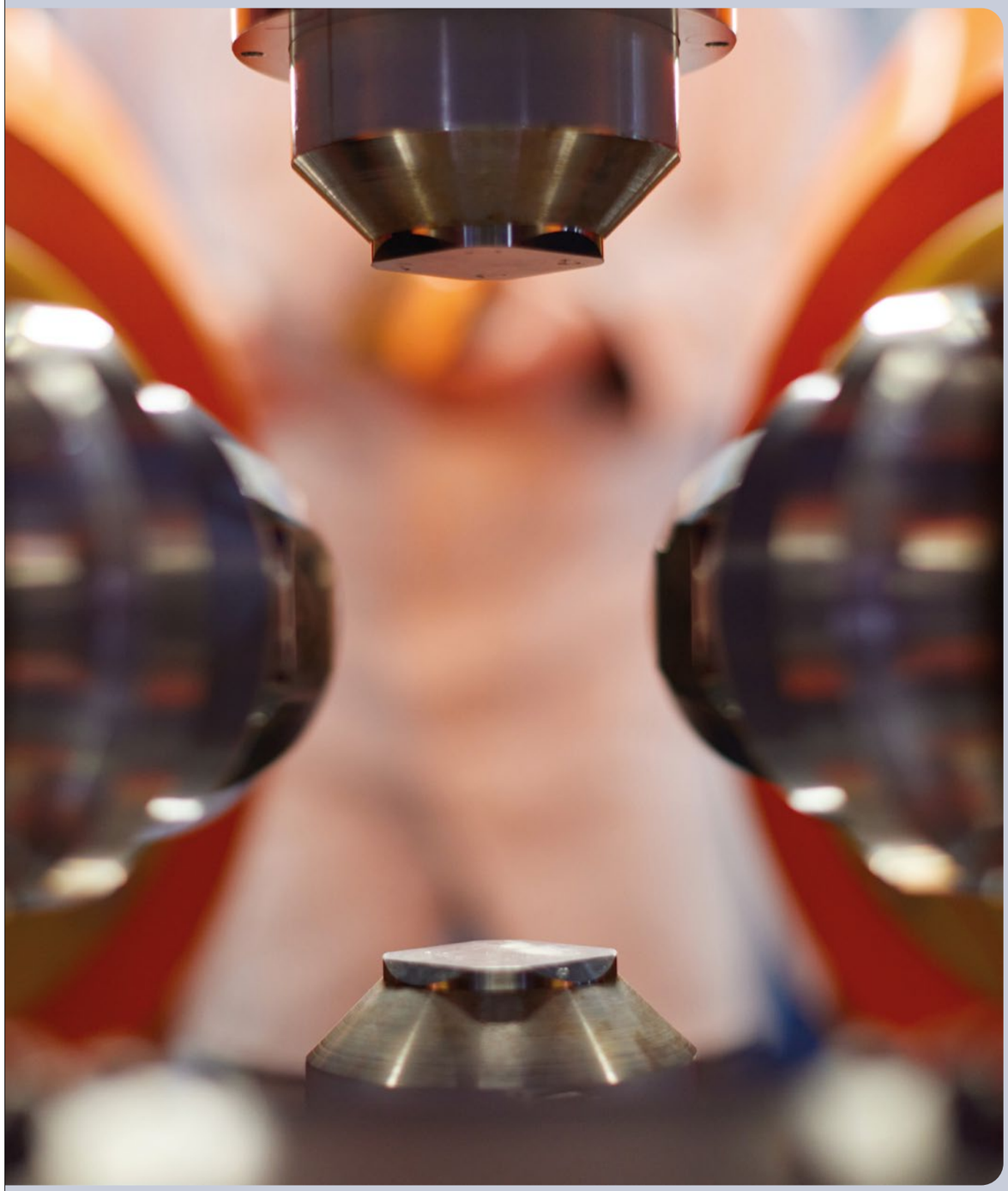

Front page:
Insight into the neutron guide housings at beamline 5. The neutron guides shown here supply four new state-of-the-art instruments in the Neutron Guide Hall East: POWTEX, TOPAS, TRISP and SAPHiR.

Back page:
The Six Anvil Press for High pressure Radiography and TOF diffraction SAPHiR has analysed meteorites (see p. 29).

Heinz Maier-Leibnitz Zentrum (MLZ)
www.mlz-garching.de
DOI: 10.14459/2025md1833056